CERN-THESIS-2007-179

Università degli Studi di Roma
"Tor Vergata"
Facoltà di Scienze Matematiche, Fisiche e Naturali

Study of the Lepton Flavor Violating decay $\tau \to 3\mu$ with the Atlas detector

Doctoral Thesis in Physics

Silvia Ventura

Tutor

Dott. B. Esposito, S. Miscetti

Coordinator

Prof. P. Picozza

A mia madre...

Contents

Introduzione

The Atlas detector is one of the four experiments presently under construction at the interaction points of the Large Hadron Collider (LHC) of CERN. The LHC is a proton-proton collider that will accelerate protons up to a center of mass energy of 14 TeV and with the design goal to reach the unprecedented luminosity of 10^{34} cm^{-2} s^{-1}. The very high values of luminosity and center of mass energy will allow to explore a large and variegated set of physics topics.

The Atlas detector is a general purpose detector which has been designed to explore the high energy frontier above the 1 TeV scale. Among the main physical goals, we list the search of the Higgs boson, the only unobserved particle predicted by the Standard Model (SM), the search for new massive vector bosons foreseen by several models beyond the SM and the search for the yet unseen supersymmetric particles. In order to reach all these physical goals, high quality performances in particle identification and high precision measurement of momentum, energy and charge are necessary.

The Atlas detector is made of layers of different technologies. An inner detector surrounds the beam line and measures the trajectories, and thereby the momenta, of charged particles. A super-conducting solenoid, which generates a homogeneous 2 T magnetic field in the inner detector volume, closes the inner detector. Directly outside this solenoid, the electromagnetic and hadronic calorimeters are located. The outermost shell of the detector is formed by the muon spectrometer, which identifies the muon with high efficiency and measures their momentum. In order to minimize multiple scattering effects, the magnetic field in this region is realized by three huge super-conducting air-core toroids.

Clean signatures of interesting processes are often granted by high momentum leptons (electrons and muons) produced in the final state. For istance, one of the most promising decay channel for the discovery of the Higgs boson is the decay $H \rightarrow ZZ \rightarrow 4\mu$ where four high momentum muons are produced. Moreover, the new vector bosons, W' and Z', can also be discovered by observing their leptonic decay with production of muons with transverse momentum up to few TeV. Hence very good performances in the measurement

of the muon transverse momentum and very high trigger capability are required in order to observe such important physics processes.

The Atlas Muon Spectrometer has been design to provide a very good stand-alone measurement of the muon momentum with a relative accuracy from 3% up to 10% in a muon transverse momentum range from few GeV to 1 TeV and in a wide pseudorapidity range ($|\eta| < 2.5$). This is due to the combination of a large lever arm, the three huge super-conducting air-core toroids and the three tracking chambers layers that provide a precision coordinate measurement in the bending direction of the toroidal magnet. The other coordinate is measured with smaller precision by RPC or TGC chambers which instead are used to build the LVL1 trigger for muons.

The tracking detectors of the Muon Spectrometer are the Monitored Drift Tube chambers. The MDT chambers are detectors composed by layers of pressurized drift tubes glued together. They can provide the measurement of the muon trajectory with a precision of 40 μm. In the past few years, the MDT chamber functionality has been tested in several ways. An important step in the understanding of the chamber performances has been the test beam at the H8 beam line of SPS. In this setup, the first measurement of the muon momentum in an Atlas-like environment has been performed and is described in detail in this thesis. Moreover each MDT chamber, of the middle and outer stations of the Muon Spectrometer, has also been tested with cosmic rays before being installed in the Atlas cavern. The procedure used at the cosmic ray facility BB5 of CERN is also presented in this work.

The last part of this thesis concerns the MonteCarlo study of the Lepton Flavor Violating (LFV) decay of the τ lepton in three muons. This rare decay is foreseen by several models beyond the Standard Model. For instance, in the frame of the SuperSymmetric theory, a branching ratio of the order of 10^{-7} is expected for such a decay which are very close to the best limits (BR $< 2\times10^{-7}$ at 90% C.L.) already set by the beauty factories (Babar and Belle). An improvement of the experimental sensitivity on the branching ratio for processes involving lepton flavor changing in the charged lepton sector is an interesting topics, either to give origin to an observation or to extend the exclusion limits. Even without any observation, the reduction of the upper limit can help in distinguish which theory model better describes the dynamic of this LFV decay. In this thesis a selection strategy to search for this signal with the Atlas detector has been developed. Evaluation of the detection efficiency and of the background rejection power has been done with a fast simulation. A detailed study with a complete detector simulation has also been carried out which is helping in tuning the algorithms and the reconstruction for such a search.

In Chapter 1, a description of the main physics goals of the Atlas experiment is reported. In particular the LFV decay of the τ lepton in three muons is considered in the frame of the SuperSymmetric Standard Model. Moreover a brief description of the analysis performed by other collaborations, in particular from the B-factories Babar and Belle, on this decay channel is presented in order to introduce to the analysis of the decay $\tau \rightarrow 3\mu$.

In Chapter 2, the Atlas detector is described with particular attention to the characteristics and performances of the Muon Spectrometer. The Monitored Drift Tube chambers,

used as tracking detectors in the muon system of Atlas, are described in Chapter 3.

In Chapter 4, results of analysis of the data collected at the H8 beam line of the SPS at CERN are reported. In the H8 setup two towers of the barrel muon spectrometer were located offering the opportunity to study the chamber performances. With these data, it has been possible to measure for the first time, the resolution of the transverse muon momentum. The results obtained confirms that the three stations of the muon spectrometer are able to measure the curvature of muons with the required precision of 50 μm.

In Chapter 5, the procedure to certificate an MDT chamber before the installation in the Atlas cavern is described. Each single MDT chamber of the middle and outer stations of the Muon Spectrometer has indeed been tested at the cosmic ray stand at CERN before the installation. Once a chamber has been certified with cosmic rays, it is considered ready for installation in the detector. Other performance tests on the first chambers installed in final positions in the spectrometer are also described.

In Chapter 6, the analysis of the LFV channel $\tau \to 3\mu$ performed with simulated events is presented. The analysis consists in studying the most characteristic signal features in order to individuate the best strategy selection with higher efficiency while improving the backgrounds rejection. Given the low momentum of the decay products in this channel, it is relevant to reconstruct muons down to 3 GeV. For the background, a statistic corresponding to above 20 fb^{-1} has been generated and simulated with the fast simulation while for the signal around 20000 events have been simulated. In the signal case, either a uniform phase-space decay for the three muons or a detailed simulation of the decay in the contest of the Minimal Supersymmetric Standard Model (MSSM) have been used. At the end of the analysis chain, we extract signal efficiency and expected background yield. These numbers are then used to estimate the achieveable upper limit on the signal in the hypothesis of zero events observed.

With the full simulation many technical details have been investigated and solved although some analysis aspects have still to be understood. However the results obtained with the fast simulation indicates that the Atlas detector, thanks to the high luminosity of LHC and the very good detector performances, can improve the present upper limit on this decay branching ratio already in the first year of data taking.

Chapter 1

The LHC physics program

1.1 The Large Hadron Collider at CERN

The Large Hadron Collider (LHC) [1] is a proton-proton collider currently under construction at CERN. The LHC will be installed in the 27 Km underground circular tunnel where LEP, the electron-positron collider has taken place before it. LHC has been designed to access the energy frontier above the TeV scale. In order to achieve this task protons are accelerated and stored at an energy of 7 TeV and collide with an unprecedented luminosity of 10^{34} cm^{-2} s^{-1}. The LHC will be completed by the summer 2007.

The existing injector chain, shown in Fig.1.1, will be used for producing the LHC beams. The protons are produced and accelerated to 50 MeV by the proton linac before being injected into the 2.5 GeV Proton Syncroton (PS). The Proton Synchroton (PS) and the Super Proton Synchroton (SPS) will be used to accelerate the protons up to an energy of 450 GeV before injecting them into the LHC main rings. Once the protons are injected in the main rings they are divided in bunches of 10^{11} particles and accelerated to the energy of 7 TeV. The bunches will collide in four interaction points along the LHC where experimental apparatuses are located to study the interaction products.

The choice to have proton-proton interactions instead of proton-antiproton is due to the difficulty in producing a so high density beam of antiprotons. As a consequence, LHC requires separate vacuum pipes for each proton beam, both contained in the same cryogenic and mechanical structure, and demands a novel design of the superconducting bending magnets to keep the two beams rotating in opposite direction orbits. The beams will collide with an angle of 300 μrad.

The accelerator magnetic field is produced by 1232 14.6 m long superconducting two-in-one dipoles. The superconducting magnets have to be cooled to very low temperatures (a few degrees Kelvin) with superfluid Helium.

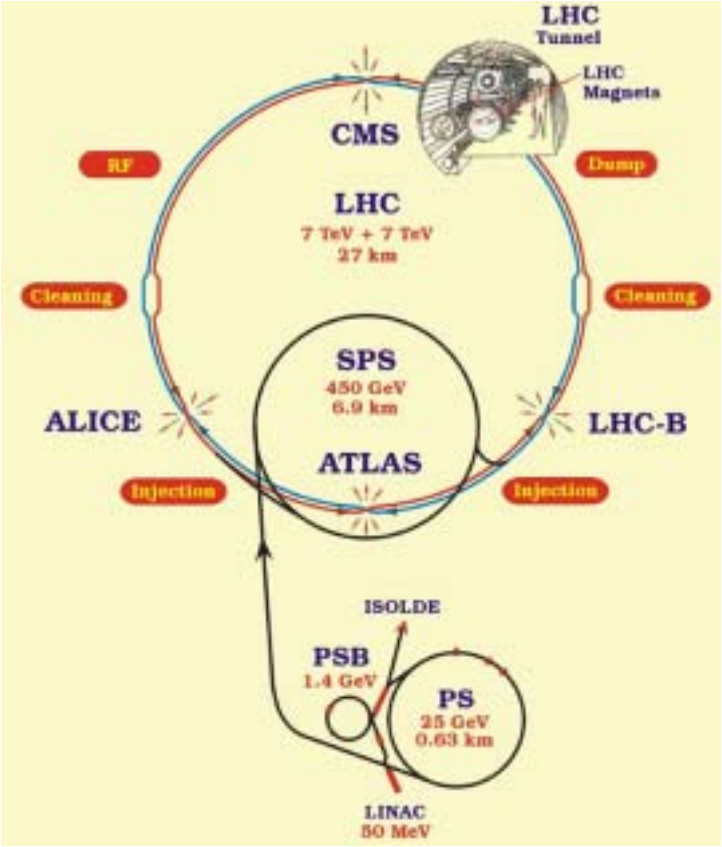

Figure 1.1: Accelerator systems of LHC

The luminosity is done by the following formula:

$$L = \frac{kN_1N_2f}{4\pi\sigma^2} \tag{1.1}$$

where N_i is the number of protons in each colliding bunch, k is the number of bunches, f is the beam revolution frequency of 1.1×10^4 Hz and σ is the transverse bunch width at the interaction point. In Tab. 1.1 some of the most relevant beam parameters are reported.

With the parameter values reported in Tab. 1.1 the Large Hadron Collider is expected to achieve a luminosity of $L = 10^{34}\text{cm}^{-2}\text{s}^{-1}$, surpassing the highest luminosity ever reached before in a hadron collider by almost two orders of magnitude. Nevertheless, for the first period of LHC running, a lower luminosity of 10^{33} cm^{-2} s^{-1} is foreseen. An integrated luminosity of 10 fb^{-1} is expected in the first year of data taking, when the LHC performances will have to be still optimized. An integrated luminosity of 100 fb^{-1} per year is expected when the high luminosity regime will be reached.

Parameter	Value
Luminosity	$10^{34} cm^{-2} s^{-1}$
Beam energy	7 TeV
Number of bunches	2808
Number of particles per bunch	10^{11}
Bunch-crossing	25 ns
Bunch spacing	7.7 cm
Bunch transverse width	16 μm

Table 1.1: Main parameters of the LHC.

1.2 LHC physics

The physics program of the LHC experiments will cover a large amount of physic topics, from the precision measurement of the Standard Model known parameters to the discovery of the Higgs boson and new physics beyond the Standard Model. The complex LHC physics program will be performed by different experiments. In particular the ATLAS and CMS detectors will operate at the high LHC luminosity of 10^{34} cm^{-2} s^{-1} and have as main goal the discovery of the Higgs field and new massive particles as the supersymmetric partners of the standard particles from proton-proton collision. In addition to these high luminosity experiments the LHC has two "low" luminosity experiments: LHCB for B-physics aiming at a peak luminosity of 10^{32} cm^{-2} s^{-1} and TOTEM for the detection of protons from elastic scattering at small angles aiming at a peak luminosity of $2{\times}10^{29}$ cm^{-2} s^{-1}. The LHC has one dedicated ion experiment, ALICE, aiming at a peak luminosity of 10^{27} cm^{-2} s^{-1}. Alice will collect data produced by Pb-Pb collisions with the goal of reproducing and understanding the properties of gluon-quark plasma.

The Standard Model The Standard Model is the theoretical framework that presently describes our knowledge of elementary particles. It describes three of the four fundamental particle interactions. The Standard Model is a gauge theory based on the invariance under transformation of the group $SU(3)_c \times SU(2)_L \times U(1)_Y$: strong interactions are carried by the gluons, the gauge bosons associated with the group $SU(3)_c$ while weak and electromagnetic interactions are carried by the bosons of the group $SU(2)_L \times U(1)_Y$, W_μ^I (I = 1, 2, 3) and B_μ, that give rise in linear combination to the massive bosons Z_0 and $W^\pm$ and to the massless boson γ. The theory does not include the effects of gravitational interactions. The matter fields are spin 1/2 fermions, corresponding to three lepton and quark families.

In addition to the matter and gauge fields, in order to spontaneously break the gauge symmetry, a scalar field (the Higgs) has to be introduced. The Higgs boson is responsible for the masses of all particles in the model. The physics of the Higgs boson is the only part of the Standard Model that has to be still confirmed by experimental evidence. The discovery of the Higgs boson is the main goal of the LHC experiments Atlas and

CMS. Despite the great theoretical and phenomenological achievements of the SM, there are different reasons to believe that this is not the definitive theory for describing the elementary particle physics. To briefly list the most important motivations for going beyond the SM, we remember that the SM:

- does not include a quantistic description of the gravitational force;
- has 19 free unpredicted parameters;
- has coupling constants that are not asymptotically free;
- does not explain the existence of three fermion families nor the strong hierarchical values of the fermion masses;
- does not take into account massive neutrinos;
- cannot explain cosmological issues like the baryon asymmetry of the universe;
- does not have a viable candidate for the cold Dark Matter of the universe;

The Standard Model is thus considered an effective theory, i.e. valid up to a certain cutoff scale. That means that it represents the low energy extension of a more complete theory.

Many models of theory beyond the SM have been studied in recent years. LHC is the most promising experimental setup capable to confirm or not such new theories. Due to its high center of mass energy and luminosity, LHC would provide indications for new physics. In Fig.1.2 the production cross sections for different processes as a function of the center of mass energy of a hadron collider are shown. The working line of LHC is also shown and clearly demonstrates how the LHC will be able to test new frontiers of physics not reachable by any other existing machine.

Supersymmetry The Supersymmetry (SUSY) is certainly the most promising theory of physics beyond the Standard Model. In the Minimal Supersymmetric Standard Model (MSSM), which is the simplest supersymmetric extension of the SM, for each SM particle there is a superpartner which differs by statistics (superpartner of a fermion is a boson and vice versa) and mass. Since on the wide spectrum of new particles predicted by the model any supersymmetric particle has been still observed, a realistic model must require supersymmetry breaking.

In the MSSM two complex Higgs field doublets are needed in order to give masses to the fermions. Assuming CP-conservation, this leads to five physical Higgs bosons: three neutral states, the two CP even h^0 and H^0 and the CP odd A, and two charged states $H^{\pm}$. The supersymmetry theory solves some of the open questions of the SM: (1) it solves the hierarchy problem. By including the superparticles, the quadratic divergence, that comes out in the evaluation of the first order radiative corrections to the Higgs propagator, becomes a logarithmic divergence; (2) it provides an explanation of the origin of the electroweak symmetry breaking; it is necessary to have a unification of the SM gauge couplings; (3) it provides a natural candidate for the Dark Matter. In order to

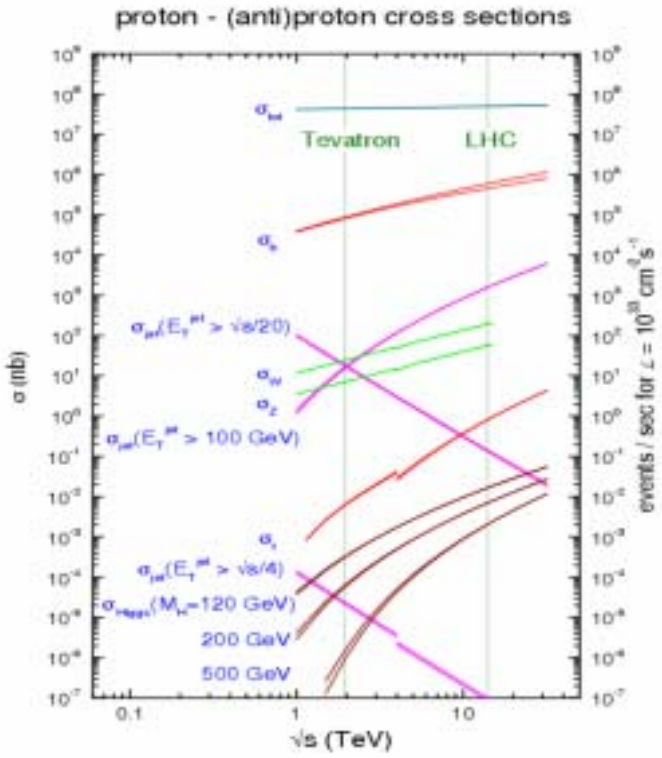

Figure 1.2: Cross section for different processes as a function of the center of mass energy.

avoid Barion/Lepton number violating terms in the superpotential, a new symmetry is introduced: the so called R-parity. The quantity $(-1)^{3(B-L)-2S}$, where S is the particle spin, has to be conserved.

1.3 The Atlas Physics program

In this section a brief description of the main physics goals of the Atlas experiment is reported.

Higgs search The Higgs boson will be produced from p-p collisions through four kind of hard scattering processes: gluon-gluon fusion, vector boson fusion, bremsstrahlung from W or Z bosons and associated heavy quark production. The correspondent Feynman diagrams are shown in Fig.1.3, where also the expected cross sections as a function of the Higgs mass are plotted. The gluon-gluon fusion process is the dominant one for the whole Higgs mass range. For Higgs mass around 1 TeV the vector boson fusion process becomes comparable with the gluon-gluon fusion. In Fig. 1.3 the present lower limit on the Higgs

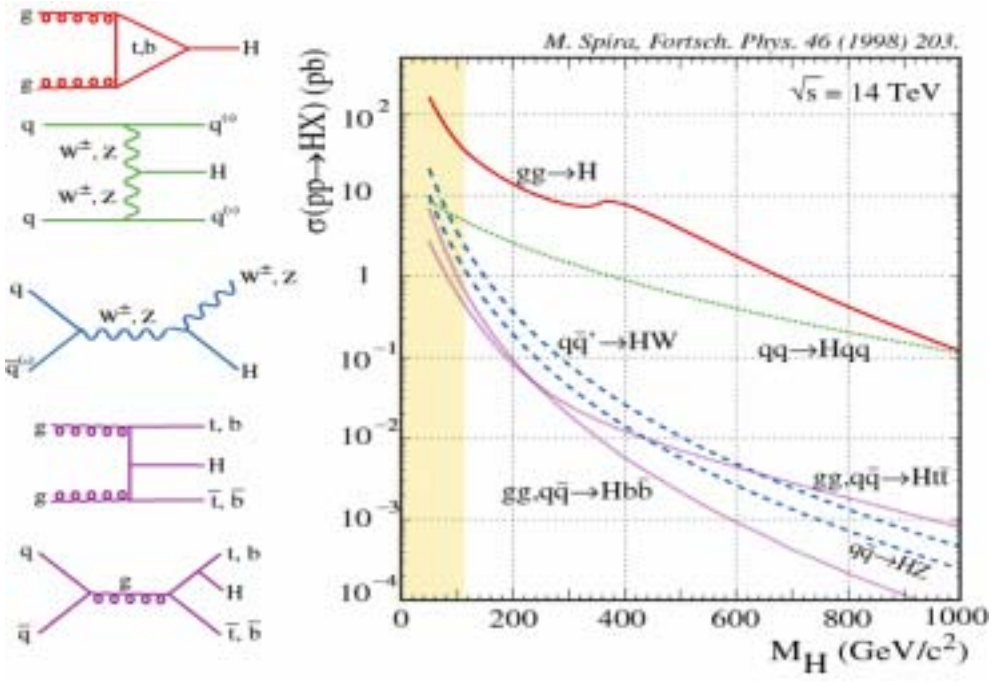

Figure 1.3: The four way to produce the Higgs boson. The corresponding production cross section is shown as a function of the expected Higgs mass.

mass is shown. It has been fixed by LEP [2] to the following value:

$$M_H > 114.1 \ GeV/c^2 \ \ at \ \ 95\% \ \ C.L. \tag{1.2}$$

The Higgs boson can decay in several ways, depending on its mass value. In Fig. 1.4 the values of the Branching Ratio of the possible decay channels of the Higgs boson are plotted as a function of the Higgs mass. We can subdivide the Higgs mass range in three zones. For each zone one decay chain is indicated as the most probable.

- $m_H < 130$ GeV: in this mass range the dominant decay channels are $H \rightarrow b\bar{b}$ and $H \rightarrow \gamma\gamma$. The decay $H \rightarrow b\bar{b}$ is dominant with a branching ratio of about 90%. Since a large two-jet background is expected the associated production with a W or Z boson or a $t\bar{t}$ pair is the only possible process to observe a signal from the $H \rightarrow b\bar{b}$ decay. In this case a high p_t lepton is produced providing the possibility to trigger on these events and reach a high rejection from QCD jet production.
  The $H \rightarrow \gamma\gamma$ decay is also possible in this mass range although with a much smaller branching ratio. In order to observe the narrow mass peak above the irreducible prompt $\gamma\gamma$ continuum background this decay requires an excellent angular and energy resolution .

- $130 < m_H < 2m_Z$: in this mass range the most promising Higgs decay is $H \rightarrow ZZ^* \rightarrow 4l$. The branching ratio for this decay is increasing up to Higgs mass values

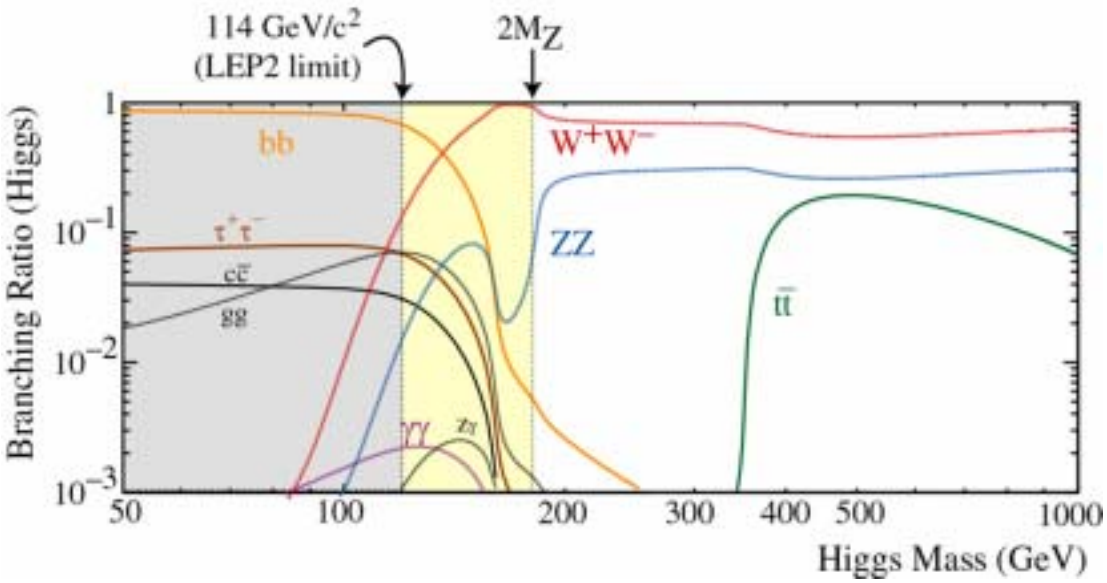

Figure 1.4: Branching Ratio of the various Higgs boson decay modes as a function of the Higgs mass.

of 180 GeV, where a pronounced dip appears due to the opening of the $H \to WW$ channel. This channel provides a clean signature since four high p_t leptons are produced and it is possible to impose the reconstructed di-muon invariant mass be consistent with the Z mass. The irreducible background is constituted by ZZ^* and $Z\gamma^*$ continuum production. The reducible background is done by $t\bar{t}$ and $Zb\bar{b}$ production. The first one has a larger production cross section with respect to the second one but the $Zb\bar{b}$ events are more difficult to reject since a Z is produced as for the signal. Moreover, a continuum background from ZZ where one Z decays into τ-pair with subsequent leptonic decay of the τ's and the other Z decays into leptons.
For Higgs masses close to 170 GeV the WW^* decay mode opens up and the $H \to WW^* \to l\nu l\nu$ branching ratio become 100 times larger than $H \to ZZ^* \to 4l$. The W decay is reconstructed through the invariant mass on the transverse plane. A reliable determination of the missing transverse energy is therefore required.

- $m_H > 180$ GeV; in this mass range the decay $H \to ZZ \to 4l$ is the most reliable channel for the discovery of the Standard Model Higgs boson. The Higgs width grows rapidly with increasing m_H and dominates the experimental mass resolution for $m_H > 300$ GeV. This channel represents the most clean signature to discover the Higgs boson since the final state is constituted by four very high p_t leptons and the constraint on the di-lepton invariant mass on the Z boson mass could be applied for both lepton pairs. The background from continuum ZZ or $\gamma^*\gamma^*$ production has a smaller cross section with respect to the signal.

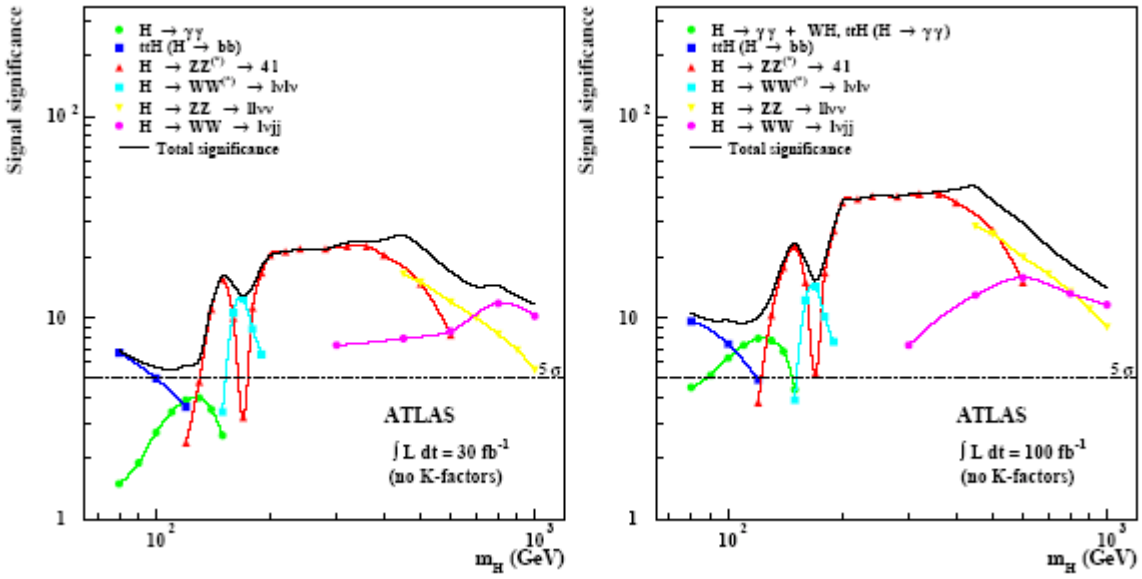

Figure 1.5: Atlas Higgs discovery significance as a function of the Higgs boson mass for different Higgs decay modes for an Atlas integrated luminosity of 30 fb^{-1} (left) and 100 fb^{-1} (right).

In Fig. 1.5 the expected signal significance, defined as the ratio $S/\sqrt{B}$ where S is the number of signal events and B the number of background events, for the different decay modes of the Higgs boson, is shown as a function of the Higgs boson mass for individual channels as well as for the combination of all channels. The significances refer to an integrated luminosity of 30 fb^{-1} and 100 fb^{-1}. The ATLAS experiment is capable of detecting a Standard Model Higgs boson with a high significance (> 5) in the mass range allowed, which extends from 114 GeV (present LEP limit) to 1 TeV. For a large fraction of the mass range considered, the Higgs boson can be discovered in at least two independent channels.

Supersymmetry The cross section of SUSY production is dominated by gluinos and squarks which are produced with cross sections comparable to the SM background. Superparticles decay after a series of steps into the LSP (Lightest Supersymmetric Particle) and involve production of multiple jets, leptons, photons, heavy quarks, W and Z bosons and missing energy. The phenomenology of the Higgs sector could be determined by just two parameters, usually chosen to be the ratio of the vacuum expectation values of the two Higgs doublets, $tan\beta$, and the Higgs mass, M_A. At least one of the neutral Higgs bosons is predicted to have a mass below the Z mass. However, radiative corrections shift this limit to about 135 GeV for a top quark mass $m_t = 175$ GeV and a soft SUSY-breaking parameter in the sfermion sector at the electroweak scale $M_{SUSY} = 1$ TeV.

For an integrated luminosity of 30 fb^{-1} the ATLAS discovery potential for the light

Higgs boson, h_0, is dominated by the vector boson fusion (VBF) production process with the $h_0 \rightarrow \tau\tau$ decay. The discovery potential for the heavier neutral Higgs boson states is given by the associated production with b quarks and the Higgs decay into a pair of muons or tau leptons (this channel cover the region of high $tan\beta$). The production of charged Higgs bosons can be observed from top quark decays for $M_{H^\pm} < 170$ GeV and from gluon bottom fusion for $M_{H^\pm} > 180$ GeV. Beyond the supersymmetric Higgs sector, the goal of the Atlas experiment is the discovery of superparticles. Typical signatures will be very high transverse momentum charged particles and high missing energy in the event.

Top physics The LHC will be a 'top quark factory' capable of producing approximately 30000 $t\bar{t}$ pairs per day. The expected cross section for the pair production of top quarks in the case of $m_t = 175$ GeV is at the next to leading order (NLO) $\sigma(t\bar{t}) = 833$ pb. This implies that more than 8 million $t\bar{t}$ pairs per year at low luminosity will be produced. This means about 470 reconstructed $t\bar{t} \rightarrow (l\nu b)(jjb)$ decays per day and about 50 clean isolated $e\mu$ pairs per day. Atlas will exploit this large production rate to perform accurate measurement of many SM parameter related to the top quark, as the measurement of the V_{tb} element of the CKM matrix via the $t \rightarrow bX$ decay. Moreover within the Standard Model an accurate measurement of the top quark mass will constrain the mass of the SM Higgs boson.

B-physics The LHC will produce a huge number of $b\bar{b}$ events thanks to the large hadronic cross section for the b quark production and the high luminosity. About one collision every hundred will produce a $b\bar{b}$ pair. This makes LHC a machine competitive with the dedicated B-physics experiments at e^+e^- colliders. The Atlas experiment has strong features for studying B-physics: a flexible trigger system, high resolution on secondary vertex measurement, highly efficient track reconstruction. The Atlas B-physics program will include the sequent topics:

- precise measurement of CP violation parameters through the decays $B^0_d \rightarrow J/\psi K^0_S$, $B^0_d \rightarrow \pi^+\pi^-$ and $B^0_d \rightarrow J/\psi\phi$. An high accurancy is expected for the measurement of the angles α and β of the unitary triangle;
- precise measurement of the periods of flavour oscillations in B^0_s and B^0_d mesons and of their relative decay rates to constrain the element of the CKM matrix;
- search and measurement of very rare decay modes which are strongly suppressed in the Standard Model. Indeed significant enhancement could provide indirect evidence for new physics. An example is the decay $B \rightarrow \mu\mu$ which implies flavour-changing neutral currents;

B-physics studies will be experimentally simpler during the first few years of LHC when the luminosity will be low and pile-up effect small. B-physics events will be initially selected by an inclusive muon trigger with a p_t threshold of 6 GeV in the pseudorapidity range $|\eta| < 2.4$.

1.4 The Lepton Flavour Violating decay $\tau \rightarrow 3\mu$

In this section a description of the Lepton Flavour Violation (LFV) phenomenology is reported in order to introduce the decay $\tau \rightarrow 3\mu$. The study of the Atlas capability in measuring the Branching Ratio (BR) of this channel is the main object of this thesis. This decay is not foreseen by the Standard Model where the mixing of the flavor families in the charged lepton sector is not allowed. Anyway decay modes with violation of the leptonic flavor are predicted by several models beyond the SM. A summary on the different models that predict non zero BR for the LFV decay of the τ lepton is presented in this section. Particular attention is dedicated to the Minimal Supersymmetric Standard Model that predicts, with a particular choice of the MSSM parameters, a BR for the $\tau \rightarrow 3\mu$ decay of the order of $\simeq 10^{-7}$ with a strong dependence on $tan\beta$.

A review of the present experimental situation on the study of the lepton flavour violating decay of the τ in three charged leptons is also reported in this section.

1.4.1 Theoretical Framework

In the minimal Standard Model with m_ν=0, the decays that violate the conservation of the lepton numbers are not foreseen. Even though there is no fundamental motivation for this lepton flavor conservation, since no symmetry is associated with the lepton family number, the lepton numbers L_e, L_μ and L_τ are separately conserved in each decay process of the SM. However recent observation of flavour oscillations in atmospheric neutrinos [3] imply that neutrinos have non zero masses and a large mixing between ν_μ and ν_τ exists. As a consequence also a family mixing in the charged leptons sector can be expected. In this new scenario only the total lepton number $L = L_e + L_\mu + L_\tau$ has to be conserved.

Even though the lepton flavour violation is allowed in the SM with $m_\nu \neq 0$, the expected branching ratios are predicted to be very small since the LFV decays, like $\tau \rightarrow \mu\gamma$, involve neutrinos and W boson one-loop intermediate states. The expected branching ratios are of the order of m_ν^2/M_W^2 that is at best 10^{-21}. This situation can dramatically change if new additional particles, carrying lepton flavour numbers and with very large masses, exist and simultaneously mix among themselves. In this case the expected branching ratios for decays such as $\tau \rightarrow e\gamma$ and $\tau \rightarrow \mu\gamma$ are enhanced and brought into the realm of observability. However, to not observe these processes will lead to strong constraints on the nature of new physics, which is expected to be present just above the electroweak scale.

On the other hand, in order to have observable lepton flavour violation, there must be new physics at or below the TeV scale. A large number of models predicts and can explain the LFV decays. In the following a not exaustive list of the principal models is reported:

- see-saw model with right-handed heavy neutrinos [6]: in this model the existence of N_R right-handed neutrinos beside the standard left-handed neutrinos is assumed. The heavy neutrinos ($M_\nu > 100$ GeV from experimental non observation) have to be considered as a possible intermediate state in the LFV violating decays. The

seesaw models predict very small branching ratios for LFV processes in most of the parameter space, although in a very restricted parameter region it can reach maximal branching ratio values such as: $BR(\tau \to \mu\gamma) < 10^{-9}$ and $BR(\tau \to 3\mu) < 10^{-10}$.

- SUSY SO(10) [7]: in this framework at least one of the neutrino Yukawa couplings is as large as the top Yukawa coupling, leading to a strong enhancement of these leptonic flavour changing decay rates. Branching ratios of the order 10^{-8} and 10^{-10} are expected for the decays $\tau \to \mu\gamma$ and $\tau \to 3l$ respectively.

- non-universal Z': there are many models beyond the standard model predicting the existence of non-universal gauge bosons Z', which can give rise to very rich phenomena. The contributions of the non-universal gauge bosons Z', predicted by topcolor-assisted technicolor (TC2) models and flavor-universal TC2 models, to the lepton flavor-violation tau decays has been calculated [8]. The authors find a branching ratio $BR(\tau \to 3l)$ larger than that of the process $\tau \to \mu\gamma$ for all the parameter space. Over a sizable region of the parameter space, they have found $BR(\tau \to 3l) \simeq 10^{-8}$ which may be detected in the future experiments.

- MSSM [10, 12, 11]: a natural framework, where several LFV signals can be significant, is the Minimal Supersymmetric extension of the Standard Model (MSSM). Supersymmetry provides new direct sources of flavor violation since it is possible to have off-diagonal terms in the sleptons[1] mass matrix. This LV in the slepton sector can be communicated to the charged leptons through the exchange of Higgs bosons [9, 12]. Since the sleptons are expected to have mass around the TeV scale, if flavour mixing is present in the slepton sector, large branching ratios are expected for the lepton flavour violating decays. This model predicts branching ratios of the order of $10^{-7} - 10^{-8}$ that are strongly dependent on the MSSM parameters.

In the last part of this section, the mechanism by which the lepton flavour violation can occur as mediated by a supersymmetric neutral Higgs boson will be explained in more detail. In this case the predicted branching ratio of the $\tau \to 3\mu$ process results a particular sensitive probe of LFV.

LFV in MSSM The MSSM contains two Higgs doublets, H_1 and H_2, with opposite hypercharges. Charged leptons only couple with the H_1 field at the tree level and the lagrangian is written as:

$$L = -Y_\mu H_1^0 \mu^c \mu - Y_\tau H_1^0 \tau^c \tau + h.c. \tag{1.3}$$

where H_1^0 is the neutral component of the H_1 and Y_μ, Y_τ are the Yukawa coupling constants. After the inclusion of radiative corrections the downtype fermions interact also

[1] The supersymmetric partners of the leptons that carry the same flavour quantum numbers of the SM leptons.

with the H_2 field and the coupling could be either flavour conserving (FC):

$$L_{FC} = -(Y_\mu \Delta_\mu + Y_\tau \Delta'_\mu) H_2^{0*} \mu^c \mu - Y_\tau \Delta_\tau H_2^{0*} \tau^c \tau + h.c. \tag{1.4}$$

or flavour violating (FV):

$$L_{FV} = -Y_\tau \Delta_L H_2^{0*} \tau^c \mu - Y_\tau \Delta_R H_2^{0*} \mu^c \tau + h.c. \tag{1.5}$$

This last term can be expressed as a function of the leptons and higgs mass eigestates as:

$$L_{FV} = -\frac{Y_\tau}{\sqrt{2} cos\beta} (\Delta_L \tau^c \mu + \Delta_R \mu^c \tau)[h^0 cos(\beta - \alpha) - H^0 sin(\beta - \alpha) - iA^0] + h.c. \tag{1.6}$$

where $tan\beta =< H_2^0 > / < H_1^0 >$, α is the mixing angle in the CP-even Higgs sector and Δ_μ, Δ'_μ, Δ_τ and Δ_L, Δ_R are dimensionless functions of the MSSM mass parameters. The matrices Δ_L and Δ_R take into account the one-loop diagrams with the exchange of gauginos, neutralinos and sleptons that are shown in Fig. 1.6. Explicit expressions of Δ_L and Δ_R are reported in [12]. The effective couplings (eq. 1.6) contribute to LFV low-energy processes, such as the decay $\tau \to 3\mu$ and other ones, through Higgs boson exchange, Fig.1.7.

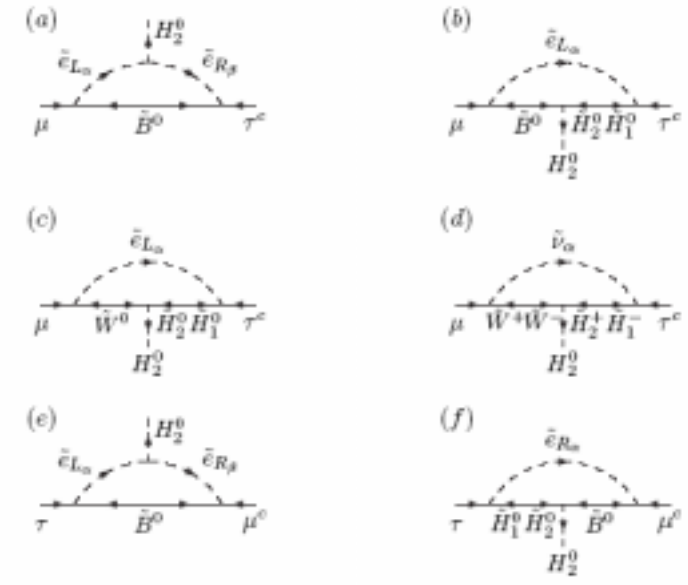

Figure 1.6: Diagrams that contribute to Δ_R and Δ_L

The expected branching ratio is not far from the regime experimentally accessible by the LHC experiments:

$$BR(\tau \to 3\mu) = 10^{-7} \left(\frac{tan\beta}{50}\right)^6 \left(\frac{100GeV}{m_A}\right)^4 \left(\frac{|50\Delta_L|^2 + |50\Delta_R|^2}{10^{-3}}\right), \tag{1.7}$$

and depends strongly on the values of the MSSM parameters as $tan\beta$ and the higgs mass. If the higgs spectrum is relatively light ($m_A < 300$ GeV), future collider, in particular LHC may be able to detect the $\tau \rightarrow 3\mu$ decay.

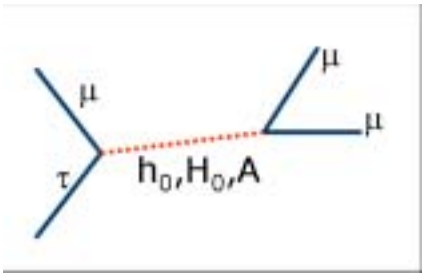

Figure 1.7: Feynman diagram for the $\tau \rightarrow 3\mu$ decay mediated by a neutral Higgs boson.

1.4.2 Experimental results

The abundance of theoretical models predicting a non zero branching ratio for the LFV decays of the τ lepton, and the important role that these branching ratio values could have in constraining the parameters of such models, have motivated a lot of experiment searches of these decays in the last years.

First searches have been performed by the CLEO collaboration, then followed by improved determination of the U.L. on the BR($\tau \rightarrow 3\mu$) by the experiments at the B-factories. In the following a review of the experimental results on the search of the LFV decay $\tau \rightarrow 3\mu$ is presented.

CLEO The Cleo collaboration has analyzed a sample of 4.79 fb^{-1} of data collected at the CLEO II detector at CESR, looking for three charged body decays of the τ [14]. Tau leptons are produced in pairs in e^+e^- collisions at a center of mass energy of about 10.6 GeV. The number of produced τ pairs is 4.37×10^6. The search method is the following: signal candidate τ decays are required to produce three reconstructed tracks in the detector (3-prong decay) while the other τ in the event must decay into a 1-prong mode, and the total visible charge must be zero. They have set an upper limit on BR($\tau \rightarrow 3\mu$) to 1.9×10^{-6} at the 90% C.L., according to the convention adopted by the Particle Data Group. This result represents the present limit reported in the PDG [13].

BABAR The Babar detector is dedicated to the physics of the B-$\bar{B}$ mesons system produced at the PEP-II B-factory. The PEP-II B-factory is an asymmetric e^+e^- collider designed to operate at a luminosity of 3×10^{33} cm^{-2} s^{-1} and above, at a center of mass energy of 10.58 GeV, the mass of the $\Upsilon(4S)$ resonance. Although the primary physics goal of the Babar experiment is the systematic study of CP-violating asymmetries in the decay of neutral B mesons to CP eigenstates, precise measurements of decays of bottom, charm mesons and τ leptons, and searches for rare processes have been carried out.

The Babar collaboration has published results on the search for LFV τ decays in three charged leptons [15]. They have analyzed a sample of 91.5 fb^{-1} of integrated luminosity, that with a τ-pair production cross section of $\sigma(\tau\tau) = (0.89 \pm 0.02)$ nb, corresponds to over 160 million τ decays. The signature of this process is three charged particles, each identified either as an electron or as a muon, with an invariant mass and energy equal to that of the parent τ lepton. Candidate signal events in this analysis are required to have a '1-3 topology', where one tau decay yields three charged particles (3-prong), while the second tau decay yields one charged particle (1-prong). Four well reconstructed tracks are required with zero net charge, pointing toward a common region consistent with $\tau^+\tau^-$ production and decay. One of these tracks must be separated from the other three by at least 90° in the CM frame. The plane perpendicular to this isolated track divides the event into two hemispheres and defines the 1-3 topology.

With the high statistics available, they have set an upper limit on the τ decay mode in three leptons final state, taking into account all the six possible combinations consistent with charge conservation ($e^-e^+e^-, \mu^+e^-e^-, \mu^-e^+e^-, e^+\mu^-\mu^-, e^-\mu^+\mu^-, \mu^-\mu^+\mu^-$) to (1-3)$\times 10^{-7}$ at 90% C.L.. In particular the upper limit on the decay mode $\tau \to 3\mu$ has been set to 1.9×10^{-7} at 90% C.L. improving the previous result from Cleo by one order of magnitude.

BELLE A very similar analysis on the rare three body decay of the τ into three charged leptons has been performed also by the Belle collaboration. The Belle detector, at the KEKB asymmetric energy e^+e^- collider operating at a center-of-mass energy $\sqrt{s} \simeq 10.6$ GeV, is dedicated to the study of the CP violation in the $B\bar{B}$ meson system. They have analyzed a data sample of 87.1 fb^{-1} corresponding to (79.3±1.1) million τ-pairs collected finding an upper limit on the branching ratio of 2.0×10^{-7} at 90% C.L..

Summary In Tab. 1.2 a summary of the results of the analysis of the $\tau \to 3\mu$ decay from the experiments Cleo, Babar and Belle is reported. Together with the final upper limit on the branching ratio published by the three collaborations, the number of expected background events and the number of signal and background events collected are also reported. The number of signal events, and thus the signal branching ratio, has been determined using the number of expected background events and the number of observed signal and background events using the prescription of Feldman and Cousins [17].

Experiment	Detection Efficiency	N_{obs}	Expected N_{bgd}	UL	C.L.
CLEO	15.0	0	0.11	1.9×10^{-6}	90%
Babar	6.7±0.5	0	0.31±0.09	1.9×10^{-7}	90%
Belle	9.0±1.6	0	0.1±0.1	2.0×10^{-7}	90%

Table 1.2: Upper limit on BR($\tau \to 3\mu$) set by the Cleo, Babar and Belle collaborations.

Chapter 2

The ATLAS Detector

2.1 Overall Description

The Atlas experiment has been designed to explore the high energy physics frontier at the TeV scale and to investigate the physics of the Standard Model and beyond, at the Large Hadron Collider. The Atlas detector has a cylindrical symmetry along the beam axis, with a total length of 42 m and an external radius of 11 m. It is made of layers of different technologies. The construction has started in 1998 and will be completed in the year 2006.

For the description of the Atlas detector the following right-handed system of coordinates will be used: the z axis is the one parallel to the proton beams, the x axis pointing toward the center of the LHC circumference and the y axis is the vertical one pointing toward the ground level. ϕ is the azimuthal angle while θ is the polar one. As customary in the experiments at hadron colliders, the pseudorapidity variable will be used instead of θ because it is independent on Lorentz boosts along the beam axis. The pseudorapidity is defined as:

$$\eta = -\ln\left(\tan\left(\frac{\theta}{2}\right)\right). \tag{2.1}$$

The Atlas detector has been designed to offer very high quality performances in the detection of particles. In particular high resolution electromagnetic calorimeter system for electron and photon identification and good hadronic calorimeters to accurately measure the jet momentum and the event missing transverse energy are required. As it has been shown in the previous chapter, high momentum final state muons are the most promising and robust signatures for the physics at the LHC. For this reason very high precision measurement of transverse momentum of muons on a wide range of momenta is required together with large acceptance in η and almost full ϕ coverage. This is provided by the Muon Spectrometer that is the outer part of Atlas. A very good trigger capability for particles at low p_t threshold is needed. In Fig.2.1 an overall layout of the Atlas detector

is presented. Its various parts are in order:

- Magnetic Systems: the magnet configuration is based on an inner superconducting solenoid surrounding the Inner Detector cavity which bends the charged particles in the internal tracker, and large superconducting air-core toroids consisting of independent coils arranged with an eight-fold symmetry outside the hadronic calorimeter system in order to bend muons in the muon spectrometer;

- Inner Detector: is contained within a cylinder of length 6.80 m and radius 1.15 m, with a solenoidal magnetic field of 2 T. Pattern recognition, momentum and vertex measurements and enhanced electron identification are achieved with a combination of discrete high-resolution pixel and strip detectors in the inner part and continuous straw-tube tracking detectors with transition radiation capability in the outer part of the tracking volume;

- Calorimeters: the Atlas calorimeter consists of an electromagnetic calorimeter covering the pseudorapidity region $|\eta| < 3.2$, barrel hadronic calorimeter covering $|\eta| < 1.7$, hadronic endcap calorimeters covering $1.5 < |\eta| < 3.2$ and forward calorimeters covering $3.1 < |\eta| < 4.9$. The EM calorimeter is preceded in the range $|\eta| < 1.8$ by a presampler detector, installed immediately behind the cryostat cold wall.

- Muon Spectrometer: the muon spectrometer is the outer part of the Atlas detector and has been designed to offer very high quality performances in the measurement of the transverse momentum of muons. The air-core toroid system, with a long barrel and two inserted end-cap magnets, generates a large field volume and strong bending power with a light and open structure. Multiple scattering effects are therefore minimal, and an excellent muon momentum resolution is achieved with three stations of high-precision tracking chambers. The muon instrumentation is complemented with fast trigger chambers.

In the following paragraphs the main characteristics of the Atlas sub-detectors will be described, with particular attention on the Muon Spectrometer.

2.1.1 The Atlas magnetic systems

The magnetic system of Atlas [19] consists of a central solenoid that provides magnetic field for the inner tracker and a system of three large air-core toroids (one barrel toroid and two endcap toroids) that provide magnetic field for the muon spectrometer.

The solenoid is a superconducting magnet placed inside the calorimeter system. It is kept at a temperature of 4.5K and is contained in the same cryostat of the electromagnetic calorimeter. In order to minimize the material in front of the calorimeter the solenoid is shorter than the inner detector producing some non uniformity in the magnetic field along the z direction. The field varies from 2T near z=0 to 0.5T at the end of the inner detector.

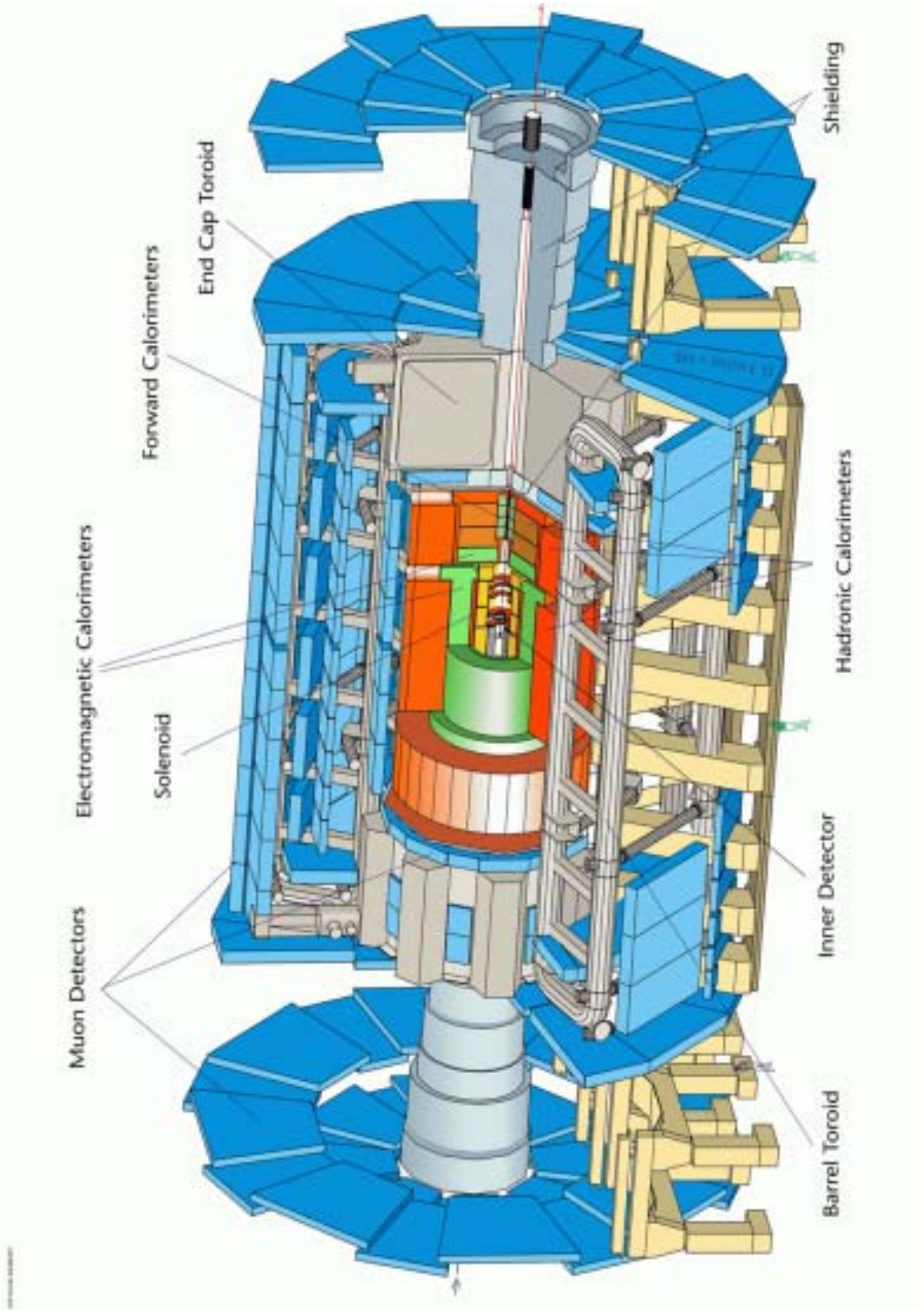

Figure 2.1: Layout of the Atlas experiment

The toroidal magnetic system has been designed to produce a high magnetic field in a large volume in a pseudo-rapidity range $0 < |\eta| < 2.7$. The barrel toroid consists of eight coils assembled radially and symmetrically around the beam axis. Each coil have a length of 25 m. The end-cap toroid are rotated in the azimuthal direction by an angle of 22.5° to provide radial overlap and to optimize the bending power in the transition regions. The eight barrel coils are contained in individual cryostat while the eight endcap coils are enclosed in the same cryostat. As shown in Fig.2.2, the bending power provided by the toroidal magnetic system is not uniform varying the pseudorapidity. The magnetic field provides typical bending powers of 3 Tm in the barrel and 6 Tm in the endcaps.

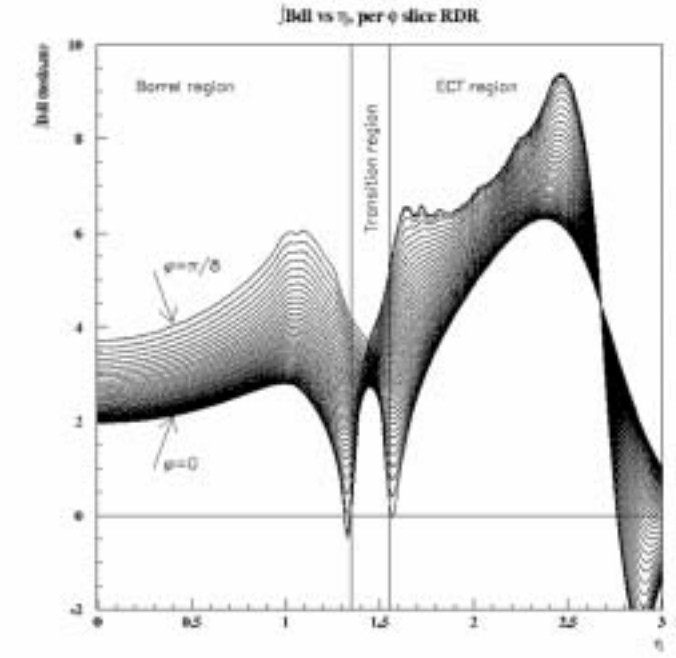

Figure 2.2: Toroidal magnet system bending power.

2.1.2 Inner Detector

Given the very large track density expected at the LHC (in the high luminosity regime $\simeq 20$ minimum bias events per bunch crossing and $\simeq 1000$ charged tracks per event are expected) a fine granularity is required in order to measure track momentum and vertex position with high resolution and efficiency.

The Atlas Inner Detector [20, 21] has been designed to satisfy the following physics requirements: very high momentum and impact parameter resolution for charged tracks with $p_t > 0.5$ GeV up to very high momenta; acceptance coverage over the range $|\eta| < 2.5$; high efficiency with good noise rejection; charge identification for high-p_t tracks; tagging

of b jets originated by b quarks; good resolution in the measurement of the event primary vertex and secondary vertexes from b quark.

In order to measure the track momentum the Inner Detector (ID) is contained in the solenoidal magnetic field described in the previous section. In Fig.2.3 a layout of the Atlas ID is shown. The outer radius of the ID cavity is 1.15 m. It is constituted by a barrel that extends over ±80cm and two identical endcaps. In the barrel region detectors are arranged in concentric cylindrical layers around the beam axis, while in the endcaps detectors are mounted on disks perpendicular to the beam axis. In the innermost region very high granularity is provided by pixel detectors. The middle region is composed by the Semiconductor Tracker (SCT), while in the outermost part a Transition Radiation Tracker id used.

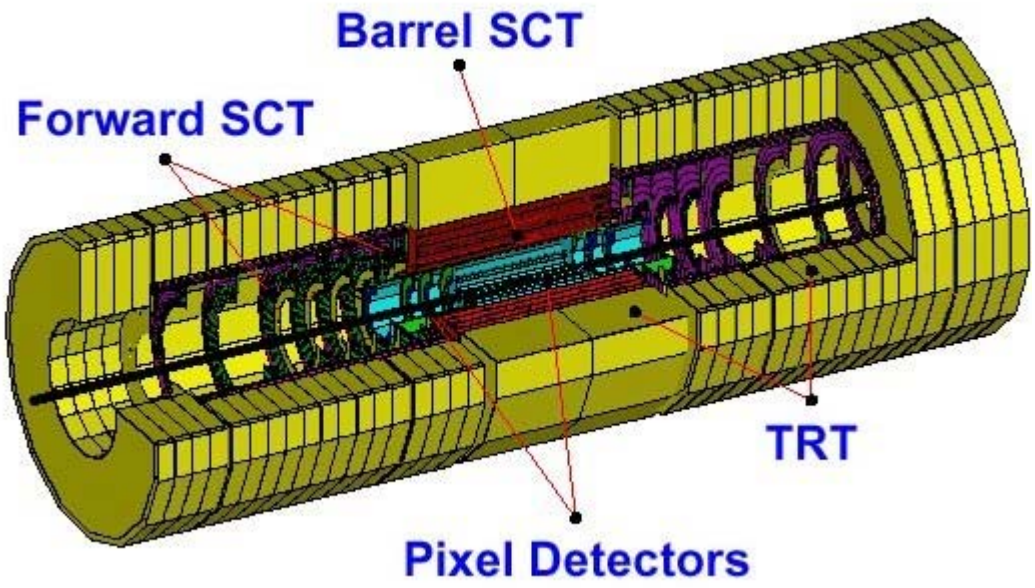

Figure 2.3: Layout of the Atlas Inner Detector

The pixel detector The pixel detector (Fig. 2.4) is designed to provide very high granularity as close to the interaction point as possible. The system consists of three barrels at radii of ≃4 cm, 10 cm and 13 cm respectively and three rings on each side with 11 cm inner radius and 20 cm outer radius, covering the pseudorapidity range of $|\eta| < 2.5$. The pixels size is 50 μm in the rϕ plane and 300 μm along the z axis. The system contains a total number of 140 millions detector elements. The readout system is composed by chips with individual circuits for each pixel element, including buffering to store the data while awaiting the level-1 trigger decision. The chips must be radiation hardned to stand over 300 kGy of ionising radiation and over 5×10^{14} neutrons per cm^2 in

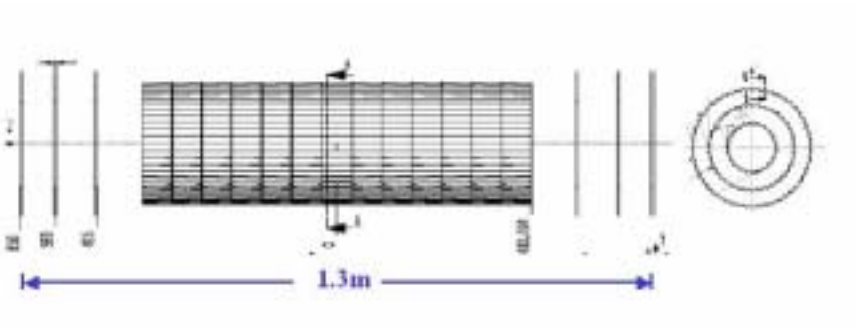

Figure 2.4: Layout of the pixel detector.

ten years of operation. The thickness of each layer is about 1.7% of the radiation length (X_0) at normal incident angle. The position resolution that is achieved with this high granularity is about 10 μm in the rϕ plane and 50 μm along z, allowing the track origin to be reconstructed and secondary decay vertices to be found.

A hit corresponds to a single pixel cell which collects an amount of charge above a given threshold. The occupancy, defined as the number of hits per electronic channel per event, has to be very small in order to avoid single channel efficiency deterioration. The average occupancy for minimum bias events at the design LHC luminosity of $10^{34}\text{cm}^{-2}\text{s}^{-1}$ has been estimated of the order of 10^{-4} for the middle and outer layers and 4 time more for the inner one.

The pixel detector provides an excellent transverse impact parameter resolution for short-lived particles as B hadrons and τ lepton and a very good three dimensional vertex identification. It also has a very good b-tagging and b-triggering capability.

The Semiconductor Tracker The semiconductor tracker (SCT) system is designed to provide eight precision measurements per each track in the intermediate radial range of the inner detector, contributing to the measurement of the track momentum, impact parameter and vertex position. The barrel SCT provides high granularity using eight layers of silicon micro-strips (80 μm pitch) to determine the track position in the rϕ plane. Using a small stereo angle it is possible to obtain also the z coordinate. Two SCT endcaps, similar in construction to the barrel, are placed to each end of the barrel module. The detector contains 6.2 million readout channels. The spatial resolution provided by the SCT system is 16 μm in rϕ and 580 μm in z. The SCT system can individuate tracks separated by $\simeq$ 200 μm distance.

The Transition Radiation Tracker The Transition Radiation Tracker (TRT) provides continuos tracking at large radius of the inner detector of Atlas. It consists of a barrel part containing $\simeq$ 52000 axial straws of about 150 cm length, each divided in two at the center in order to reduce the occupancy and read out at each end, and of two endcap parts containing $\simeq$ 320000 radial straws of 39 cm length. All charged particle tracks with

$|\eta| < 2.5$ and $p_t > 0.5$ GeV will cross about 40 straws.

The thin proportional drift tubes (straws) have a 4 mm diameter, this value is a reasonable compromise between speed of response, number of ionization clusters and mechanical stability, guarantying a high modularity for the overall detector. Each straw is equipped with a 30 μm diameter gold-plated W-Re wire for reading the electronic signal. The detector can operate at the very high rates expected at the LHC due to the small diameter of the sense wires and their isolation within the individual gas volumes. Each channel provides a drift time measurement with a spatial resolution of 170 μm per straw. The large number of straws per track guarantees a measurement accurancy better than 50 μm averaged over all straws at the LHC design luminosity. Electron identification capability is obtained by employing xenon gas to detect transition-radiation photons created in a radiator between the straws. This technique is intrinsically radiation hard. The electron-pion power rejection for particles with p_t= 20 GeV is 10^{-2}.

Inner detector combined performances The combination of the three tecnologies of the Inner Detector provides a very robust pattern recognition and high precision in both ϕ and z coordinates. All tracks with $|\eta| < 2.5$ are measured with six precision space points and about 36 straws, except for a slight degradation across the barrel to endcap transition regions. Above $|\eta| = 1.8$, tracks leave the ID volume before reaching the maximum radius of the cavity, thereby reducing the field integral available as compared to the lower η regions. This effect limits the momentum resolution achievable in the endcap regions. The resolution in the measurement of the transverse track momentum is shown in Fig.2.5 as a function of η.

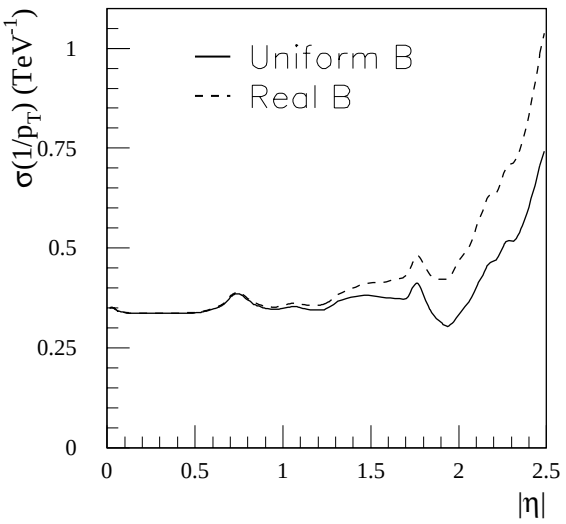

Figure 2.5: Resolution of the Atlas Inner Detector in the measurement of the track p_t as a function of η.

The momentum resolution is limited by several factors: the radial space available in

the cavity, which limits the lever arm, the strength of the magnetic field, and the intrinsic precision of the detector elements. At high momenta the impact parameter of the track to the primary vertex can be measured with a precision smaller than 15 μm. At lower momenta multiple scattering effects lower it at 60 μm. Tracks with $p_t < 0.5$ GeV will spiralize along the axis and will not be reconstructed.

2.1.3 Calorimeters

The main tasks of the ATLAS calorimetric system are:

- precise measurement of energy and position of electrons and photons;
- measurement of energy and direction of jets;
- measurement of the missing transverse momentum of the event;
- particle identification (separation of electrons and photons from hadrons and jets).

Good performances are required in the whole energy range extending from a few GeV up to the TeV scale. Due to the hard conditions in which the LHC experiments will operate (large fraction of pile-up events) fast detector response (< 50 ns) and fine granularity are required. High radiation resistance is also needed given the high particle fluxes expected over a period of operation of at least ten years. Overall calorimetry coverage up to $|\eta| \simeq 4.9$ is necessary for high quality measurement of the missing transverse energy and to increase the acceptance for jet tagging.

The layout of the Atlas calorimetric system is shown in Fig.2.6. Starting from the inside it consists of an electromagnetic calorimeter covering the pseudorapidity region $|\eta| < 3.2$, barrel hadronic calorimeter covering $|\eta| < 1.7$, hadronic endcap calorimeters covering $1.5 < |\eta| < 3.2$ and forward calorimeters covering $3.1 < |\eta| < 4.9$. The EM calorimeter is preceded in the range $|\eta| < 1.8$ by a presampler detector, installed immediately behind the cryostat cold wall.

The Electromagnetic calorimeter The performance specifications for the EM calorimeter come from a few benchmark channels: the search for a Higgs boson through the decays $H \to \gamma\gamma$ and $H \to 4e$, and the search for haevy vector bosons, W' and Z', with masses up to 5-6 TeV. Since the energy resolution of the EM calorimeter improves with increasing energy the best sensitivity for observing this particles is achieved through the electron decay modes $W' \to e\nu$ and $Z' \to e^+e^-$, where the produced electrons have very high momenta. A very good electron reconstruction capability for high energy electrons (up to 5 TeV) is needed to search for electrons from the W' or Z'. Good electron reconstruction capability for low energy electrons (1-2 GeV) is necessary for the study of the semileptonic decay of b quarks in order to increase the total b-tagging efficiency by about 10%, important in the search of $H \to b\bar{b}$ decays, SUSY decays and B-physics.

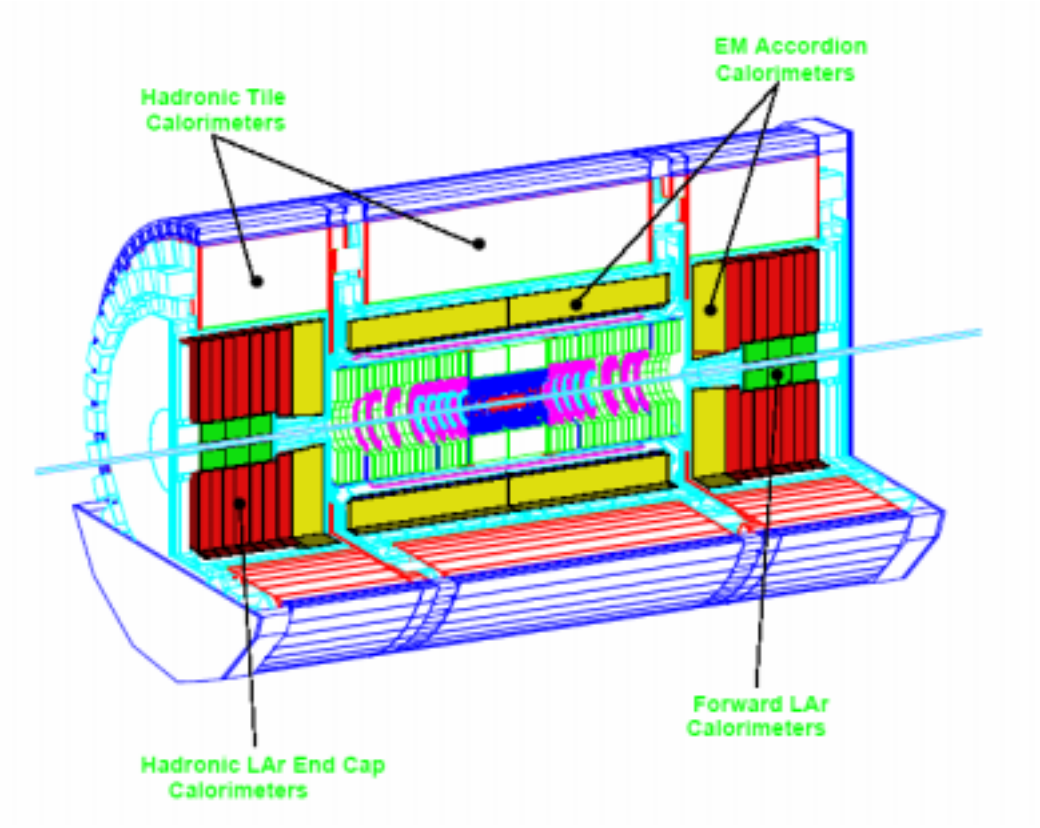

Figure 2.6: Layout of the Atlas calorimeter system.

An excellent energy resolution and linearity response better than 0.5% are needed in the energy range 10-300 GeV to achieve a mass resolution of $\simeq 1\%$ for the $H \to \gamma\gamma$ and $H \to 4e$ channels in the mass region 90-180 GeV. A constant resolution term of few % will assicurate a detector resolution smaller than the Z' intrinsic width ($\Gamma_{Z'} = 10$ GeV for $m_{Z'} = 1$ TeV in the framework of Extended Gauge Theories [22].)

The electromagnetic calorimeter is a lead/Liquid-Argon (LAr) sampling detector [23] with accordion shaped kapton electrodes and lead absorber plates. As it is shown in Fig. 2.7, the thickness of the lead absorbers varies as a function of the pseudorapidity to optimize the energy resolution and provide complete ϕ symmetry. The barrel of the electromagnetic calorimeter covers up to $|\eta| < 1.5$ and the two endcaps cover $1.4 < |\eta| < 3.2$.

In the pseudorapidity range $|\eta| < 1.8$, a presampler detector installed immediately behind the cryostat cold wall is placed in front of the EM calorimeter. It is used to correct for the energy lost in the material upstream of the calorimeter (inner detector, cryostats, coils $\simeq 2X_0$ at η=0).

The total thickness of the EM calorimeter is above $24X_0$ in the barrel and above $26X_0$ in the endcaps. This is required to keep to an acceptable level the contribution to the energy resolution coming from longitudinal fluctuations of high energy showers not

fully contained in the calorimeter. Particle identification, accurate position measurement, response speed, low noise and good energy resolution require a transverse granularity not coarser than $\Delta\eta \times \Delta\phi = 0.03 \times 0.03$ over the rapidity region $|\eta| < 2.5$.

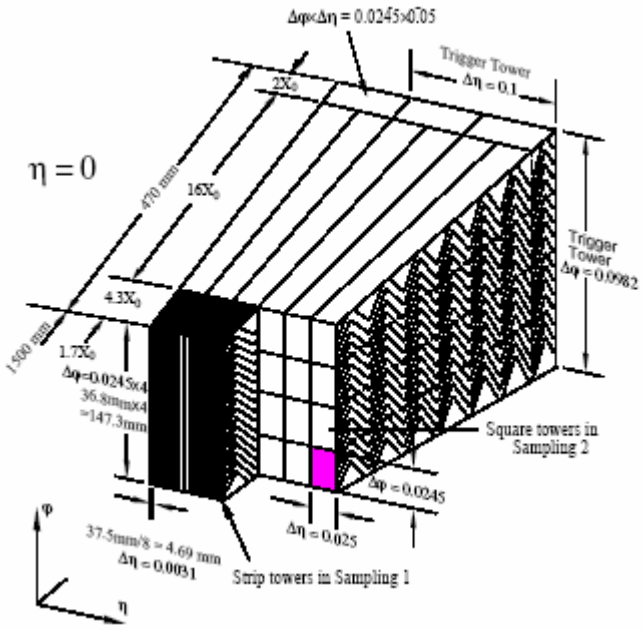

Figure 2.7: Accordion structure of the LAr EM calorimeter.

The energy resolution provided by the electromagnetic calorimeter of Atlas is given by:

$$\frac{\sigma(E)}{E} = \frac{10\%}{\sqrt{E(GeV)}} \oplus 1\% \tag{2.2}$$

The measurement of the shower direction in θ has a resolution of $\simeq$50 mrad$/\sqrt{E(GeV)}$.

The hadronic calorimeter The main hadronic calorimeter tasks are the reconstruction of jets and the measurement of the event missing E_T. Moreover at low luminosity the aim is to approach a 1% error on the top quark mass reconstruction, while, at high luminosity, the goal is the detection of a heavy Higgs boson decaying into a high-p_t W with successive decay $W \rightarrow jj$.

The E_T^{miss} plays an essential role from two different points of view: a good resolution is necessary for the $\tau\tau$ mass reconstruction for the detection of the $H \rightarrow \tau\tau$ decay, a very good control of the tails of the transverse missing energy distrubution is required to keeping low the level of fake E_T^{miss} background. This background effects the search of SUSY particles and of the Higgs boson through the decay $H \rightarrow ZZ \rightarrow ll\nu\nu$.

The Atlas hadronic calorimeter [24] covers the range of $|\eta| < 5$ in order to extend jet detection and allow an efficient tagging of the forwards jets associated to the production of heavy Higgs. Moreover this implies an overall good E_T^{miss} resolution. Different techniques

are used over the wide η range to best suite the widely varying requirements and radiation environment.

The hadronic barrel calorimeter is a cylinder divided in three sections, a central barrel and two identical extended barrels with an inner radius of 2.28 m and an outer radius of 4.23 m. It is based on a sampling technique with plastic scintillator plates (tiles) embedded in an iron absorber. The tiles are placed perpendicular to the colliding beams, staggered in depth and segmented in three layers. The structure is periodic in z. The barrel and extended barrels are divided in 62 modules in the azimuthal coordinate, in η the read out cells built by grouping fibers into a photomultiplier are pseudo-projective to the interaction region. The most stringent transverse granularity requirement comes from the $W \rightarrow jj$ decay at high p_t and applies for $|\eta| < 3$, where a granularity of $\Delta\eta \times \Delta\phi = 0.1{\times}0.1$ is needed. At larger pseudorapidity regions a granularity of $\Delta\eta \times \Delta\phi = 0.2{\times}0.2$ is sufficient.

For the hadronic calorimeter a total thickness of about 10 interaction lenght (λ) is required for shower containment and reduction of punch through. This reduces the background in the muon system.

At larger pseudo-rapidities, where higher radiation resistance is needed, the LAr technology is used. Hadronic LAr calorimetry covers the endcap and forward regions in the range $1.5 < |\eta| < 4.9$. Each hadronic endcap calorimeter consists of two equal diameter wheels built out of copper plates.

The forward calorimeter is integrated in the endcap cryostat at about 5 m from the interaction point. It has to accommodate at least 9 interaction lengths of active detector in a short longitudinal space, and thus it is a high density detector, consisting on three longitudinal sectors. The first is in copper, the other in tungsten.

The expected energy resolution for the hadronic calorimeter is:

$$\frac{\sigma(E)}{E} = \frac{50\%}{\sqrt{E(GeV)}} \oplus 3\% \qquad for \;\; |\eta| < 3 \tag{2.3}$$

$$\frac{\sigma(E)}{E} = \frac{100\%}{\sqrt{E(GeV)}} \oplus 10\% \qquad for \;\; 3 < |\eta| < 5 \tag{2.4}$$

2.2 The Muon Spectrometer

2.2.1 Physics requirements

The main requirements for the Atlas Muon Spectrometer are dictated by some benchmark reactions that produce one or more high momentum muons in the final state. The most important are:

- $H \rightarrow ZZ^* \rightarrow \mu\mu ll$: discovery channel for the Standard Model Higgs boson in the mass range from 130 to 170 GeV. Since the natural Higgs width increases with the Higgs mass (Fig.2.8), and in this mass range is very narrow, and the physics

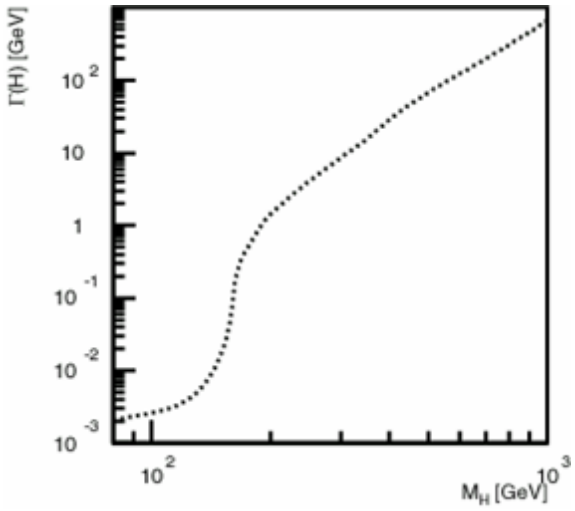

Figure 2.8: Higgs width as a function of its mass.

backgrounds are severe, a mass resolution at the level of 1% is needed for adequate signal sensitivity;

- $H/A \rightarrow \mu\mu$: discovery channel for the Minimal SuperSymmetric Model Higgs;
- Z', W': new vector bosons production, in their leptonic decay modes, will produce muons with transverse momentum up to several TeV.
- beauty physics: the muon spectrometer is used primarily as a LVL1 muon trigger and as a muon identifier for channels where a muon is produced in the decay of at least one B hadron. In the typical p_t range of such decays ($1 < p_t < 30$ GeV), the momentum resolution of the inner tracker is better than that of the muon spectrometer; the muon chambers are therefore mainly used to validate the muon candidate and match it with the inner detector track.

2.2.2 Background conditions

The background rate in the Muon Spectrometer, due both to physical events or radiation background, is an important parameter since it can influence the trigger performance and the track reconstruction efficiency of the spectrometer.

Primary background It consists of primary collision products penetrating into the muon spectrometer through the calorimeters, correlated in time to the primary pp interaction. Conventional sources of primary background are semileptonic decays of light (K,$\pi \rightarrow \mu$X) and heavy (c,b,t$\rightarrow \mu$X) flavours, gauge boson decays (W,Z,$\gamma \rightarrow \mu$X), shower muons and hadronic punch-through. At small p_t below 10 GeV, the largest component of the background are muons from π/K decays in flight. Depending on pseudorapidity, muons with momenta of 3-6 GeV will be absorbed in the calorimeters. At moderate p_t,

between 10 and 30 GeV, the cross-section is dominated by charm and beauty decays. At larger p_t, above 30 GeV, top and Z decays also give a sizable contribution. In Fig. 2.9 (left) the muon production cross sections are plotted as a function of the muon momentum.

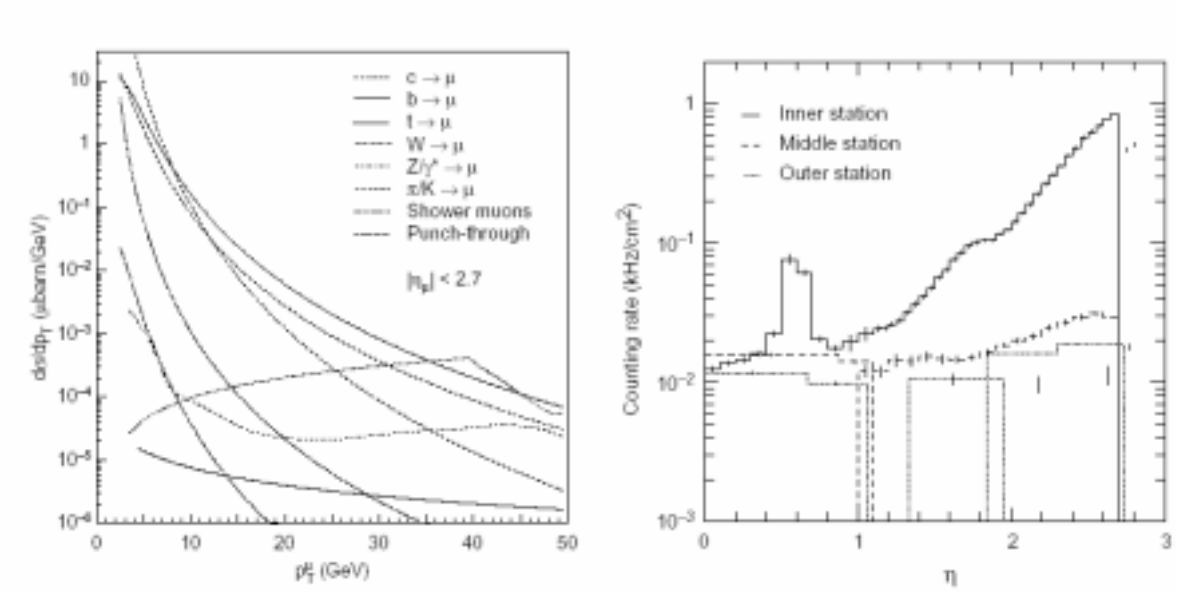

Figure 2.9: Left: Production cross sections for muons from different sources as a function of the muon p_t. Right: Pseudorapidity dependence of the total counting rate in the three precision chamber station at nominal luminosity.

Radiation background This background consists mostly of neutrons and photons in the 1 MeV range, produced by secondary interactions in the forward calorimeter, shielding material, beam pipe and machine elements. Low-energy neutrons, which are an important component of the hadronic absorption process, escape the absorber and produce a low-energy photon background. This background enters into the spectrometer from all directions and is not any longer correlated in time to the primary pp interaction. Using the MDTs as an example, typical detection efficiencies for photons are at the level of 1%, and those for neutrons one order of magnitude smaller. Despite these low sensitivities, the low-energy neutral particle background will dominate the counting rates in most areas of the spectrometer. The simulated charged and neutral counting rates in the three stations of precision chambers are shown in Fig.2.2.2 (right) for the nominal LHC luminosity L $= 10^{34}\text{cm}^{-2}\text{s}^{-1}$. Combined with occupancy considerations, these rates drive the choice of precision chamber granularities. Since the background estimates are affected by significant uncertainties, a safety factor of five has been systematically applied to all computed rates in the detector design.

2.2.3 Layout of the Muon Spectrometer

According to the design the Muon Spectrometer [25] should provide a standalone measurement of the muon transverse momentum with a relative accuracy from 3% up to 10% in a momentum range from few GeV to 1 TeV and in a wide pseudorapidity range ($|\eta| < 2.7$). The layout of detectors in the spectrometer is the result of an optimization process taking different requirements into account:

- efficient use of the bending power of the magnet;
- very high resolution in the measurement of the muons p_t;
- almost full azimuthal coverage;
- projective tower geometry for chamber alignment;
- practical chamber dimensions for production, transport and installation.

To respect these requirements the Muon Spectrometer is composed by an assembly of different technologies both for tracking and for triggering muons. It is composed by a the barrel region ($|\eta| < 1.05$), a transition region ($1.05 < |\eta| < 1.4$), and two endcap regions ($|\eta| > 1.4$). As shown in Fig. 2.10, four different chamber technologies are employed: Monitored Drift Tube chambers (MDTs) and Cathode Strip Chambers (CSCs) for the precision measurement; Resistive Plate Chambers (RPCs) and Thin Gap Chambers (TGCs) for triggering. The total number of electronics channels is about 400 k for the precision chambers (MDT: 300 k, CSC: 100 k) and 900 k for the trigger system.

The barrel of the muon spectrometer, Fig.2.11, is constituted by three cylindrical layers of tracking detectors (MDTs). The three stations are located at radii of 4.5 m, 7 m, and 10 m. The trigger function in the barrel is provided by three stations of RPCs. They are located on both side of the middle MDT station and either directly above or directly below the outer station. The barrel covers the pseudorapidity range $|\eta|<1.05$. In the azimuthal direction, the chamber layout follows the eightfold symmetry of the toroid. For reasons of installation, accessibility, and size, the chambers are separated into 'large' and 'small' types. The large sectors cover the region between the magnet coils while the small ones are inserted into the coils. The maximum chamber length is 5.7 m. The active areas of neighboring small and large chambers overlap by at least 200 mm; they can thus be aligned with respect to each other using particle tracks. In the z direction, the chambers are segmented into physical units not larger than 2.6 m. The chamber widths in each of the three stations are determined by the requirement that they form projective towers with alignment rays passing close to the corners of the chambers. The following notation for the names of the barrel stations is used: BI for the barrel inner stations, BM for the barrel middle and BO for the outer stations.

The endcaps are constituted by three wheel shaped planes of vertical stations. The notation is the following: EI, EM, EO. MDT are used as precision chambers in the middle and outer stations, while CSC are used in the inner one. In the endcap the trigger is provided by three stations of TGC located near the middle MDT chambers.

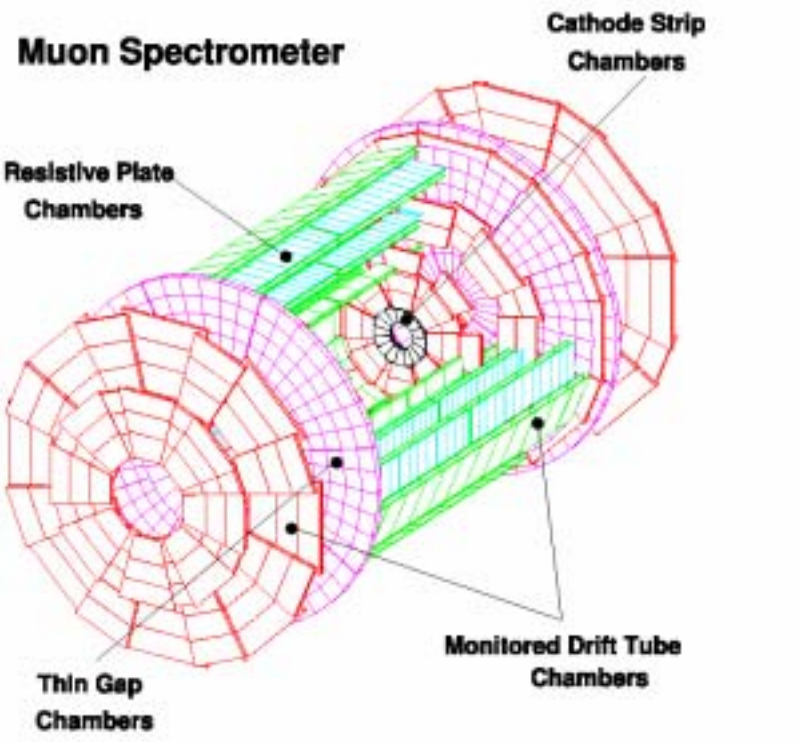

Figure 2.10: Muon Spectrometer layout.

They are of trapezoidal shape, with a maximum length of 6.3 m. Since the magnetic field changes sign along muon trajectories with $1.3 < |\eta| < 1.4$, additional horizontal chambers will be installed between the last two ribs connecting the barrel coils. They allow to measure separately the deflection of the muons in the endcap and barrel fields. The endcap chambers cover the pseudorapidity range $|\eta| > 1.4$. In the radial direction, the chambers are segmented into units of up to 3 m width, depending on their position and on the alignment scheme.

The measurement of the muon momentum is obtained by measuring the muon trajectory, curved by the magnetic field of the toroid magnet (par. 2.1.1), in three points by using precision tracking chambers both in the barrel and in the endcaps, as it is shown in Fig.2.12 where a section of the muon spectrometer parallel to the proton beams is schematized.

The Monitored Drift Tube chambers

The Monitored Drift Tube chambers will be described in detail in the next chapter.

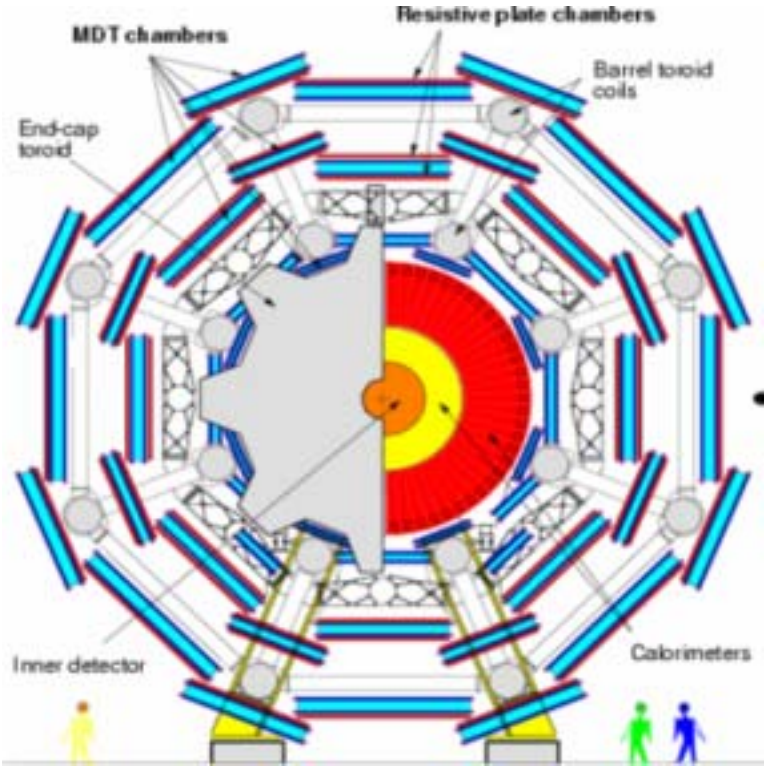

Figure 2.11: Section of the Muon Spectrometer in the plane r-ϕ.

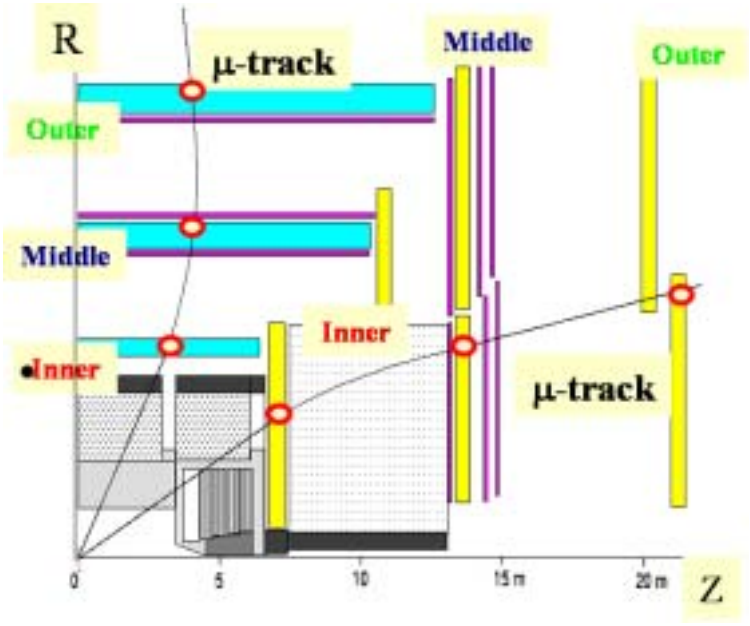

Figure 2.12: Section of the Muon Spectrometer in the plane r-z.

The Cathode Strip Chambers

The CSC are multi-wire proportional chambers with cathode strip readout and a wire spacing of 2.5 mm. The gas mixture is $Ar/CO_2/CF_4$ with the ratio of 30%/50%/20%. The maximum drift time is 30 ns. The precision measurement is obtained by measuring the charge induced on the segmented cathode by the avalanche formed on the anode wire. The measurement of the transverse coordinate is obtained from orthogonal strips, orientated parallel to the anode wire, which form the second cathode of the chamber. The cathode readout pitch is 5.08 mm. Good spatial resolution, better than 60 μm, is achieved by segmentation of the readout cathode and by charge interpolation between neighboring strips.

The Resistive Plate Chambers

The RPC is a gaseous detector that provides a typical space resolution of 1 cm and a time resolution of 1 ns. The active element of the RPC unit is a narrow gas gap formed by two parallel resistive bakelite plates, separated by insulating spacers. The primary ionization electrons are multiplied in avalanche mode produces pulses of typically 0.5 pC. The signals are readout via capacitive coupling by metal strips of two types on both sides of the detector. The η-strips are parallel to the MDT wires and provide the bending view of the trigger detector. The ϕ-strips are orthogonal to the MDT wires and provide the measurement of the second coordinate which is also required for the offline pattern recognition.

The Thin Gap Chambers

The TGC are similar in design to multi-wire proportional chambers, with the difference that the anode wire pitch is larger than the cathode-anode distance. Signals from the anode wires, arranged parallel to the MDT wires, provide the trigger information together with readout strips arranged orthogonal to the wires. These readout strips are also used to measure the second coordinate. TGC are constructed in doublets and triplets of chambers. The inner station consists of one doublet and is only used to measure the second coordinate. The seven chamber layers in the middle station are arranged in one triplet and two doublets which provide the trigger signal and the second coordinate measurement. To form a trigger signal, several anode wires are grouped and fed to a common readout channel. The number of wires per group varies between 4 and 20, depending on the required granularity as a function of pseudorapidity.

The alignment system

The optimum performance of the spectrometer can only be reached if the relative positions of the chambers along the track of a muon is known with a precision which is better than the intrinsic chamber resolution. The relative positions of the chambers in space has to be known with a precision of about 30μm. Of course given the large dimension of the

spectrometer is not possible to assembly the almost 1200 tracking chambers at the required precision level. For this reason chamber relative displacement will be continuously monitored by means of optical alignment system[26]. Different schemes of the alignment system are used for the barrel and endcaps regions.

In the barrel, the chambers are positioned in such a way to form projective towers In Fig.2.13 the arrangement of the light rays for the alignment of the barrel towers is shown. In order to reduce the number of projective rays, alignment towers have to be made out of two consecutive physical chamber towers. Thus an axial alignment system provides merging of adjacent chambers and a global positioning in space of all chambers within a sector. The scheme of the axial alignment system is also shown in Fig.2.13. Optical monitoring is foreseen only for the large sectors, while the small sectors will be aligned with particle tracks, exploiting the overlap with chambers in the large sectors.

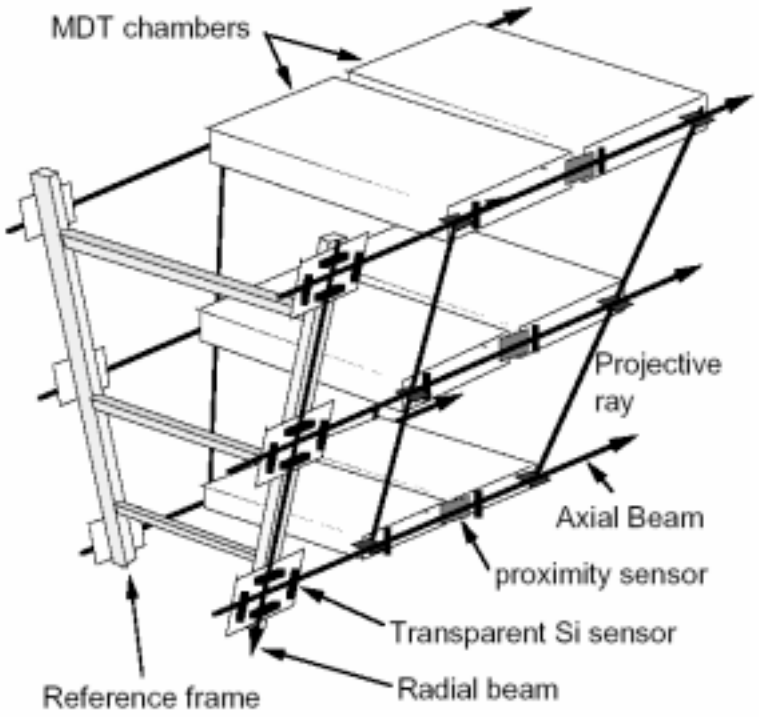

Figure 2.13: Scheme of the barrel muon spectrometer alignment system.

In the endcaps, the alignment scheme is based on a small number of pseudo-projective light rays connecting the chamber layers, and the reconstruction of all relative chamber positions. Moreover an in-plane alignment system, with four light rays for a large MDT chamber and one light ray for a small chamber, aims at monitoring MDT wire displacements with an accuracy of 10μm or better.

2.2.4 Muon Spectrometer performance

In Fig.2.14 the relative resolution of the Muon Spectrometer standalone muon momentum measurement is shown as a function of the muon momentum. The various contributes

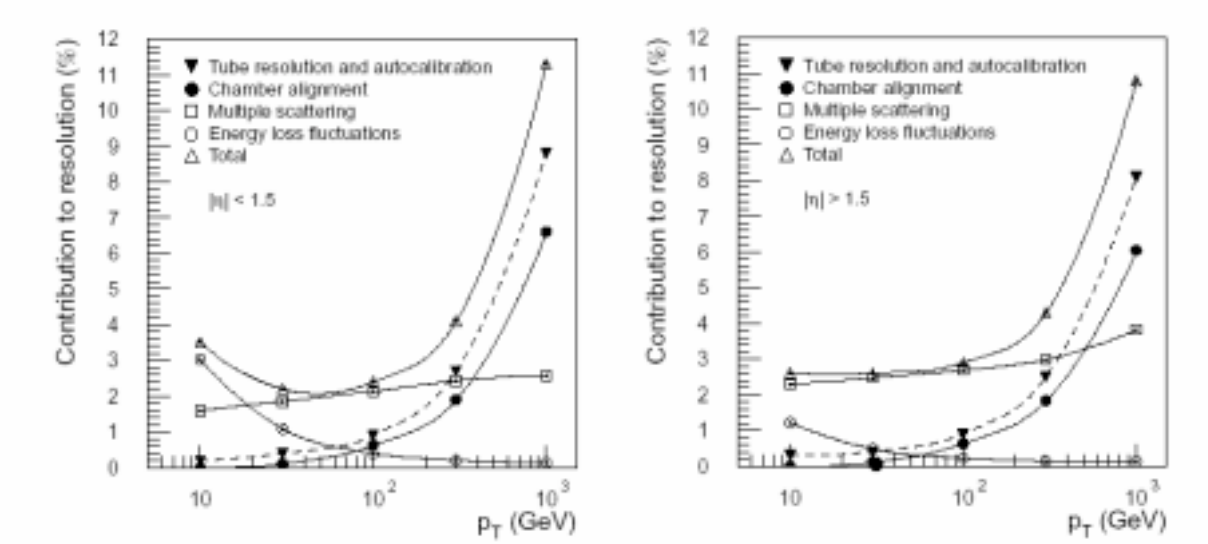

Figure 2.14: Relative muon momentum resolution for the Muon Spectrometer standalone: barrel (left) and endcaps (right).

to the total resolution are also shown: for $p_t < 20$ GeV the main contribute is due by statistical fluctuation of the energy loss in the material crossed by the muons upstream the spectrometer. In this p_t range the resolution is of 3-4%, a better resolution of 1-2% is obtained with the inner detector; for muons with 20 GeV $< p_t < 300$ GeV the resolution is dominated by the multiple scattering; for $p_t > 300$ GeV the multiple scattering becomes negligible and the chamber intrinsic resolution becomes dominant.

2.3 The trigger system

At high luminosity the interaction rate at LHC will be $\simeq$40 MHz, this requires the trigger system to work in very hard conditions. The average data volume for each bunch collision will be of about 2 MByte, so the overall data volume from the detector (10^7 readout channels) would require a data bandwidth of about 4×10^4 GByte/s. The data storage can record 10-100 MByte/s, so that the trigger system has to reduce the data volume by a factor 10^6 analyzing on line all the events and taking decision in about 1 s. Moreover, since the interesting processes have a very low rate, the trigger must be able to identify them with high efficiency. The trigger and DAQ are organized in three sequential levels, Level-1, Level-2 and Event Filter, this allows reduction of the event rate through several steps of increasing complexity and processing time. In Fig. 2.3 the trigger and DAQ architecture is shown.

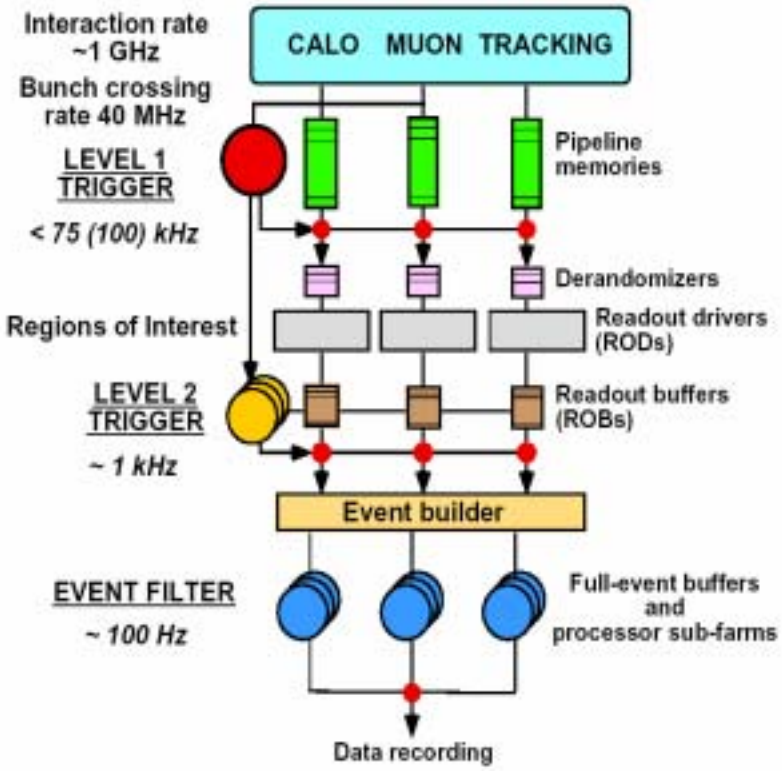

Figure 2.15: Block diagram of the trigger DAQ system.

The Level-1 trigger[27] works at the LHC bunch crossing rate of 40 MHz and has to take decisions in 20 μs. It is directly connected to the detector front-end electronics of calorimeter and muons detectors. Data coming from the inner tracker are not used because of the complexity of the events. It reduces the output rate from 40 MHz to 75 kHz, upgradeable to 100 kHz. Data of accepted events are stored in pipeline memories, connected to the read-out drivers (RODs) and made available to the high level trigger through read-out buffers (ROBs). Several ROBs are grouped in ROS (Read Out System) elements. The Level-1 trigger identifies also the bunch crossing associated to the triggered event.
The Level-2 and Event Filter triggers are based on software algorithms which make use of the full granularity of the detector[28]. The Level-2 trigger analyzes only data coming from the RoIs (Region of Interest) selected by the Level-1 trigger. The analysis, performed with fast algorithms, is made in two steps: first, for each RoI the object features are extracted for a more accurate confirmation of the object, and then combined to take the global LVL2 decision. The LVL2 trigger reduces the event rate by a factor of about 100 with a latency time in the range 1-10 ms. The accepted data from LVL2 are collected by the EB (Event Builder) and passed to the EF. The EF uses all detector data and takes the final decision on the event in a few seconds. LVL2 and EF combined will give a reduction factor of about 10^3. A simple trigger menu is employed by the LVL1 trigger which requires the presence

of at least one interesting object with the transverse energy above threshold to accept the event. On the contrary the High Level trigger (LVL2 and EF) use detailed trigger menus based on classification schemes of events which summarize the physics signatures associated to interesting processes.

2.3.1 The Muon Trigger

The LVL1 muon trigger identifies muons pointing to the interaction region with a p_t above a few GeV threshold. The selection is done using the data coming from fast and highly segmented detectors with an intrinsic time resolution less than the time gap between two bunch crossings. The muon spectrometer is able to trigger on the muon tracks by using different technologies for the barrel (RPC) and for the endcap regions (TGC).

In the barrel, the LVL1 trigger is done by three RPC stations each composed by two layers. Each layer is equipped with two planes of readout strip: the ϕ-strips are parallel to the magnetic field while the η-strips are parallel to the beam direction. The muon identification is obtained via fast coincidence between the hit in different RPC layers, which are compatible with a trajectory of a prompt muon. The central RPC is used as reference plane(*pivot*). Each hit found in the pivot plane is extrapolated along a straight line through the interaction point to the innermost and the outermost RPC stations, see Fig. 2.16. This defines a coincidence window in the η direction, the size of the coincidence window defines the p_t threshold of the trigger. A low-p_t muon is defined as a muon not reaching the outer layer of the muon spectrometer since it is curved by the magnetic field. In this case the trigger is formed by the coincidence window of the inner RPC. A high-p_t muon instead reaches the outermost station. The coincidence is valid when more than two RPC layers have hit strips in the trigger window. This allows to reduce the fake trigger due to cavern background. To achieve further reduction against fake triggers, the muon trigger works in the two plane, r-ϕ and r-z, indipendently and then combines the results. In this way the trigger detectors are used also to measure the muon position in the r-ϕ plane.

The LVL2 and EF triggers provide a reduction factor of 10^3 by rejecting low-p_t muons, muons produced by decay in flight of charged pions or kaons and fake muon tracks composed by hits from the cavern background. They take decisions in 10 ms and 1 s respectively. The probability that a fake LVL1 muon (from background) is reconstructed as a muon by the LVL2 trigger is 10^{-2}. EF has to recover additional muons present in the event that were not selected by LVL1 and LVL2 triggers.

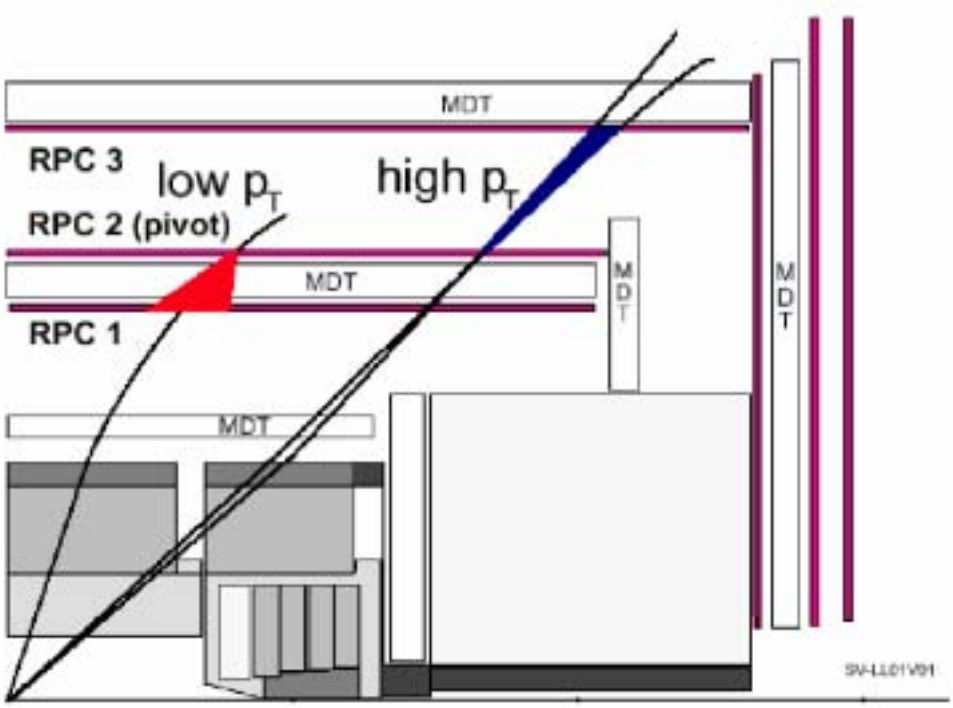

Figure 2.16: Schematic view of the Level-1 muon trigger.

Chapter 3

The Monitored Drift Tube Chambers of Atlas

The Muon Spectrometer of Atlas allows the measurement of the transverse momentum of muons in a wide range of muon momenta with a high precision. This is due to the three tracking chamber layers that provide a precision coordinate measurement in the bending direction of the air-core toroidal magnet.

The tracking stations are made by Monitored Drift Tube chambers (MDT's) and Cathode Strip Chambers (CSC's). MDT chambers are in all the three stations of the barrel and in the middle and the outer stations of the endcaps. CSC chambers are in the first station of the endcaps to provide a finer granularity, which is required to cope with the demanding rate and background conditions in this region. The whole Muon Spectrometer is formed by 1194 MDT chambers for a total of 370000 readout channels and a total gas volume of 800 m^3. They have all the same operating principles differing only for dimensions and shape depending on the position in the Muon Spectrometer. The MDT chambers provide an excellent determination of the trajectory of muons within the pseudorapidity range $|\eta| < 2.7$. In this chapter a description of the MDT's operating principles and performances will be reported.

3.1 The MDT chambers

A Monitored Drift Tube chamber[29] consists of layers of pressurized drift tubes glued together and organized in two multilayers on either side of a rigid support structure. The dimensions of each chamber and the number of tubes per layer depend on the chamber position in the spectrometer. As an illustrative example, chambers of the barrel region will be described.

The barrel chambers are constituted by two multilayers, each of which is done by three layers of tubes, Fig. 3.1. Only the chambers of the inner station have four layers per multilayer in order to increase the tracking efficiency at the entrance of the spectrometer. In order to reach the required precision level (each point has to be measured with a precision of 50 μm) the MDT chambers have to satisfy very stringent mechanical constraints. The

relative position of the two multilayers has to be known with 40 μm precision. Each multilayer has to maintain a certain flexibility in order to let the tubes follow the natural wire sagitta. A deviation of the wire from the tube center greater than 100 μm should create deformation of the electric field around the wire and consequently systematic effects on the tracking. Moreover in order to guarantee a good spatial resolution, the position of the wires with respect to a chamber reference frame has to be know with at tolerance of 20 μm.

The positions of the MDT chambers one respect to the other has to be known with a precision of 30 μm. This is clearly very hard over the large global dimensions of the spectrometer. Therefore, chamber positions are constantly monitored by means of optical alignment systems and displacements up to 1 cm are corrected in the offline analysis. Moreover an in-plane alignment system controls chamber deformations. More details on the alignment system have been reported in chapter 2.

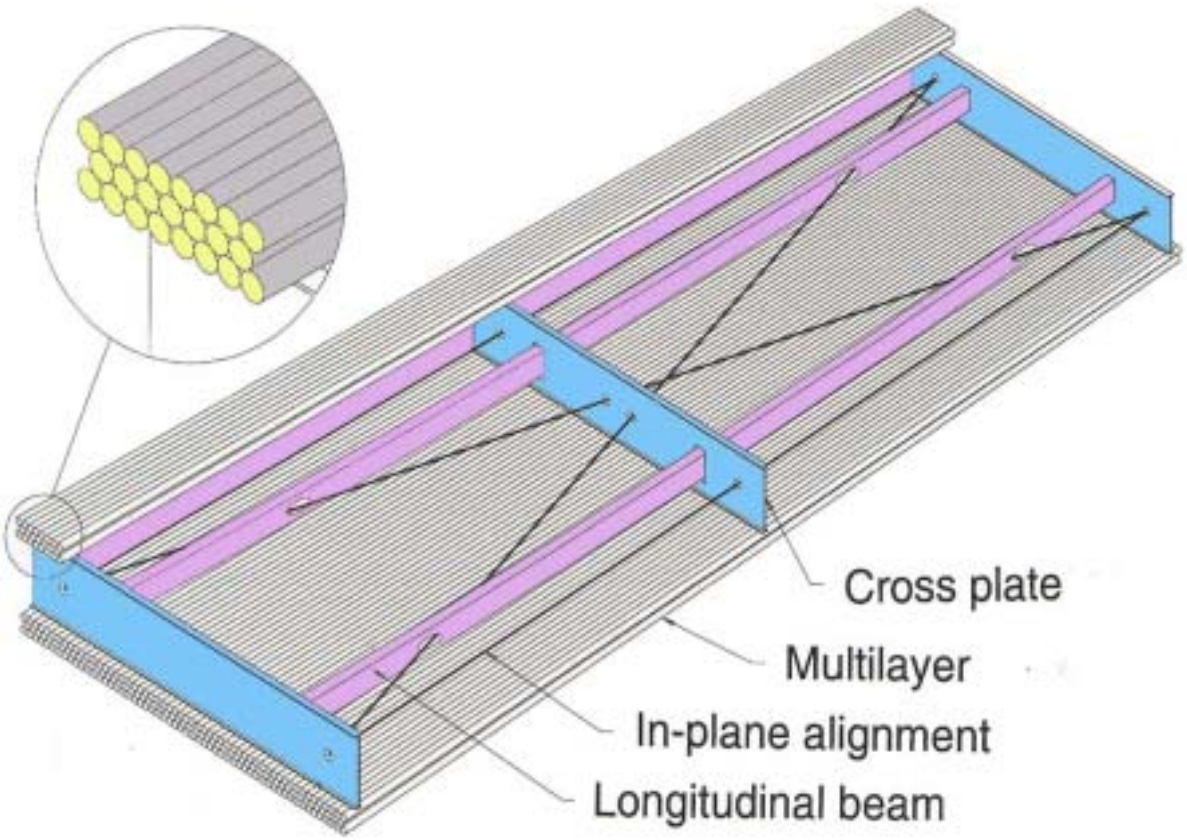

Figure 3.1: Schematic drawing of an MDT barrel chamber.

3.2 Single tube operating principle

The basic detection element of an MDT chamber is a cylindrical aluminum drift tube. Each tube has a diameter of 30 mm and a wall thickness of 400 μm, while the length varies from chamber to chamber depending on the chamber position in the spectrometer. The tube holds a 50 μm diameter W-Re (97/3) wire at its center as anode. The tube is closed at both ends with specially developed 'end-plugs', which hold the wire in the center of the tube with a precision of 10 μm and give electrical access to the tube and to the wire. The tube is filled with a non-flammable gas at high pressure to reduce diffusion and ionisation position fluctuations, the gas mixture is Ar/Co_2 (93/7). A positive high voltage of 3080 V is applied to the wire. The standard conditions chosen for the Atlas drift tubes are summarized in Tab. 3.1.

Diameter	3 cm
Tube thickness	400μm
Wire thickness	50μm
Gas mixture	Ar/CO_2 93/7
Pressure	3 bar abs
HV	3080 V
Gas gain	2×10^4
Maximum drift time	700 ns
Discriminator threshold	20^{th} electron

Table 3.1: Characteristics of the single drift tube

When a charged particle crosses a tube, the gas is ionized and the ionization electrons begin to drift to the wire following the electric field lines. An electric signal is generated on the wire. In Fig. 3.2 the drift path of the ionization electrons is shown, the path is bent due to the presence of the magnetic field in the spectrometer. The primary electrons generated by a charged particle traversing a drift tube move in the electric field towards the wire, and they experience frequent collisions with the molecules of the operating gas. The drift process can be described by the rt-relation, which for each time t the fastest electrons need to reach the anode and produce a signal, gives the distance r from the wire.

Close to the wire the electric field is so high, $\simeq 10^5$ V/cm, that an avalanche is generated. Since the electron drift velocity in the wire proximity (< 100 μm) is of $\simeq 50$ μm/ns, the process of charge multiplication takes about 1 ns. The gas gain, that is the ratio between the total number of electrons reaching the wire and the number of primary electrons, is of 2×10^4.

The signal generated is then propagated along the wire and collected from the MDT's readout electronics. The measured time is the sum of different contributions:

$$t_{meas} = t_{drift} + t_{prop} + t_0, \tag{3.1}$$

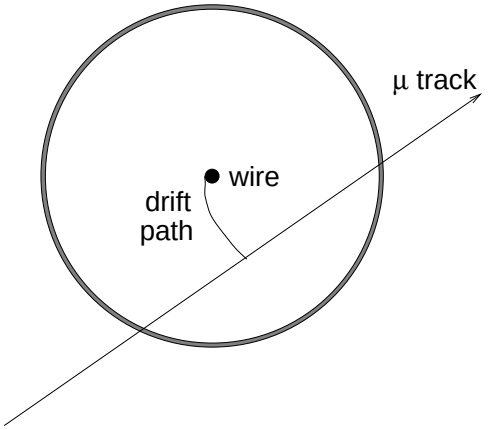

Figure 3.2: Transverse view of a drift tube.

where t_{drift} is the time that the electrons take to reach the wire, t_{prop} is the time to propagate the signal along the wire and t_0 is a constant of the tube that takes into account the delay of the signal cables and front-end electronics. The t_{prop} and t_0 are independent on the drift properties of the tube. A typical time distribution is shown in Fig. 3.3. The t_0 is defined as the start of the physical time window and corresponds to the

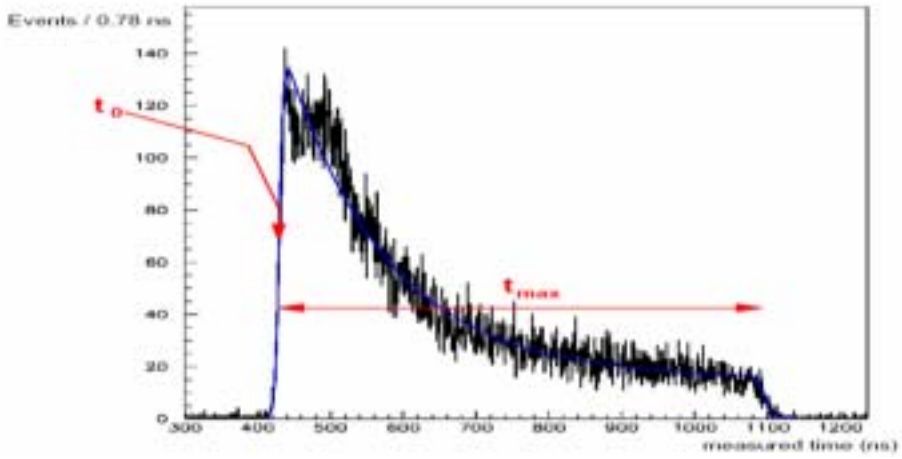

Figure 3.3: A typical TDC spectrum.

drift time of particles that cross the wire. In the same way, t_{end} is the end of the physical time window. The quantity $t_{max} = t_{end}$ - t_0 corresponds to the drift time associated to particles passing close to the tube wall and depends on the gas drift properties. The t_0

and t_{max} values can be determinated by fitting the time spectrum with the function:

$$\frac{dn}{dt} = P_1 + \frac{P_2(1 + P_3 e^{-\frac{t+P_5}{P_4}})}{(1 + e^{\frac{-t+P_5}{P_7}})(1 + e^{\frac{t-P_6}{P_8}})}. \tag{3.2}$$

Here P_1 is the noise level, P_5 is the t_0, P_6 is the t_{max} and the other parameters are related to the shape of the signal distribution. It has been shown that the accuracy in determinating t_0 is about 0.5 ns for a sample of 20 K tracks per tube.

The time t_{prop} is measured by the trigger chambers that measure the "second" coordinate[1] of the hit in the tube and has to be subtracted to the t_{drift}. The t_{max} is, in standard conditions of 3 abs bar pressure and 27 °C temperature, of about 700 ns. The t_{max} is dependent on the gas temperature, in fact a slope of about -2.7 ns/K has been observed. For this reason each chamber is equipped with temperature sensors to be able to correct the measured drift time offline.

From the TDC spectrum, Fig. 3.3, the non linearity of the drift velocity is evident. In fact the MDT mixture, Ar/CO_2 (93/7), belongs to the group of so-called nonlinear drift gases for which the electron drift velocity v_{drif} is proportional to the reduced electric field strength E/ρ, where ρ is the gas density. It immediately follows that v_{drif} is not constant over the cross section of the tube.

Once the drift time of the ionization electrons has been measured, it has to be converted in the distance between the muon track and the wire in order to determine the muon trajectory. In this way one can individuate in a single chamber six (eight for the inner station chambers) coordinates of the track in the plane perpendicular to the tube direction, that is the plane r-z on which the muons are bent. An accurate knowledge of the rt-relation, and thus of the drift velocity, is a prerequisite for using drift tubes to precisely reconstruct particle tracks. The rt-relation of a tube is highly dependent on its operating conditions (HV, threshold), as well as on the gas composition, pressure, temperature and on the magnetic field. An example of rt-relation for a tube in standard conditions is reported in Fig. 3.4.

3.2.1 Tube autocalibration

The chamber calibration procedure makes use of the information from the measured drift times and of the precise knowledge of the wire positions. It is thus an autocalibration procedure. The standalone C++ software tool Calib [32] is used to perform the autocalibration. The method works under some important assumptions. First it is expected that tubes that operate in the same conditions have the same rt-relation. The toroidal magnetic field of the spectrometer is not uniform, but it is possible to divide a chamber into regions where this variation is negligible. Moreover the tracks used for calibration have to be straight lines. In the experiment, the event samples used for autocalibration will be provided by the LVL-1 muon trigger that selects particles with transverse momentum

[1] The coordinate measured by the precision chambers is on the plane r-η, that is the plane on which the tracks are curved by the magnet, while the second coordinate is the one along the tube.

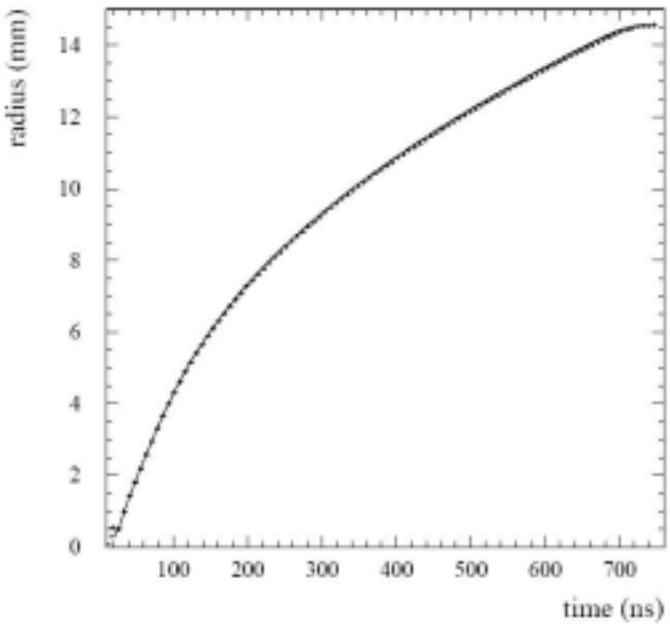

Figure 3.4: Typical rt-relation.

greater than 6 GeV. Within a multilayer the curvature of such tracks is negligible. The autocalibration procedure is therefore applied separately to each multilayer.

The method consists in three steps:

- first the t_0 of each tube is computed and subtracted from the measured drift time to equalize the times in the different tubes. Then, assuming an appropriate function for the drift velocity (an initial $R(t)$ relation), the best straight line, tangent to the circles representing the hits is computed;
- the difference between the measured drift radius ($r_{meas} = R(t_{meas})$) and the one obtained by the track fit is computed and used to correct the $R(t)$ relation;
- using the corrected $R(t)$ relation new drift circles are identified and the track fit is performed again.

This is an iterative procedure that is stopped when the average residuals, that means the difference between the measured drift distance and the radius of the drift circle found by the track fit, $\Delta R(t_{meas}) = R(t_{fit}) - R(t_{meas})$, are below the required accuracy of 10-20 μm. Usually 10 iterations are sufficient to reach the required accuracy. It is important to stress that this procedure converges to a unique and bias-free solution only if the angular spread of the tracks is at least 100 mrad. This due to the fact that a beam of parallel tracks correlates in a unique way the measured drift time in the tubes of a multilayer and the autocalibration is not sufficiently constrained. In Fig.3.5 the residuals as a function of

the measured drift distance at the different level of the iteration procedure are shown. At the last iteration step the residuals are contained within ± 10 μm from zero everywhere.

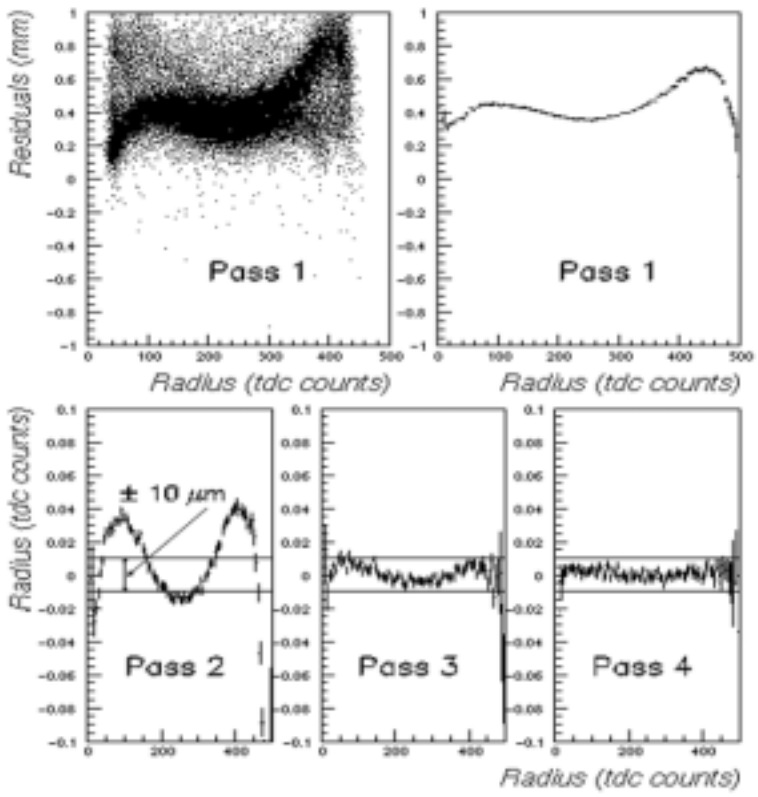

Figure 3.5: Residuals as a function of the drift distance at the various steps of the iterative procedure of chamber autocalibration.

3.2.2 The intrinsic spatial resolution

The intrinsic spatial resolution of a single MDT tube depends on the resolution in measuring the drift time of the ionizing electrons. The time resolution has different contributions:

- discrete nature of the primary ionization. The ionization electrons are grouped in clusters. The distance between clusters and the number of electron per cluster can fluctuate;
- Landau fluctuations of the ionization charge of each cluster and fluctuation of the gas gain;
- diffusion during the drift;
- electric noise;

The fluctuations of the distance between clusters and of the number of electrons contained in each cluster produce fluctuations on the signal rise time (*time slewing*). This means that the time in which the signal goes over the discriminator threshold can vary, since the arrival time of the first electron (start of the signal) and the time to let the last electron reach the wire change. This effect is relevant for tracks that cross the tube near the wire becoming negligible for radii greater than 1 mm. For drift distances greater than 1.2 cm the dominant contribution to the intrinsic tube resolution is due to the diffusion of the ionization electrons. The effect of the diffusion is that the individual electrons follow a zigzag path toward the anode wire rather than a straight line. The actual path length travelled by an electron is not fixed but follows a distribution with a finite width; this prodeces a resolution on the drift time. The high pressure of the MDT gas mixture minimizes this effect. In Fig.3.6 the contributions to the time and spatial resolution are shown as a function of the drift distance. The single tube spatial resolution ranges from 200 μm very near to the wire and 50 μm near the tube wall. The spatial resolution mediated on the while tube radius is of 80 μm.

3.3 MDT Electronics

Each MDT tube terminates on one side with a 380Ω impedence, while on the other side is put the front end and the readout electronics. The MDT electronics processes the information of the ionization electrons arriving on the wire. A preamplifier converts the induced current signal into a voltage pulse which is sent to a discriminator. A time do digital converter, synchronized to the bunch crossing clock, measures the time of the leading and trailing edge of the discriminator output and stores it in a buffer. In case of a LVL1 trigger the data corresponding to the event of interest are driven to the Atlas data acquisition system via the readout driver. The electronic scheme is shown in Fig. 3.3. Each multilayer is entirely enclosed in a faraday cage shield at both ends. The faraday cage is grounded to the end of each tube at the endplug. The exterior of the faraday cage has a ground attachment point provided to allow the signal ground to be tied to a clean external Atlas ground point. Each complete MDT chamber is electrically isolated from the support structure, and all services (gas, electrical, etc) are also electrically isolated or floating at the source.

On the readout side of a chamber the tubes are grouped in blocks of 24 tubes, each of them is connected to a mezzanine card. A mezzanine card is a printed circuit board composed by three 8-channels ASD (Amplifier, Shaper and Discriminator) and a simple 24-channels ADC. The outputs of three ASD chips drive a 24-channels Time to Digital Converter (TDC). Data of each TDC are read out individually via a 40 Mbit/sec serial link to a single CSM (Chamber Service Module) which multiplexes the serial links (on a chamber the serial links could be up to 18) into a single optical fiber for transmission to the Atlas DAQ. A daisy-chain JTAG bus permits the downloading of the parameters of ASDs and TDCs.

The time measurament is performed by a 24-channel TDC by dividing the 40 MHz

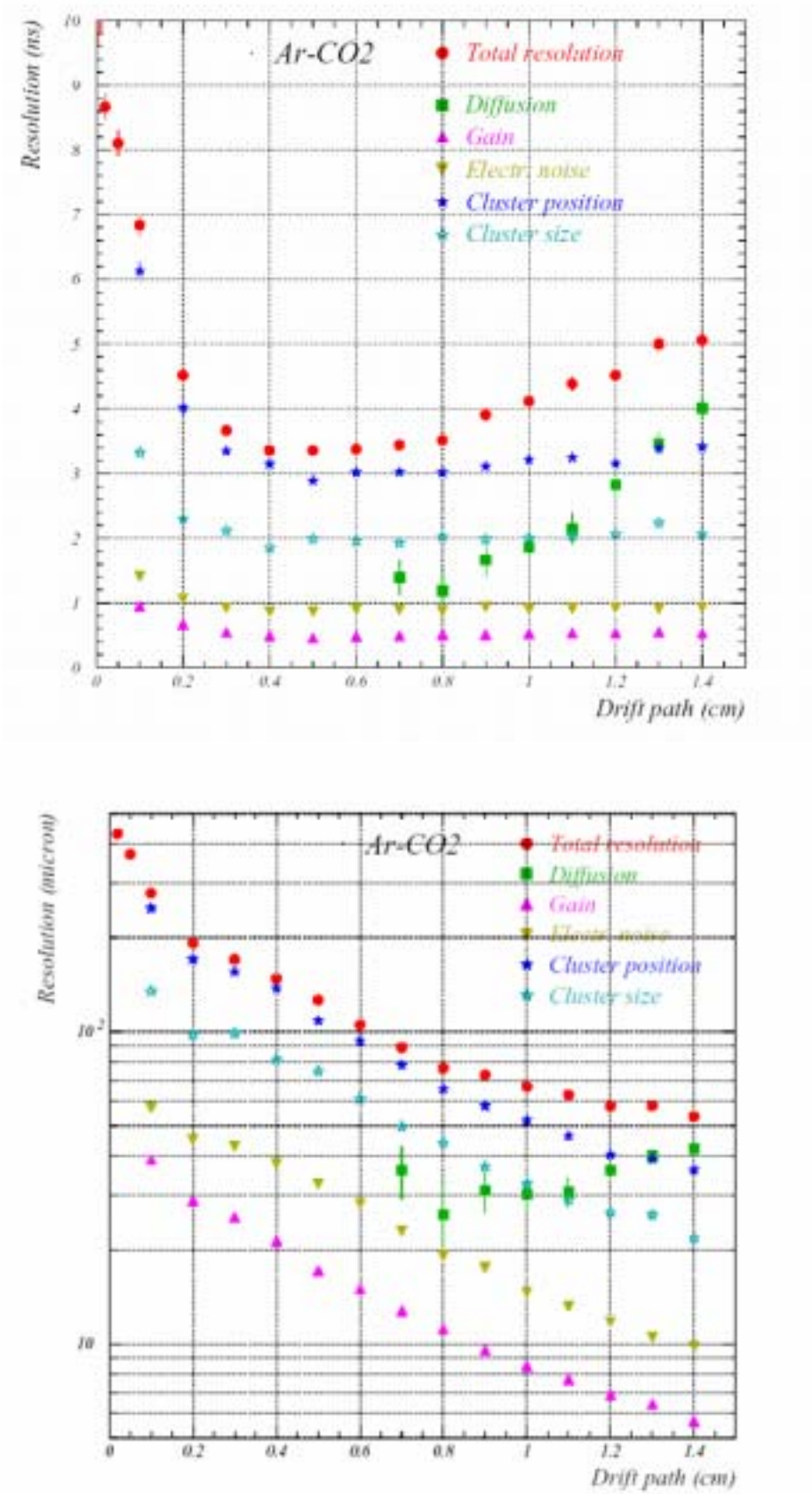

Figure 3.6: Contribution to the time (top) and spatial (bottom) single tube resolution.

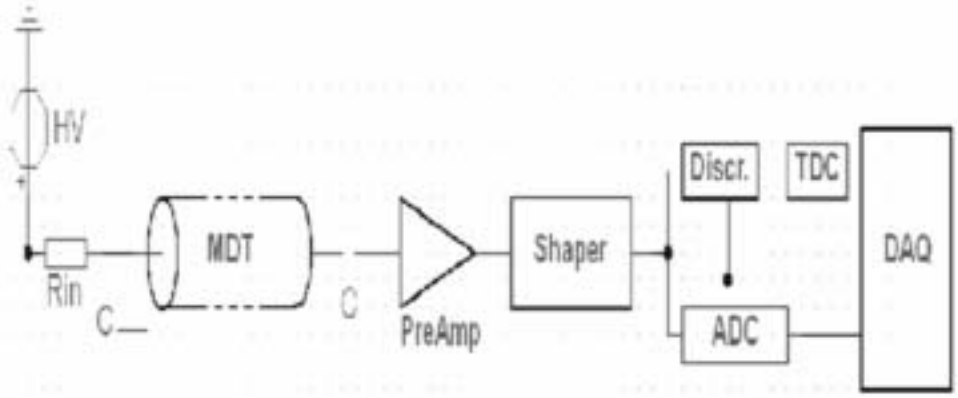

LHC clock into 32 intervals providing 0.78 ns time bins. For what concerns the discriminator threshold, once the gas gain is fixed to 2×10^4, the minimal practical threshold is five times the noise level, which in the MDT is dominated by termination resistor series noise, that corresponds to 17 electrons.

Chapter 4

The H8 Test Beam

In the year 2004 Atlas has been involved in a very intensive test of the different sub-detector technologies in a combined test beam at the H8 beam line at the CERN SPS[33]. A complete slice of the Atlas barrel and of the muon end-cap has been tested with beams of different particles (pions, electrons, muons and photons) at different energies (ranging from 1 GeV up to 350 GeV). This provided a unique opportunity to evaluate the individual sub-detector performances and also to exploit the full power of the Atlas detector for particle identification and measurements in a realistic combined data taking.

In this chapter a more detailed description of the H8 setup of the muon system will be reported in order to introduce and explain the results obtained analysing the data collected with chambers of the barrel muon system. The object of this chapter is the evaluation measurement of the precision reachable by the MDT chambers in the measurement of the muon momentum and sagitta. Referring to Fig. 4.1, the sagitta of a track is defined as the distance between the reconstructed segment in the middle station of the muon spectrometer and the track connecting the segments reconstructed in the outer and inner stations. The sagitta is related to the track curvature in a magnetic field and thus to the track momentum.

The Atlas Muon Spectrometer has been designed to provide a good stand-alone momentum measurement, the transverse momentum should be measured with a resolution of $\sigma(p_T)/p_T = 10\%$ at $p_T = 1$ TeV . A muon with $p_T = 1$ TeV has a sagitta of $\simeq 500\mu$m in the average magnetic field of 0.5T of the Atlas spectrometer, thus to reach a momentum resolution of 10% the sagitta has to be measured with an accuracy of 50μm. The MDT chambers have been designed to contribute to the sagitta resolution with an intrinsic term of the order of 50μm. Since the measured sagitta resolution depends not only on the intrinsic resolution of the tracking chambers but also on multiple scattering, an energy scan is needed to disentangle the two contributes. With the 2004 H8 data it was also possible to measure the beam momentum, since a B magnet was present in the H8 setup. The H8 setup gives the unique possibility to measure this quantity in a realistic layout before the installation of the Atlas experiment will be completed. Many tests can be performed in a combined test beam: mechanical detector installation tests, integration between different technologies, test of the detector control system, integration between different subsystem

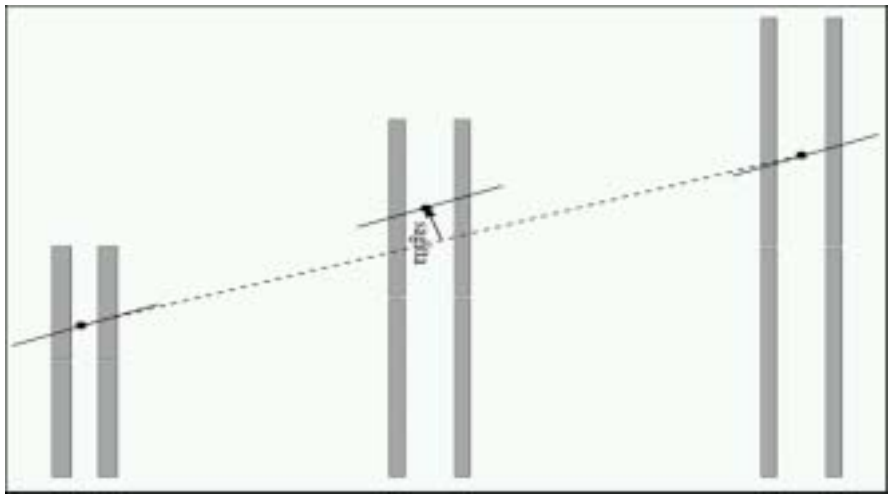

Figure 4.1: Sagitta definition

tasks (trigger and tracking) and different software tools (data acquisition, databases, high level trigger software, on-line and off-line monitoring and reconstruction), study of the alignment and calibration of the chambers.

4.1 The H8 Muon setup

The H8 muon beam is obtained by the proton beam provided by the SPS CERN machine. Muon energy ranges from 20 to 350 GeV . The upstream section of H8 test is reserved to Calorimeter and Inner Detector tests. It is separated from the Muon Spectrometer area by the beam dump, an iron block thick 3.2 m. A schematic top view of the 2004 muon setup is shown in Fig. 4.2.

The H8 Muon setup [34, 35] is constituted by two sections: a barrel stand and an end-cap stand. Since the data presented here have been collected with the barrel chambers, in the following only the barrel setup is described. The barrel part is composed of two barrel towers, each of them is constituted by an inner, a middle and an outer chamber installed on rails. It emulates a barrel sector of the Spectrometer consisting of six MDT chambers and six RPC chambers. The MDT tubes are located in vertical position (perpendicular to the plane of the Fig. 4.2) and the tube layers form with the beam an angle of about 15°(0.26 rad). The MDT chambers are: two inner large (BIL), two middle large (BML) and two outer large (BOL) chambers.

The chambers are fully instrumented with front-end electronics (FEE), read-out with the Muon Readout Driver (MROD) and fully equipped with the optical alignment system. Each middle MDT chamber has one RPC chamber upstream and one RPC chamber downstream. The outer MDT's have one RPC chamber downstream.

The beam does not illuminates in the same way the two towers of barrel chambers.

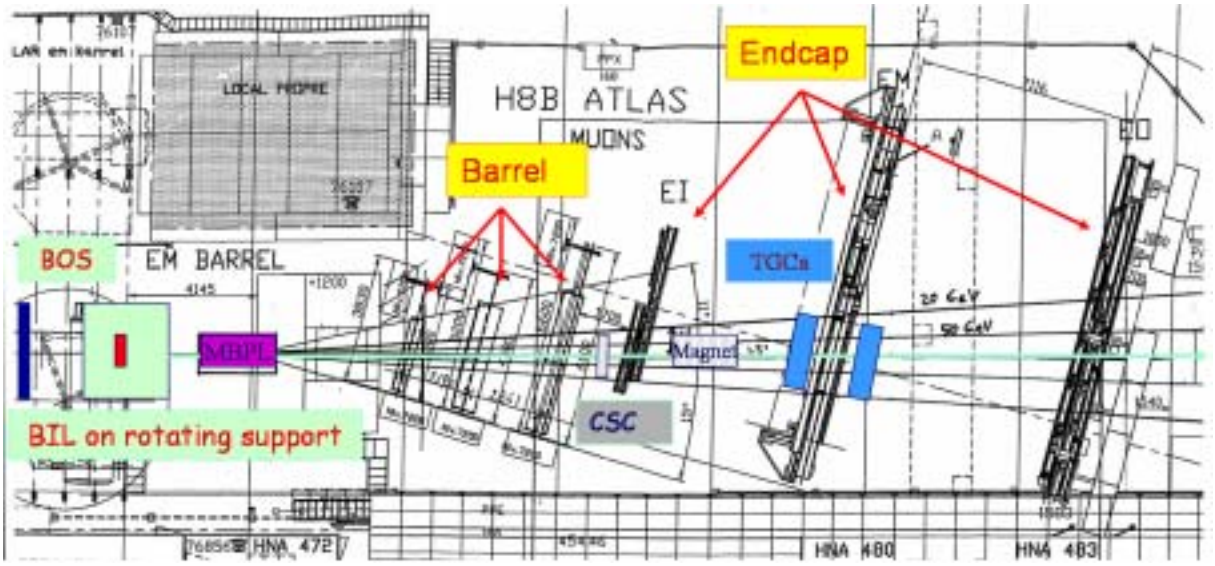

Figure 4.2: Top view of the H8 muon setup

The tower at the top in Fig. 4.2 is the most illuminated. Only events collected with this tower have been considered in the analysis.

Two additional barrel stations are present on the test, before the barrel sector: one outer station upstream of the muon wall and one inner barrel on a rotating support (hereafter called "rotating BIL"). The rotating BIL can rotate around its axis from 0° to 10° respect to the direction normal to the beam in the horizontal plane (the plane of Fig. 4.2). One beam magnet is installed between the rotating BIL and the barrel towers, in order to bend the muon track in the horizontal plane (magnet field of this dipole points along the MDT wires, the vertical coordinate). The magnet current can be controlled remotely from the control room and varies from 0 A up to ±600 A. It is able to provide a maximum field integral of about 4 Tm.

For the results that will be reported in the next section, the RPCs are used to perform measurement of the second-coordinate (the vertical coordinate, along the MDT wires) and not to trigger on the beam muons. Two external systems of trigger were available in H8. A small area trigger is given by the coincidence of the signals of two scintillators (10×10 cm^2) centered on the beam line. It is installed upstream the magnet. A large area trigger (60×100 cm^2) is given by the coincidence of the signals of two planes of six scintillating slabs (each of 10×100 cm^2). In order to suppress the beam core, the possibility to use the 10×10 as a veto for the hodoscope is foreseen.

4.2 General analysis description

A very schematic top view of the two barrel towers is shown in Fig. 4.3, the reference system used in the analysis is also plotted. The magnetic field and the wires of the MDTs

are along y-axis (vertical) and the tracks are reconstructed in the plane z-x (horizontal plane).

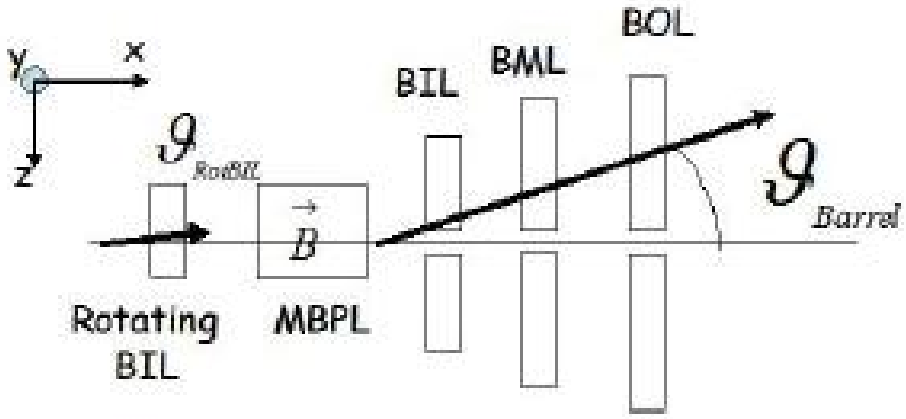

Figure 4.3: Schematization of the muon system at H8. The coordinate frame is shown.

The rotating BIL chamber measures the angle that the muon track forms with the x-axis before the magnet, θ_{RotBIL}[1]. The chambers after the magnet MBPL measure the same angle after the magnetic field, θ_{Barrel}. The barrel track is computed as the track that crosses the two super-points associated to the segments separately in the BIL and BOL chambers, as it is shown in Fig. 4.1 where also the sagitta is shown. The super-point is the crossing point of the track segments at the center of the chamber. The momentum of the track can be determined by measuring the deviation of the track due to the magnet, that means computing the difference $\Delta\theta_B = \theta_{Barrel} - \theta_{RotBIL}$. The muon momentum is given by the formula:

$$p(GeV) = \frac{0.3BL(Tm)}{\Delta\theta_B(rad)} \tag{4.1}$$

where BL is the bending power of the magnetic field and it is known once the magnetic current has been fixed.

The formula is correct if the rotating BIL and the chambers of the barrel sector are perfectly aligned in the z-x plane, that means respect to rotations around y-axis. This is not the case, in fact the rotating BIL position respect to the barrel chambers is unknown. The effect of a possible misalignment can be taken into account by measuring the track deviation in the case of null magnetic field $\Delta\theta_0$. The final formula is then:

[1]The rotating BIL rotates only during calibration runs. It is fixed during the measurement of θ_{RotBIL}.

$$p(GeV) = \frac{0.3BL(Tm)}{(\Delta\theta_B - \Delta\theta_0)(rad)} \tag{4.2}$$

With this method the muon momentum has been measured using the Muon Spectrometer chambers for the first time. Even if the method is quite different from the one will be used in Atlas, it is an important exercise to test the tracking performance of the Spectrometer. Also the measurement of the sagitta cannot be performed in the same way as in the Atlas environment, since in H8 setup the tracks crossing the chambers are straight lines. The track segments are reconstructed separately in each barrel station (BIL, BML and BOL) and the super-points are computed. Then a straight track crossing the two super-points in the two extreme chambers (the BIL and the BOL) is computed (it is the same track used to perform muon momentum measurement). The sagitta is the distance between the BML super-point and this track (Fig.4.1).

In H8 setup the barrel chambers are installed on three rails. In the final Atlas environment, the wires of the different chambers are required to be aligned with a precision of about $2mrad$. A vertical length of 10cm, that is the track spread allowed by the small area trigger used, takes a maximal shift of 200μm of the chamber wire centers respect to the nominal position in the z-x plane. Then the sagitta and consequently the sagitta resolution depend on the track vertical coordinate. A selection of tracks with the same y-coordinate is necessary to avoid this dependence. The y-coordinate is measured by the ϕ-strips of the RPCs, that are the strips perpendicular to the MDT wires. Only tracks that cross the system at the same y-coordinate have been used to compute the sagitta. In Fig. 4.4 the beam profile for the RPC ϕ-strips of the BML station is shown. In particular the figure on the left reports the beam profile on the first RPC chamber (before the MDT) on both the two ϕ-strip layers. The figure on the right shows the beam profile on the RPC chamber put after the MDT. Due to the geometry setup, the second chamber is more illuminated than the first. Only muons with at least one hit in the most illuminated ϕ-strip of the RPC upstream and downstream the MDT chamber are selected. It has been checked that equivalent results are obtained if a cut is applied on the RPC ϕ-clusters instead of on the ϕ-strips.

4.2.1 Data sets

The data on which this analysis has been performed were collected with the barrel chambers and the rotating BIL operated in the same conditions. The gas mixture of MDT chambers was : Ar:CO_2 (93%:7%) at 3 bar absolute pressure. The high voltage was 3080 V . The trigger system was the 10×10 hodoscope. The analysis has been repeated for three data sets at different discriminator thresholds: -36, -40, -44 mV . For each threshold a scan of beam momentum has been performed between 100 and 250 GeV , by varying the settings of the H8 beam, with these nominal values indicating the beam momentum at the H8 entry, before the crossing of the Calorimeters and of the beam dump. As it will shown with the measured momentum distributions, it is not possible to obtain a perfectly monochromatic beam. For each group of data at the same beam momentum and at the same threshold, three runs taken in sequence has been selected to perform the analysis:

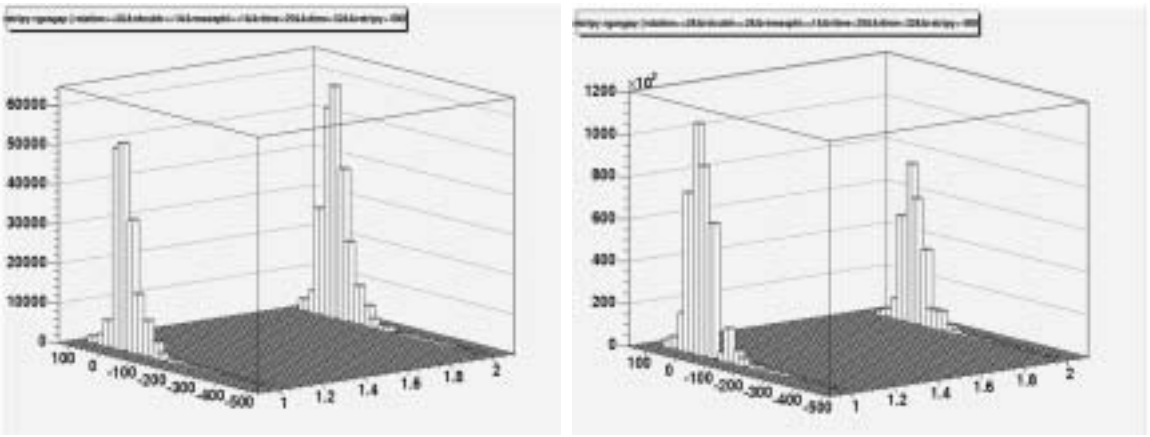

Figure 4.4: Strip profile of the beam on the two gaps of the RPC upstream the BML (left) and of the RPC downstream the BML.

- a run during which the rotating BIL chamber was rotating. This sample is used to calibrate the chambers.

- a run during which the rotating BIL was fixed and the magnet was switched off. This sample has been used to measure the misalignment of the rotating BIL respect to the barrel sector in the z-x plane.

- a run during which the rotating BIL was fixed and the magnet was switched on. This sample has been used to perform both sagitta and momentum measurement.

The analysis has been performed using the package MuonTestBeam of the ATHENA release 10.0.0.

4.2.2 Data Calibration

The MDT calibration procedure (computation of the t_0 and rt-relation for each tube) has been explained in chapter 3. Here are reported some specific considerations to calibrate the chambers in the H8 setup.

t_0 determination

For each tube, the parameters of the raising of the drift time spectrum has been derived from a fit to a Fermi-Dirac function. In order to reduce the statistical uncertainties, all the data used in the analysis are summed up to compute the fit. In order to reduce the electronic noise, a cut has been applied : only hits with ADC counts larger than a given threshold have been selected.

rt-relation determination

For each set of runs with the same nominal momentum the rt-relations of the two multilayer of the rotating BIL have been measured. In Fig.4.5 is reported the rt-relation obtained. The single tube space resolution used for this work ranges from 200μm, near the wire, to 50μm, near the tube wall.

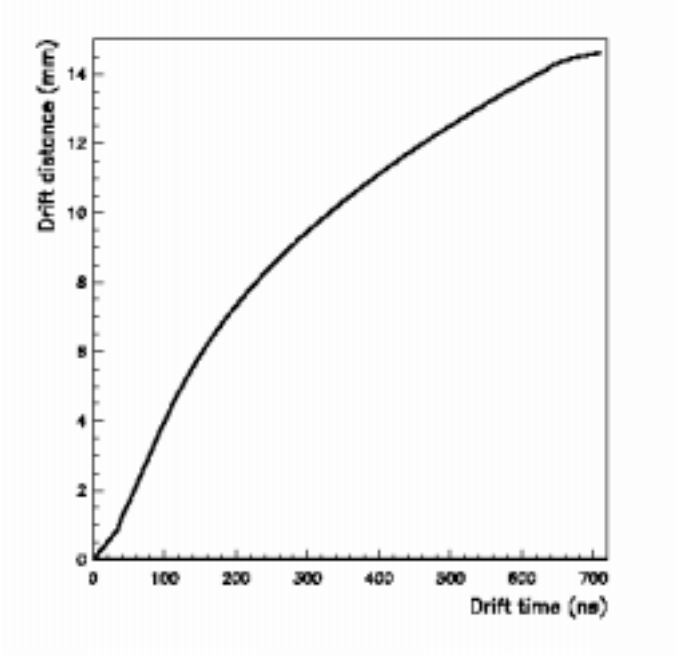

Figure 4.5: The $r-t$ relation measured for the first multilayer of the rotating BIL.

A check on the computed t_0s and on rt-relations has been performed investigating the residual distribution separately for each layer as a function of the distance from the wire. The sign disentangles between tracks passed to the right and to the left of the wire. The residual distributions are shown in Fig.4.6. The data refer to the run with a nominal momentum of 150 GeV and a discriminating threshold of -36 mV.

The large values at small drift distances are due to the difficulty to compute the rt-relation near the wire, where the electric field is very large and the drift velocity varies rapidly. Since the autocalibration procedure (see chapter 3) fails for radii smaller than 1 mm a linear $r-t$ relation is used in this drift range in this work. For radii larger than 1 mm and smaller than 5 mm, the residual distribution of the overall layers is within 20μm. A quite large spread is observed on the individual layers, but it is always smaller than 30μm - 40μm. The spread decreases approaching the tube wall, where the single tube intrinsic resolution improves. Similar distributions are observed for the second multilayer. The chamber of the two towers are kept in fix position respect to beam axis. Since they are operated at the same conditions of the rotating BIL, the rt-relation of the first multilayer of this chamber has been used also for all the other chambers.

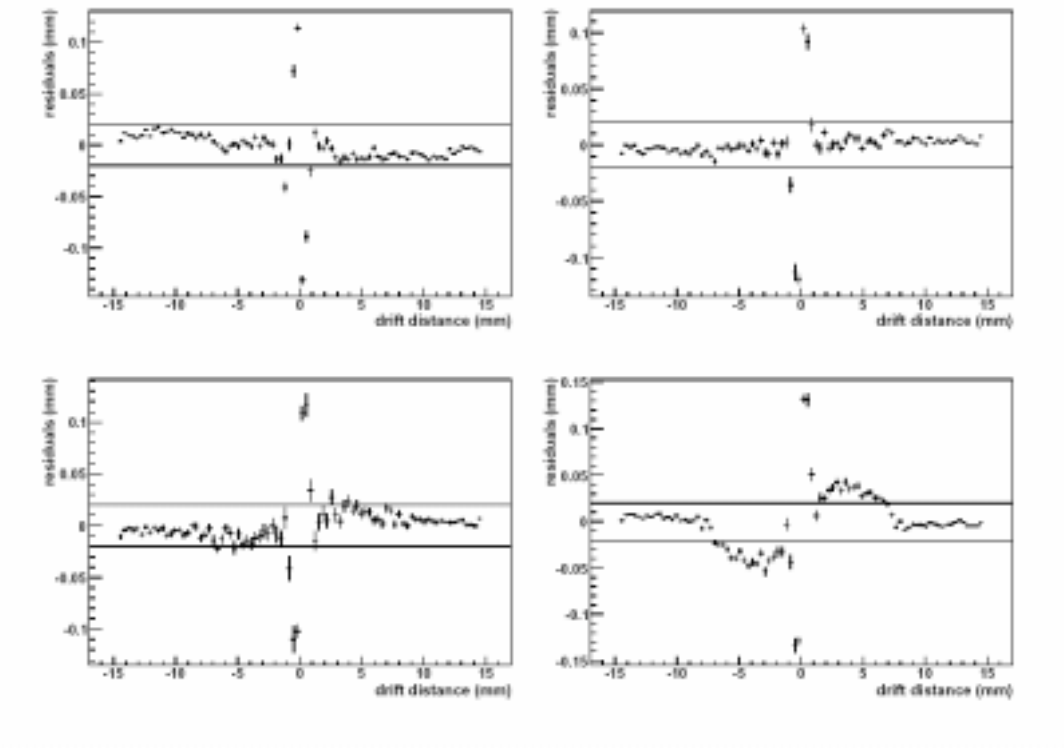

Figure 4.6: Residual distributions as a function of signed drift distance: for the rotating BIL (top-left), for the BIL (top-right), for the BML (bottom-left) and for the BOL (bottom-right).

4.3 Muon momentum measurement

The momentum measurement has been performed for each beam momentum with three sets of runs at different values of the MDT main threshold. First the difference $\Delta\theta_0$ has been measured to take into account a possible misalignment of the chambers due to ratation around the y-axis. Then the difference $\Delta\theta_B$ has been computed. In Fig. 4.7 the distributions of the two angular differences and the distribution of the momentum obtained (eq. 4.2) are shown for the runs with 120 GeV nominal beam momentum and -40 mV threshold. In table 4.1 the mean values and the standard deviation of the momentum distributions obtained for the various runs performing a gaussian fit are reported.

The beam momentum is measured by the barrel chambers with a resolution of few %s. Looking at the table 4.1 it is evident that there is a discrepancy between the nominal and the measured momentum. This is mainly due to the energy loss (about 13 GeV) by the beam in the material upstream the muon area (Calorimeters and beam dump). In Fig.4.8 the momentum distributions for the runs at different nominal beam momentum and threshold -44 mV are shown.

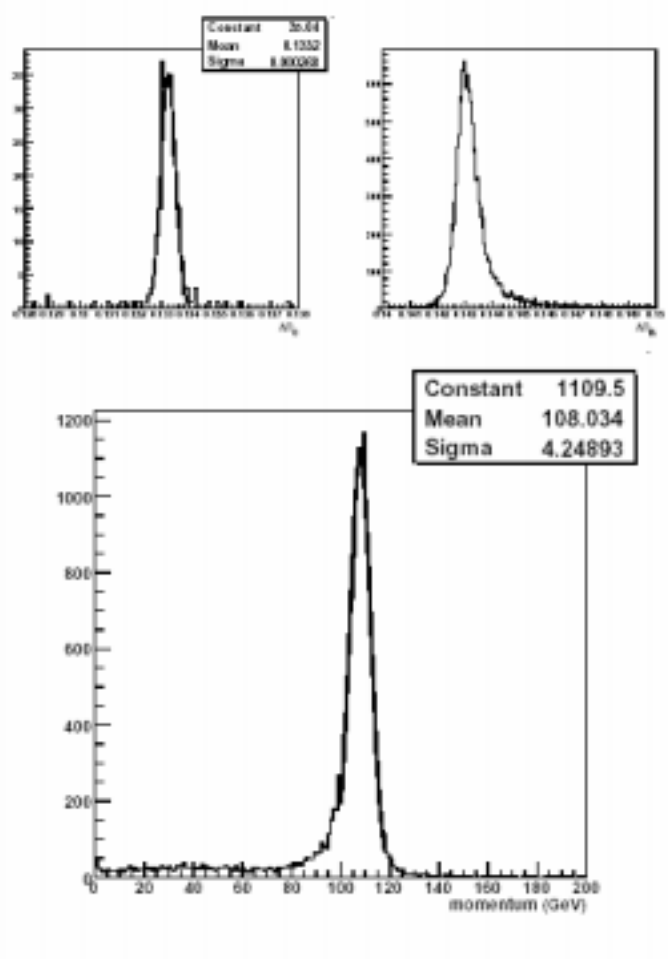

Figure 4.7: Top left: $\Delta\theta_0$ distribution; Top righ: $\Delta\theta_B$ distribution; Bottom: beam momentum distribution. The figures refer to runs at nominal momentum of 120 GeV.

$P_{nominal}$	P_{mean} (GeV)	σ_p (GeV)	$P_{mean}(GeV)$	$\sigma_p(GeV)$	$P_{mean}(GeV)$	$\sigma_p(GeV)$
100	88.7	4.5	88.8	4.2		
120			108.0	4.2	108.1	4.1
150	136.9	6.1	135.0	5.8	136.1	6.0
180	163.5	7.5			163.4	7.4
220	203.2	11.6	206.7	11.3	202.0	11.5
250	229.4	14.9	230.1	15.1		

Table 4.1: Measured momentum mean value and standard deviation at different nominal momenta for three thresholds: -36 mV, -40 mV and -44 mV.

4.4 Sagitta resolution measurement

At it is evident, the beam was not fully monochromatic. For this reason to perform the measurement of the sagitta resolution a cut was applied on the track momentum

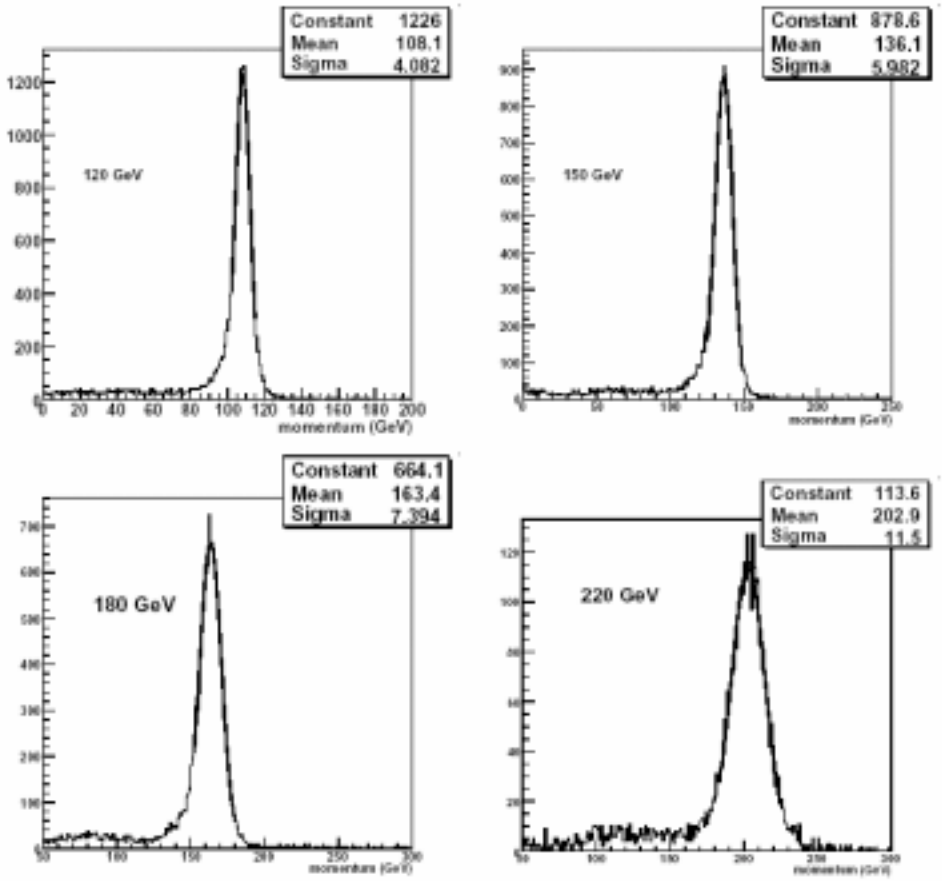

Figure 4.8: Beam momentum distributions for runs at different nominal momentum and -44 mV threshold.

distribution: only tracks with a momentum larger than $p_{mean} - 2\sigma_p$ have been selected. Another cut was applied in order to minimize the contribute to the sagitta resolution due to possible misalignment of the chambers due to rotation around the x-axis: only tracks crossing the RPCs in correspondence of the same ϕ-strips have been selected. The final sagitta distributions are shown in Fig.4.9 for the -44 mV threshold. The mean value of the sagitta should be zero since the muon measured by the two towers downstream the magnet is a straight track. This is not the case since misalignment of the chambers in the two towers are not taken into account. Anyway we are interested in the muon momentum resolution and not in the absolute momentum value. The standard deviations obtained with a gaussian fit on the sagitta distributions obtained with different nominal momentum and thresholds are reported in table 4.2.

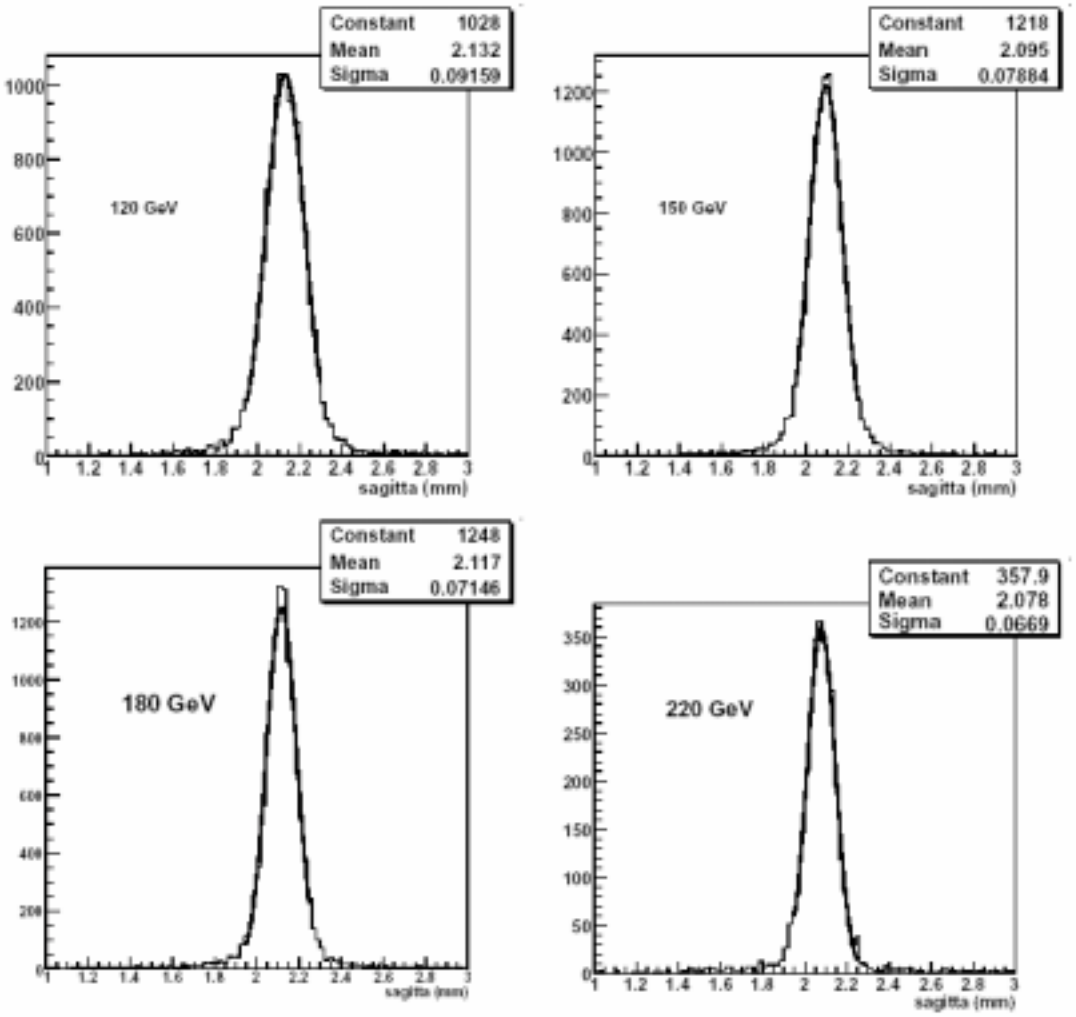

Figure 4.9: Sagitta distribution for runs at different nominal beam momentum and threshold -44 mV. This sagitta distributions are obtained after the two cuts described in this section.

$P_{nominal}$	σ_S (μm)	$\sigma_S(\mu$m)	$\sigma_S(\mu$m)
100	97.99 $\pm$2.49	101.8 $\pm$ 1.1	
120		90.56 $\pm$ 0.79	91.59 $\pm$1.00
150	74.90 $\pm$ 1.10	76.46 $\pm$ 0.62	78.84 $\pm$ 0.82
180	70.15 $\pm$ 1.40		71.46$\pm$0.71
220	62.99 $\pm$ 1.57	65.00 $\pm$ 2.00	66.90$\pm$1.20
250	59.61 $\pm$ 1.96	62.0 $\pm$ 1.40	

Table 4.2: Sagitta distribution width for the data set at different threshold.

4.5 Final results: sagitta resolution versus muon momentum

The curve of the measured sagitta resolution as a function of the muon momentum is reported in Fig. 4.10 for the three data sets with different values of the MDT discriminator threshold.

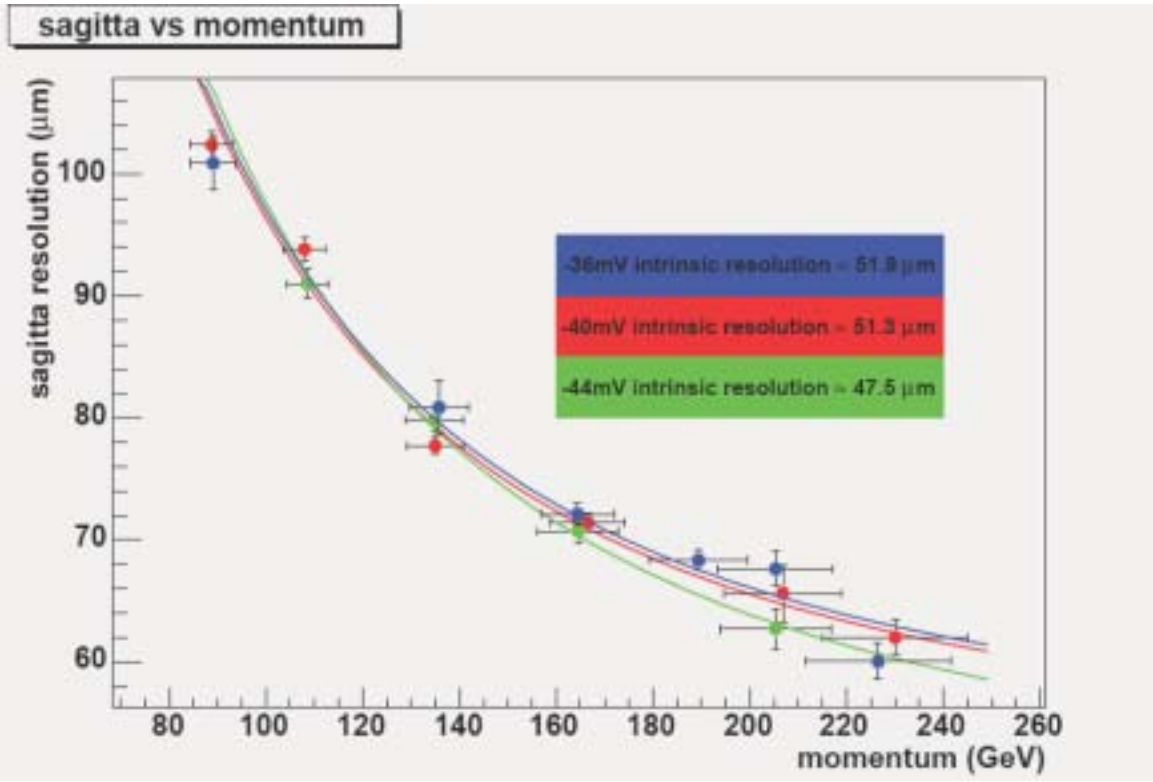

Figure 4.10: Sagitta resolution as a function of the muon momentum.

The measured sagitta resolution depends on two independent terms: the intrinsic resolution of the precision chamber that does not depend on the beam momentum, and

the multiple scattering that instead depends on the muon momentum. The three curves have been fitted with the function:

$$\sigma = \sqrt{P_1^2 + (P_2/p)^2} \tag{4.3}$$

where P_1 is the constant term related to the intrinsic resolution while P_2 is the term related to multiple scattering. In a way almost independent from the MDT main threshold we find that the contribution to the sagitta resolution due to the intrinsic resolution is of $\simeq 50\mu$m. The values found for the different thresholds are reported in table 4.3.

Threshold	Intrinsic sagitta resolution $\sigma_S(\mu\text{m})$
-36 mV	50.8 ± 2.9
-40 mV	51.8 ± 2.4
-44 mV	53.2 ± 3.3

Table 4.3: Intrinsic sagitta resolution term for the data sets at different threshold.

The P_2 term can be translated into the term $<x/X_0>$ that is the average distance crossed by the track in radiation length units. The schematization of Fig.4.11 has been used to perform the calculation. It has been supposed that the scattering happens exactly in the BML superpoint. The sagitta resolution term related to the multiple scattering is given by the formula:

$$\sigma_S(multiplescattering) = \frac{P_2}{p} \simeq \frac{(Z_2 - Z_1)(Z_3 - Z_2)}{(Z_3 - Z_1)}\sigma_{\theta_0} \tag{4.4}$$

where (Z_2 - Z_1),(Z_3 - Z_2) and (Z_3 - Z_1) are the known distances between the chambers, σ_{θ_0} is the r.m.s. of the multiple scattering angle and it is given by the formula [36]:

$$\sigma_{\theta_0}(rad) = \frac{13.6MeV}{p}\sqrt{x/X_0}\,[1 + 0.0038ln(x/X_0)] \simeq \frac{13.6MeV}{p}\sqrt{x/X_0} \tag{4.5}$$

From this formula is possible to obtain the relationship between P_2 and $< x/X_0 >$:

$$P_2 \simeq \frac{(Z_2 - Z_1)(Z_3 - Z_2)}{(Z_3 - Z_1)}13.6MeV\sqrt{< x/X_0 >} \tag{4.6}$$

The value of $< x/X_0 >$ obtained by the fit are reported in table 4.4. The $< x/X_0 >$ is about 30% and take into account about $9mm$ of alluminium of MDT tubes and for the material of the two RPC chambers.

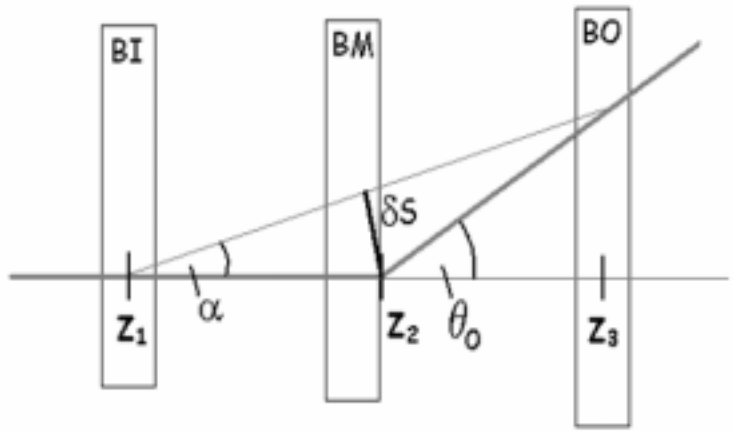

Figure 4.11: A top schematic view of the barrel H8 system. The method to compute the multiple scattering contribution to the sagitta resolution is also schematized.

Threshold	$< x/X_0 >$ (%)
-36 mV	26.9 ± 3.5
-40 mV	28.8 ± 2.4
-44 mV	29.9 ± 3.6

Table 4.4: Multiple scattering contribution to the sagitta resolution for the data sets at different threshold.

Chapter 5

MDT chambers certification and installation

Once an MDT chamber has been produced in its home institute, it is sent to CERN, where some last performance tests are performed before the installation in the Atlas cavern. About 400 MDT chambers of type BMx and BOx, that means chambers of the middle and outer stations of the spectrometer barrel, have to be tested with cosmic rays data before the installation in the cavern. The BB5 Cosmic Ray (CR) Test facility at CERN is used for this purpose[1].

In BB5 MDT and RPC chambers are prepared, pretested and then moved on the CR stand for the final step of the certification procedure. The final step consists in the analysis of the cosmic rays data collected. Once a chamber has been certified at the CR, it is moved to the Atlas cavern at point1.

After transportation from the CR stand of BB5, chambers undergo a new set of tests before being down-loaded in the Atlas pit and installed in final position in the spectrometer. These tests are performed in the SX1 surface area at point1 and are necessary to control that chambers have not been damaged during transportation.

If a chamber satisfies the BB5 and SX1 acceptance criteria, it is ready to be installed in Atlas.

The installation of the muon stations in the Atlas spectrometer has started in summer 2005. In autumn 2005 six BML chambers and six BOL chambers were installed in sector 13 and connected to temporary services. During the installation a parallel effort has started to take data with the chambers of sector 13. An intense work of commissioning, to test not only the functionality of the MDT chambers but the whole system, (trigger, detector control system, data acquisition and online/offline monitoring) has been performed.

In this chapter the main steps of the certification procedure of an MDT chamber will be described, from the cosmic ray stand in BB5 to the first data taking in the pit.

[1] Chambers of the inner station of the spectrometer are tested in a separate cosmic test stand at CERN.

5.1 The cosmic Ray Stand at BB5

The cosmic ray stand at BB5 [37] has been put on not to perform precision chamber studies but represents a fundamental step in the certification procedure that every chamber of the barrel middle and outer muon spectrometer stations has to pass before it could be considered good performing and installed in the Atlas cavern. Goal of the cosmic rays certification is to validate overall correct functioning of the stations including the read-out chain and front-end electronic.

In BB5 MDT chambers are prepared before the CR test. The preparation consists on HV cables connection check, plugging mezzanine cards and Central Service Module (CSM) on each chamber, control the on-chamber gas distribution and so on. Temperature sensors and magnetic field probes are also tested. Moreover all the chambers undergo a leak test and a noise test, even though they have been already performed in the home institute. After both the MDT chamber and its corresponding RPC planes have been prepared and have passed their respective tests in BB5, they are integrated into the final muon station and moved on the CR stand. Their functionalities are tested simultaneously but separately in the CR stand.

5.1.1 BB5 setup and trigger

The CR stand at BB5 can house up to 3 stations simultaneously. Each station is supported on a drawer which runs on rails in order to allow station installation and removal from the cosmic trigger system. In Fig. 5.1 the CR stand in the BB5 building is shown. The three stand floors are equipped with all the services (gas connections, HV and LV cables, optical fibers) in order to be able to take data on the three stations simultaneously.

Cosmic rays are triggered by two RPC chambers put under and over the CR stand. The lower trigger RPC is put 1 m under the floorboard and the upper is at a distance of about 6 m in order to select the most possible vertical cosmic rays. In order to cover the largest area as possible, two RPC formed by two type-B units have been chosen. They cover an area of 2×5 m^2 with a trigger acceptance large enough to cover completely the largest barrel chambers that have to be tested.

The two trigger RPC are made by 2 layers and 64 η-strips and 160 ϕ-strips for each layer. They are operated with the same gas mixture as the RPC of muon stations to be certified. Only the signals from strips perpendicular to the length of the plane (ϕ-strips) are used to generate the trigger. Strips are connected to a special receiver, each output of the receiver module is the logic OR of 8 strips and thus corresponds to an area of approximately 25×200 cm^2 of the RPC plane. Output signals of the receiver module are first passed to a discriminator for signal shaping, next the logic OR of all strips of an RPC layer is formed. Signals of the two layers of the upper RPC are delayed by 16 ns in order to compensate for the muon flight time between the two RPC planes. A coincidence of hits in 3 out of the 4 RPC layers is required to generate the final trigger signal. Typical trigger rates range from 150 to 200 Hz.

During all data taking the DAQ is operated in a strict single event mode, that means

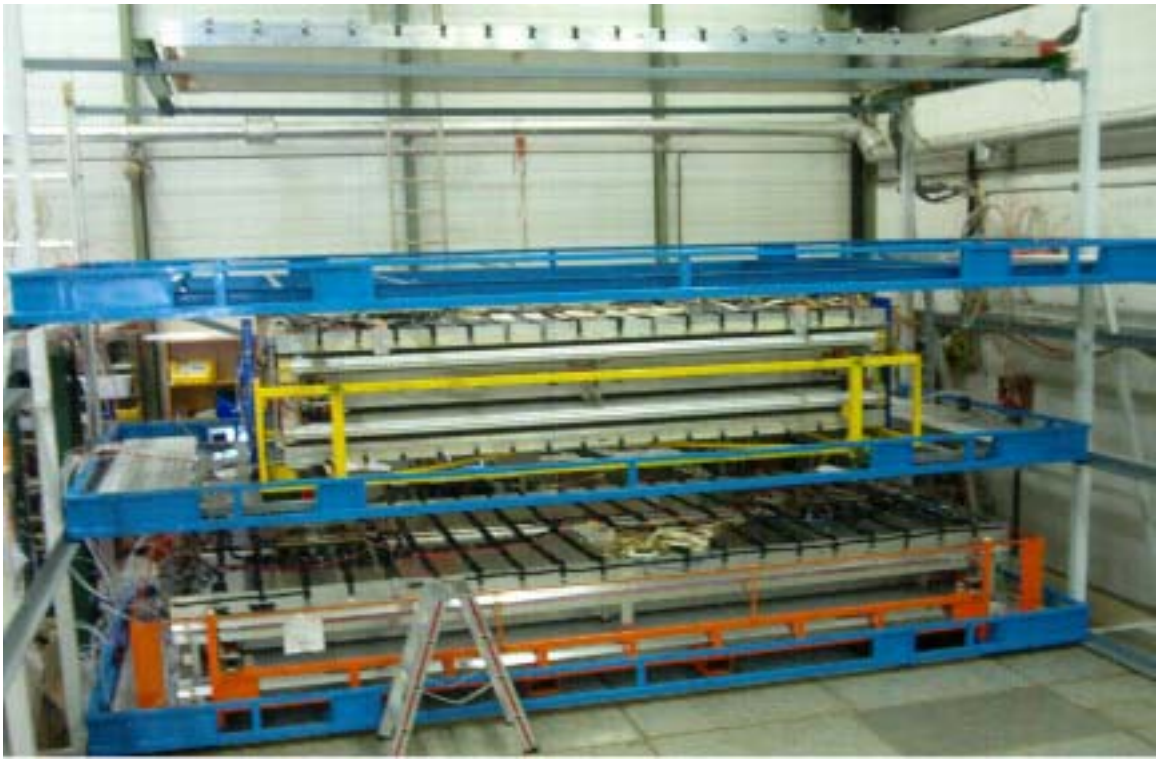

Figure 5.1: The Cosmic Ray stand in BB5: a BOL is put on the first floor, a BML on the second one, the third is empty.

that generation of triggers is physically stopped after each trigger signal until all data of the corresponding event has been read out and processed. For rates up to a few kHz, that amply cover the rates observed with cosmics, the single event mode does not pose any limitations to the performance of the system.

5.1.2 MDT Test Procedure

After a chamber has been put in place on the CR test stand all services needed for the test have to be connected on it. An MDT chamber has to be connected to:

- gas system: a gas supply system take the chamber to a constant absolute pressure of 3 bar by an electronic pressure regulator, with a minimum flow of 50 Nl/h. Gas mixing is done with the help of two mass flow controllers. They operate in blending mode, in which the absolute flow of CO_2 is adjusted automatically according to the current flow of the major component, Argon;

- HV system: the MDT operating high voltage (3080 V) is applied individually for each chamber multilayer by a CAEN SY1833P module. In addition, each MDT chamber is earthed during the tests by means of a separate cable connected to the metal part of the chamber for safety reasons;

- LV system: MDTs must be supplied with a single low voltage of 5 V; the power line has to be connected to the MDT mother board in order to aliment all the MDT readout electronic;

- read-out: the TTC fiber and the data acquisition fiber have to be connected to the CSM (Chamber Service Module). DCS information are read-out throught CanBus.

Once the chamber is connected some checks have to be performed before data taking. Gas pressure has to be measured after connecting a chamber to the CR test stand gas system. If a value below 2.85 abs bar is found, the chamber has to be flushed for several hours. The values of parameters that can influence drift properties (atmospheric temperature, pressure, gas mixture composition) and detector working parameters (ASD thresholds, applied voltages and currents) must be monitored. A detector control system (DCS) has been implemented in BB5 to monitor these parameters.

The MDT electronics has to be initialized and the ADS threshold set. A successful initialization is required for all mezzanine cards. Mezzanine serial numbers must be known for all cards and individual ASD offsets must be used for programming. After the electronics initialization, the current supplied to the chamber by the low voltage power supply has to be checked. A deviation of more than 0.2 A from the expected value[2] is followed by a more detailed control of individual mezzanine cards.

Finally the HV can be turned on. Each multilayer is required to draw less than 2 μA of current at 3080 V. High currents can be due to bad gas composition, too little CO_2 or to much water in the mixture. Chambers with initial currents above 2 μA per multilayer are flushed, with the high voltage switched off, for several hours. Another reason is humidity in the high voltage hedgehog boards and cables. In this case currents decrease rapidly as soon as high voltage is switched on.

For each chamber a long time run (one night) has to be taken in order to accumulate statistic enough to analyze the TDC and ADC spectra for each single tube. A statistic of about 10^5 events is necessary to perform fits on the single channel TDC and ADC spectra and determine the main spectra parameters.

5.1.3 Acceptance criteria

Some simple codes have been developed in BB5 in order to quickly analyze data, fill histograms and look at the relevant variables. An MDT chamber is required to satisfy the following criteria in order to be certified:

- Hit profile: hit profile is the number of hits per tube. It is checked for each tube layer separately in order to control the correct relation between electronics channels and the geometrical tube position that is obtained from a mapping file, which is read by the analysis program. Error in the cabling between mezzanine cards and CSM are easily visible in the hit profile. The hit profile is also useful to check and

[2]Expected value depends on the number of mezzanine cards of the chamber.

identify dead and noisy channels. In Fig.5.2 a typical hit profile as it has seen by a layer of a BML chamber is shown;

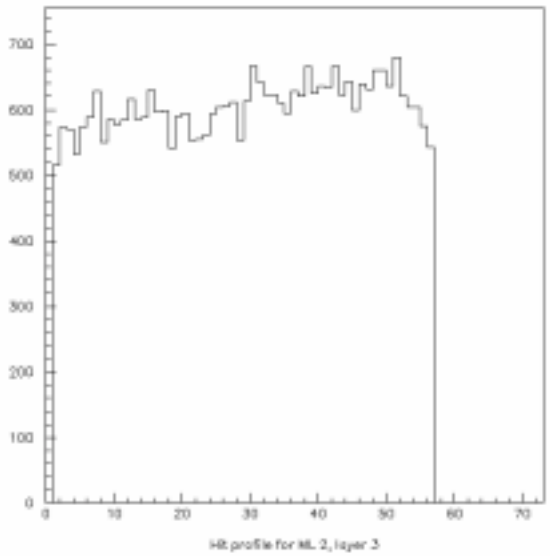

Figure 5.2: Hit profile: number of hit per tube for the layer 3 of multilayer 2 of a BML chamber.

- Dead channels: dead channels due to bad electronics/cabling are not allowed, they have to be restored by checking that all the mezzaninos and connectors are well plugged. In case of a broken wire the tube must be disconnected from HV or the wire removed. The maximum number of broken wires per chamber is 3. If this number is exceeded, an effort at repair should be made;

- ADC spectra: the ADC spectrum for all tubes is required to have a Landau shaped distribution. In Fig.5.3 a typical well shaped ADC spectrum is shown. For each individual drift tube a fit with a gaussian function of the central part of the ADC spectrum is performed. The mean value and the width are required to not differ from their mean values on all the chamber tubes by more than 5 standard deviations. ADC spectrum is also used to understand the tube noise, in fact electronic noise is composed by hits with very low charge. It can be aliminate by requiring the ADC value to be greater than 40-50 ADC counts.

- TDC spectra: For each tube the t_0 and t_{max}, the time corresponding to the edges of the time spectra, are extrapolated by fitting the spectrum with the function reported in eq. 3.2. Deviations from the mean by more than 5σ must be investigated. The t_{max} is very dependent on the gas mixture composition: if the chamber is well flushed, the t_{max} values for all its tubes is found with a spread of few ns. If larger deviation is observed, some problem in the gas mixture is expected. A high water

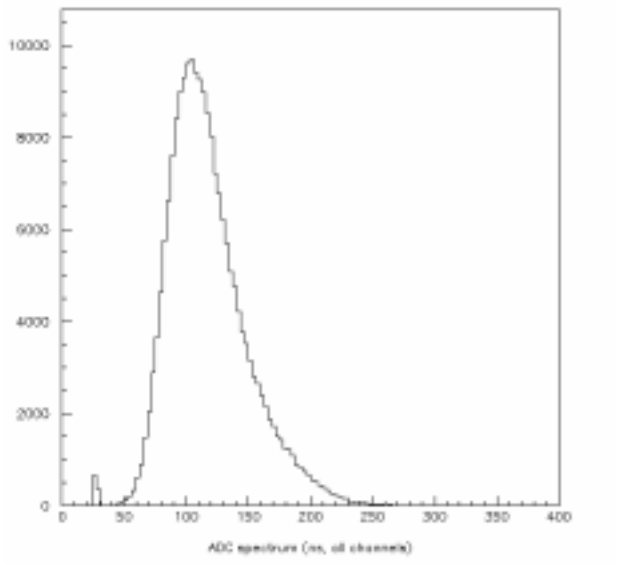

Figure 5.3: A typical well shaping ADC spectrum.

concentration in the gas mixture causes longer drift times since the electron velocity is reduced. Another reason is a CO_2 percentage greater than 7%. This second case can be distinguished from the case of excessive humdity by analyzing also the pulse height spectra: Water has a very small effect on the gas gain while additional quantities of CO_2 reduce the gain and thus shift the ADC spectra towards smaller values.

- Number of unpaired AMT edges: the number of unpaired AMT edges (leading edge found without corresponding trailing edge and vice versa) is required to be below 5% for all tubes otherwise the corresponding mezzanine must be replaced;

- Electronic noise level: the noise level is defined as the number of hit that have a drift time out of the time window, that means hits that are not correlated with a track particle. In particular at BB5 the noise level is computed taking into account hits with $t < 100$ TDC counts. The noise level has to be less than 5KHz per each tube for a threshold fixed at -50 mV. In Fig.5.4 the noise level for each electronic channel of a chamber is plotted.

5.2 Data taking in Sector 13

The installation of the Atlas muon spectrometer barrel has started in summer 2005. The sector 13 is the barrel sector in between the detector feet. It was the first sector to be installed and it has the easiest access situation in order to connect MDT's chamber to services. In this section results of the checks on the first data acquired with some chambers

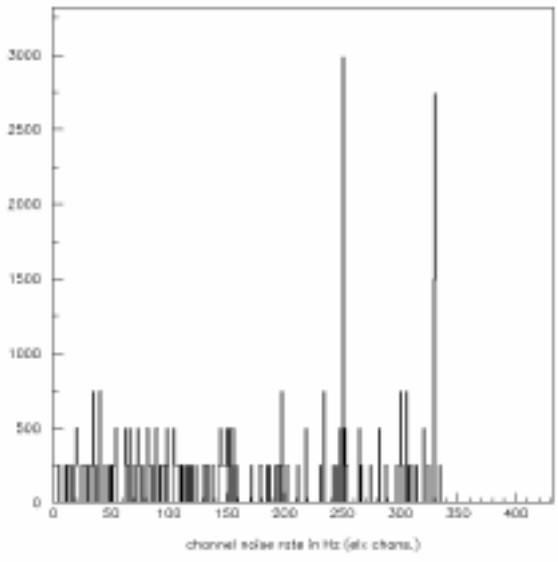

Figure 5.4: Electronic noise level (Hz) for all the electronics channel of a BML chamber.

of sector 13 is reported.

Although most of the system services were not there yet, temporary services have been installed in sector 13 to perform both a noise study in the final environment and to start reading out more than a single muon chamber from the control room (USA15) where the MROD's are located. In Fig.5.5 a picture of the installation of the BML stations in sector 13 is shown.

On the ground below sector 13, the final LV and HV power supplies based on the CAEN EASY 3000 system have been located. Chambers were connected to the supplies by means of temporary cabling. A test of the final grounding scheme, including also safety ground, was performed. Similarly, the connection of the ELMBs was done by connecting the acquired chambers with a temporary daisy chain of CanBus cables.

The standard programs ELMBloader and DCSMDT were loaded in a Windows PC in the same area. The ELMBloader was used whenever an upgrade of the ELMB was required, while the DCSMDT was used to first verify the ELMB firmware version and to initialize and check the correct functionality of temperature and B-field sensors. The latest operation is completed by controlling the voltage and temperature measurements of the CSM and of the mezzanine cards connected to it. A slow monitoring program has been installed on the DCS PC in the control room to monitor the behavior along the time of the low voltages and temperatures.

The optical fibers for the TTC and for the data readout and trigger signals were connected to the CSM's, through the final patch-panels located in the spectrometer, with the main cords coming directly from the control room. A test of their functionality was done by light firing them with a small laser and then reading out the attenuation of the transmitted light at the far end.

Figure 5.5: The sliding of a BML station in the Atlas apparatus.

After all these checks, the JTAG initialization has been performed to set the wanted thresholds on the discriminators and to adjust the readout timing.

From the detector point of view, 3 BML (1A,2A,3A) and 3 BOL (1A,2A,3A) chambers have been installed in their final positions and then connected to a temporary gas manyfold to flush them with new gas. The old H8 (see chapter 4) gas system and the neutral gas lines of Atlas have been used. The maximum flow rate of 1200 Nl/h was kept. A parallel flowing of the BML and BOL chambers was set while keeping the possibility to flush only the BML or BOL via valves mounted on the line. Safety reasons on using the gas in the pit forced us to exercise a lot of caution when flushing the chambers so that these operations were restricted to the real minimum necessary while waiting for final services. We were however able to run the gas twice, the first time on the three BMLs in October and one month later on the three BOLs.

The data taking was started in October 2005 by reading out the chambers with the two MROD's used in the H8 test beam, so providing an acquisition of up to 6×2 chambers. The readout was performed by using the DAQ program developed for readout of single VME crates, ROD Crate Daq [40]. With this standalone DAQ both noise and cosmics data taking were possible. Different upgrades of the ROD Crate Daq program were used. In the latest version, data were written with the correct Event Builder format.

5.2.1 Noise environment in the pit

As soon as the chambers arrived in the pit, a set of tests on the noise level has been carried out by studying both the final configuration of grounding and the noise dependence on the applied threshold. After trying different grounding connections it has been noticed that the noise strongly depends on the grounding of the shielding of the LV cables. In Fig.5.6 the measured noise rate without shielding is shown as a function of the channel number as the black distribution. Its level reaches up to 700 KHz/wire. In the same plot, the red distribution shows instead the noise after having grounded the shielding on the LV cable. In this case only few wires reach a counting rate of 10-20 KHz.

Moreover, the dependence of the noise on the applied threshold, V_{thr}, has also been studied. In Fig.5.7 the average value of this rate as a function of V_{thr} is shown, proving that, as expected, it reduces to one half each time the threshold is increased of 2 mV.

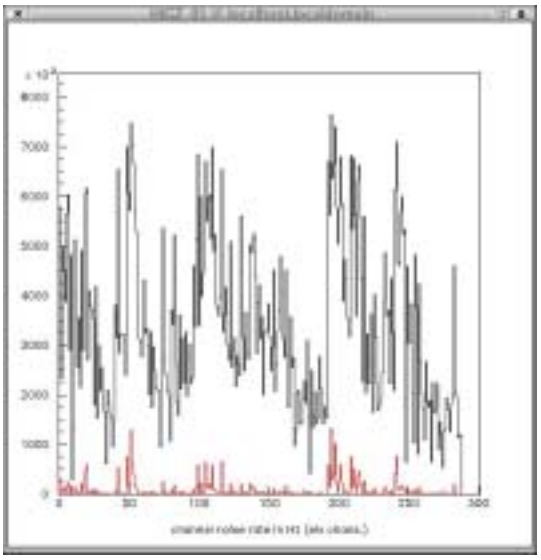

Figure 5.6: Noise rate as a function of the channel number. Black (red) curve is without (with) grounding.

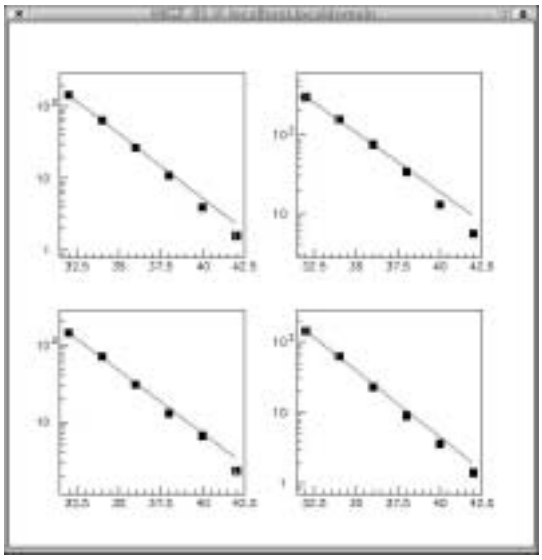

Figure 5.7: Average chamber noise (Hz) measured in the pit as a function of the applied discriminator threshold (mV).

5.2.2 Cosmics data taking with a Scintillator trigger

Since in October flushing the gas in the RPC system was not yet allowed and the LVL1 cabling was not yet completely in place, the data acquisition has started by making a simple trigger based on scintillator counters, *SciTrig*. The counters consisted of two 3.0×0.3 m slabs of plastic scintillator readout at both ends by PM, $S_j^{A,B}$. These counters have been positioned 30 cm one in top of the other and parallel along their longitudinal axes. The whole setup has then been put on the ground below the outest sector to cover almost two chambers along the η coordinate. The *SciTrig* required a 4-fold coincidence $(S_1^A \times S_1^B) \times (S_2^A \times S_2^B)$ and counted ≤ 1 Hz in the pit after having reached a plateau

in coincidence rate by adjusting the HV setting. This rate has to be compared with a trigger counting of 30 Hz at the surface which was consistent with the expected 100 Hz of double coincidence in a single counter. The trigger was formed with NIM logic in the ground of sector 13 and then brought by a 120 m long cable to the USA15 control room.

Data taking periods were restricted in time due to the difficulty to operate the HV on the chambers and to turn on the scintillators during the continuous operation of installing new chambers. However, few runs of roughly 1 hour have been taken in four months, to monitor the functionality of the chambers.

Tests of the online monitoring

While taking data the online monitoring based on GNAM[38] and the online display based on PERSINT[39] have been used.

The GNAM service was already provided in the TDAQ release used, although some specific code for the MDTs was developed by the MDT-GNAM task force. In Fig.5.8, the time distribution of a single chamber as seen by GNAM is shown. This monitoring

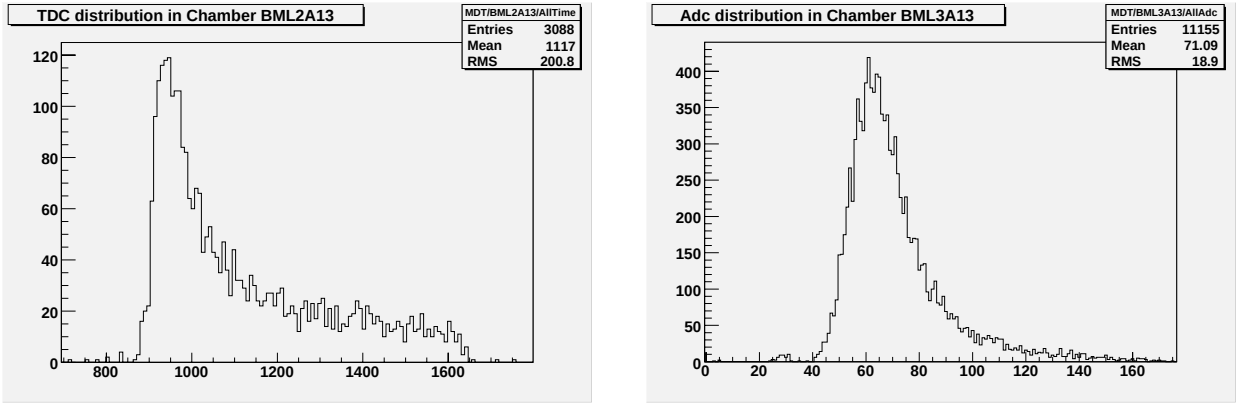

Figure 5.8: TDC (left) and ADC (right) distributions for a BML chamber as shown by the GNAM monitoring program.

tool allowed us to fine tune the readout delay needed to compensate the length of the cable bringing the *SciTrig* signal from the pit to USA15. It was also tested online that the ADC spectra were consistent with minimum ionizing peak distributions as expected for crossing tracks and that the trigger was indeed selecting crossing cosmics. This was finally proved also observing the event display based on PERSINT, which was receiving data through a specifically developed GNAM interface.

Offline data analysis without Athena

In order to have a fast feedback on the chamber functionality soon afterward data taking, two simple offline programs that were not requiring the Athena framework were developed. One of these produces a PAW ntuple with the main information on the fired channels. Here some results on the first cosmic rays data collected with sector 13 are reported.

In Fig. 5.9, a very clean time distribution is shown for one BML after integrating all wires in a multilayer. The t_0 and t_{max} of the spectrum have been extracted by fitting it with the standard curve used for the calibration procedure (see chapter 3). First testing of the offline calibration procedures have been started thanks to the acquired data. To have an idea of the expected cosmic rate in the whole sector, when RPC triggering will be available, a simple computation can be done. In 1.3 hours of data taking with the *SciTrig*, around 1000 clean straight tracks are acquired in the BML2A13 passing through all tubes/layers. Since the BML2a13 has 56 tubes this corresponds to a rate of 0.2 events/min/tube each 20 cm of wire, that is the scintillators acceptance along the wire direction. Multiplying by 20 to correct for the wire length we estimate a rate of 3.7 Hz/BML. Assuming a reasonably constant rate along η when triggering with RPC we expect $\sim$ 50 Hz on sector 13 (each sector is made of 12 chambers) for cosmics straight tracks.

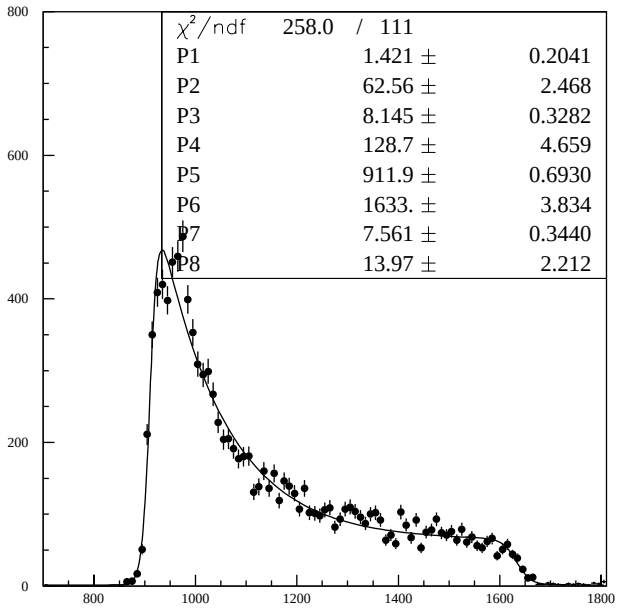

Figure 5.9: Time distribution for the BML chambers in the pit for one multilayer after one hour of cosmics data taking with the scintillator trigger.

In Fig. 5.10, the distribution of the overall ADC and TDC spectra for the two kind of chambers, BML and BOL, shows some differences:

- The ADC spectra for the BOL has an average value which is 35% higher than the

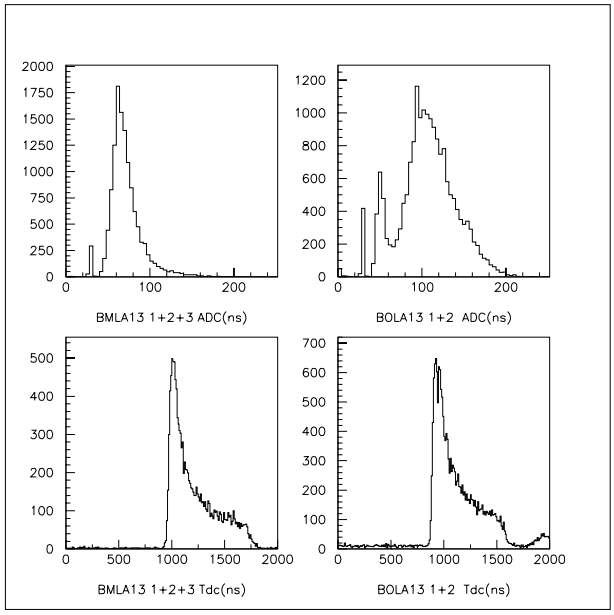

Figure 5.10: Inclusive spectra for ADC (top) and TDC (bottom) spectra for the BML (left) and BOL (right) chambers.

BML one. Since the chambers were operated at the same HV (3080 V) this is probably due to a different gas-mixture.

- Similarly, the BOL TDC spectra are 80% ns narrower in full width than the ones of the BML.

- For the BOL, there is also the presence of double hits in the distribution as shown by the population at very large times visible in the inclusive BOL time spectra. We have checked that these hits are coming with a delay of roughly 800 ns from the first hit which is consistent with the DeadTime set in the TDC.

In order to control the illumination of the chambers, obtained by triggering with the scintillators, the variable *ITube* has been constructed. ITube is a sequential tube number that starts from the BML1A and ends with the BML3A, it is proportional to the η coordinate. In the top (bottom) plot of Fig. 5.11 the BML (BOL) distribution of ITube, taking only hits with an ADC above 50 counts, is shown. For the BOL, the three chambers were not all properly connected at the same time. However the plateau of the illumination on the BML shows that the *SciTrig* well covers more than 1 chamber. In Fig. 5.12 (left), the distribution of the $\Delta Tube$ variable, i.e. the difference between the average value of ITube in one chamber and the ITube of every hit in that chamber, shows that 90% of the events are coming almost perpendicular. Indeed the $\Delta Tube$ variable is distributed with a gaussian core of ± 1 tube. While $\sim 10\%$ of the hits are due to some shower-like events produced somewhere. To better understand the source of the acquired cosmics, we plot

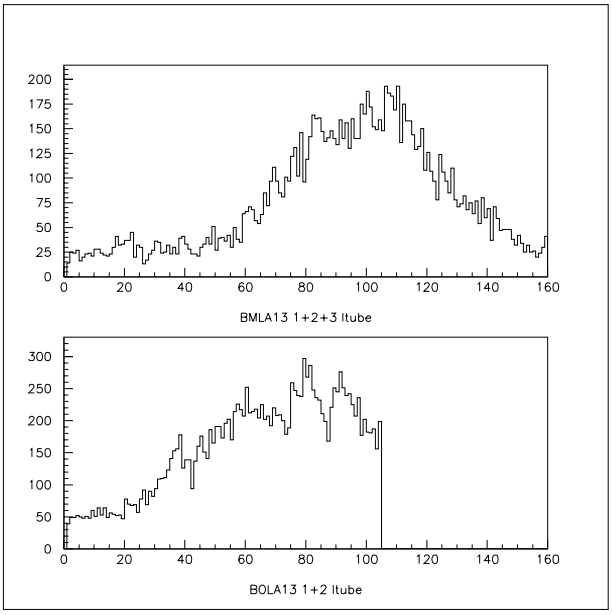

Figure 5.11: Distribution of the chamber illumination for the BML (top) and BOL (bottom) of sector 13 for run number 1008. A BOL chamber was missing in the readout.The *SciTrig* covered with almost full acceptance the BML2A13 and BOL2A13.

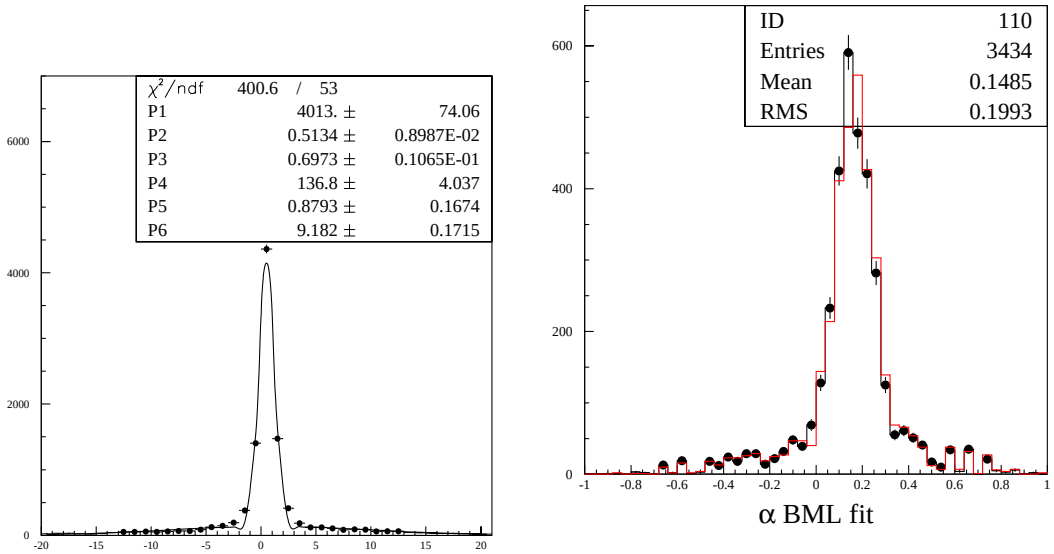

Figure 5.12: (Left) Distribution of $\Delta Tube$ variable. (Right) Distribution of the track slope.

also the slope for the events with more than 5 hits per layer in Fig. 5.12 (right). The black (red) curve represents the slope calculated with the BML (BOL) track. As expected, the

angular distribution does not follow the one at the surface indicating that the majority of the triggered events comes with an angle of +8 degrees. In other words, the best source points toward the hole of the largest shaft used for the detector installation.

In Fig. 5.13 (middle) the multiplicity distribution of fired layer is shown; where fired means at least one hit in the layer with ADC cut above 50 counts. We count 18%, 80% events with 5, 6 layers fired respectively which indicate a wire efficiency of $\sim$ 95%. In Fig. 5.13 (bottom), we instead show the distribution of number of hits for a fired layer. The situation is very clean, only few % of the events show double hits proving again that the noise in the pit-environment is well under control.

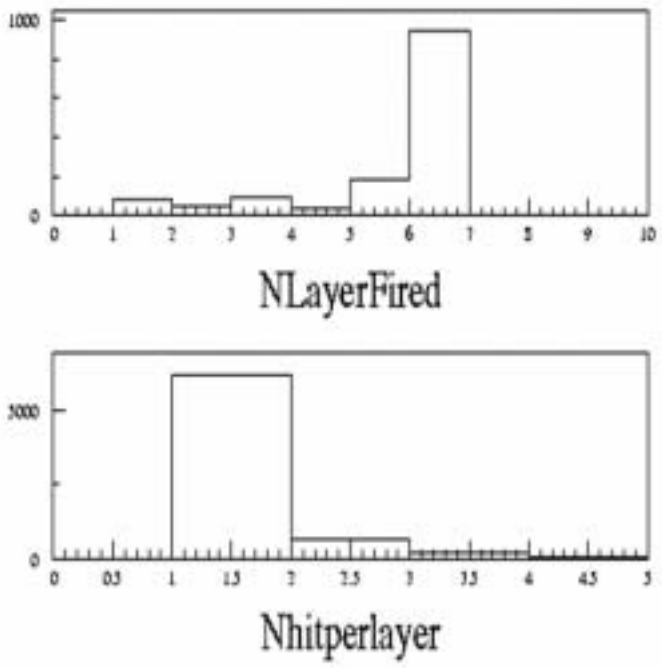

Figure 5.13: Distribution of events with candidate tracks in the BML2A13 chamber: Number of layers fired (top) and Number of hits for a fired layer (bottom).

As a conclusion, in Fig. 5.14 we show the dependence of $t_{drift} = t_{max} - t_0$, t_0 and t_{max} as a function of the data taking period. The timing values have been calculated by fitting the spectra for all chambers, or by dividing them for multilayer. The basic observation is that, since we have flushed the gas just at the beginning, while the t_0 tends to be stable, the t_{drift} has a linear growth of roughly 3 ns/day.

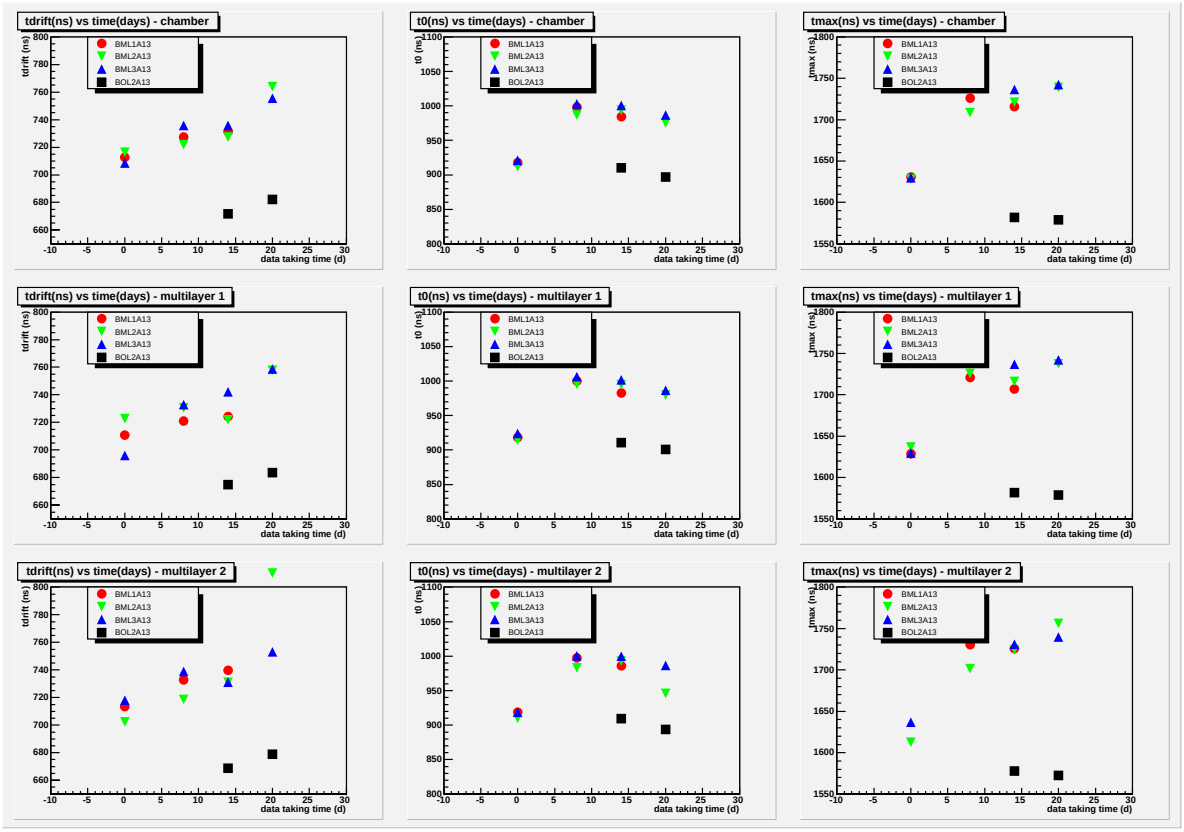

Figure 5.14: t_{drift},t_0 and t_{max} dependence along the running time for (top) all chamber, (middle) multilayer 1 and (bottom) multilayer 2.

5.2.3 First in situ calibration

The small quantity of data collected has been used as a benchmark to test how the chamber can be calibrated with cosmics. Our ntuples where used to run the autocalibration procedure (see chapter 3) integrating events in each multilayer to extract the RT relation. Only events with 6 hits on 2 multilayers have been retained for processing. The convergence of the autocalibration procedure is clearly seen in the plot of Fig. 5.15. The resulting RT relations are reasonable but not as smooth as the one obtained in H8 due to the lack of statistics. To show the quality of the data collected, an event display of the cosmic sample done with the official Atlas-Offline display, Atlantis, is shown in Fig.5.16.

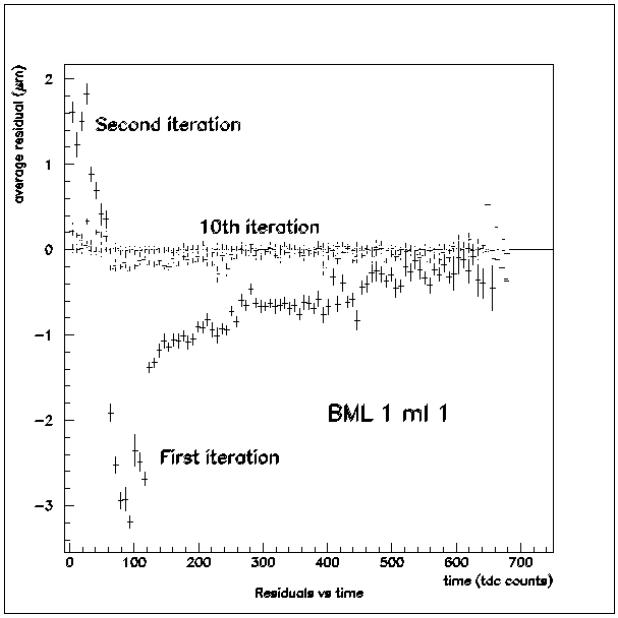

Figure 5.15: Average residuals as a function of the drift time for different iterations of the auto-calibration procedure.

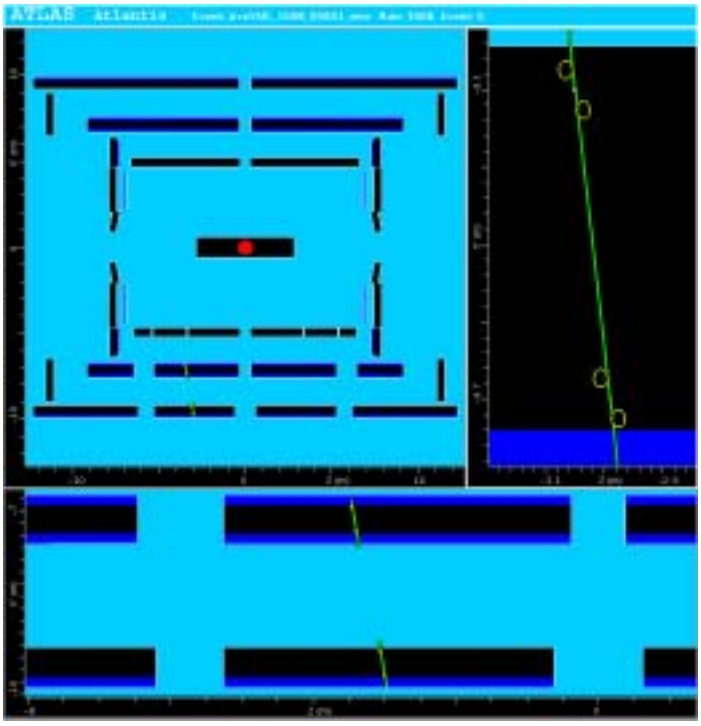

Figure 5.16: Example of one cosmic track passing through a BML and BOL chamber as view by the Atlantis display.

Chapter 6

Montecarlo study of the $\tau \rightarrow 3\mu$ decay

In this chapter, a Montecarlo study of the search for the Lepton Flavour Violating decay $\tau \rightarrow 3\mu$ with the Atlas detector is reported. As described in chapter 1, although with a very low branching ratio, this decay is expected by several models beyond the Standard Model. Observe the signal or improve the upper limit on the BR for this decay can help in distinguish the theory model describing this process. Beside an intrinsic physics interest, this channel offers also the possibility to study the reconstruction capability of the Atlas detector in hard conditions. Indeed, the transverse momentum spectrum of the three produced muons ranges from zero to $\simeq$ 30 GeV, that is a p_t range where the Atlas muon detector is not optimized to operate. Moreover, the three muons are produced very close one to each other such as to complicate the functionality of the muon reconstruction programs.

The existing best upper limit on the $\tau \rightarrow 3\mu$ branching ratio has been set by the B-factories Babar[15] and Belle[16]. They have both decreased the previous measured upper limit on this BR (published by CLEO [14]) of one order of magnitude setting it to 2.0×10^{-7}. Due to the very high luminosity expected at LHC and thus to the large amount of τ leptons produced, the Atlas detector can improve the existing limits of the $\tau \rightarrow 3\mu$ decay. Already with 10 fb^{-1}, that is the integrated luminosity in the first year of LHC running at the low-luminosity regime, Atlas can bring the BR below the 10^{-7} level. A similar analysis has already been performed by the CMS collaboration [18]. They find very promising results which encourage also study this channel with the Atlas detector.

6.1 The τ production at LHC

A large number of τ leptons is expected to be produced at LHC. At $\sqrt{s} = 14$ TeV, the extrapolated values of the total τ production cross section is expected to be $\sigma(pp \rightarrow \tau + X) \simeq O(100\mu b)$. This translates in $\simeq 10^{12}$ τ's produced in 10 fb^{-1}.

The more relevant source of τ leptons is from decays of the heavy mesons D and B. It is important to note that the theoretical uncertainties on the total QCD cross section for heavy quarks production are large (factors of 2) and only with the first runs of pp collisions at LHC these numbers will become better known. The dominant production

process comes from the decay of the strange D meson that contributes for more than 70% of the total cross section from heavy mesons.

Beside the production from B and D hadrons decays, a still relevant contribution is that from the decays of the W and Z vector bosons. Cross sections for these decays are[41]:

- $\sigma(pp \to W^+ \to \tau^+\nu_\tau) = 11.66 \pm 0.56\ nb$;
- $\sigma(pp \to W^- \to \tau^-\bar{\nu}_\tau) = 8.58 \pm 0.43\ nb$;
- $\sigma(pp \to Z \to \tau^+\tau^-) = 1.92 \pm 0.08\ nb$;

Even though the channel with the W boson has a much lower cross section than that from the heavy quark decays one, the W is the most clean source of τ leptons for this search. Indeed a very clear signal signature is expected, making easier the backgrounds rejection while offering a good detection efficiency. In this work therefore the $W \to \tau\nu$, $\tau \to 3\mu$ decay chain is considered. The main characteristic of this process are:

- high p_t τ's, the p_t distribution of the τ will be peaked around 40 GeV;
- the production through a leptonic W decay insures well isolated τ, which corresponds to have three isolated muons in the final state;
- a large amount of transverse missing energy due to the presence of a high momentum neutrino, produced together with the τ, peaked around 30-40 GeV.

In order to show how Atlas will be able to improve the present upper limit on the $\tau \to 3\mu$ branching ratio, we can compute the signal event number expected in the first year of data taking at LHC. Indeed, starting from the cross section of the $pp \to W \to \tau\nu_\tau$ decay and assuming as signal branching ratio the U.L. set by the B-factories (2×10^{-7}), already in the first 10 fb^{-1} of integrated luminosity we expect:

$$N_{expected} = \sigma_{tot}(W) \times BR_{tot}(W \to \tau\nu) \times BR(\tau \to 3\mu) \times L = 40.5, \tag{6.1}$$

where $\sigma_{tot}(W) \times BR_{tot}(W \to \tau\nu)$ is due to the sum of the contribution from the positive and negative W vector bosons, $\sigma_{tot}(W) \times BR_{tot}(W \to \tau\nu) = (20.4 \pm 0.70)$ nb.

In order to study the detector efficiencies and the analysis scheme, a large number of signal events has been generated with the PYTHIA 6.2 generator, interfaced to the Athena framework. Since the τ decay to three charged leptons is not foreseen in Pythia, the signal has been generated as a three body decay with a uniform phase space. In this way, any particular physics model can be then taken into consideration by further adding specific dynamical features. A test of the effects of a given dynamics has been later tested by adding a modeling of the $\tau \to 3\mu$ decay within the minimal supersymmetric standard model (MSSM).

The generated signal events have been then simulated both with fast and full simulation programs of the Atlas detector. Comparisons between the two simulations will be illustrated in the next sections.

The muons produced with the uniform phase space decay from the τ, have the p_t spectra shown in Fig.6.1, where they have been ordered for decreasing values of p_t. The most energetic muon has a p_t distribution that covers the range from few GeV up to $\simeq 50$ GeV, peaked at 20 GeV, the second one has a p_t distribution peaked at 7-8 GeV, while the third muon has a very low p_t spectrum. About 55% of the events have a third muon with a p_t from 3 to 6 GeV. The capability of Atlas in detecting these low-p_t muons is crucial to improve the efficiency for this search. For what concern the pseudorapidity distributions, those are shown in Fig.6.2 for the three muons. Each muon covers a pseudorapidity range $|\eta| < 6$.

6.2 The backgrounds

6.2.1 General considerations

The background for the process under investigation is constituted by all the processes having three muons in the final state very close in $\Delta\eta\Delta\Phi$ and with an invariant mass of the three muons close to the τ mass. The main source of background is expected to come from the production of c and b quarks. They will produce heavy mesons that can originate, with a semileptonic decay, light mesons (ϕ, η) and a $\mu\nu$ pair. The light meson can then originate $\mu^+\mu^-$ or $\mu^+\mu^-\gamma$ pairs. For instance a background source is from the decay chain $D_s \to \phi\mu\nu$ with the ϕ decaying in $\mu^+\mu^-$. The production of heaviest mesons, like for example J/ψ, Υ, does not represent a source of background since in this case the three muons of the final state will have an invariant mass above the τ mass. Moreover, there is also the possibility that other processes with fake leptons will give a smaller contribution. Channel such as $D_x \to \phi\pi$ with π decaying in flight or π punching-trough the calorimeter will be simulated in a second stage. Also cosmic muons can be easily tagged and rejected by timing considerations.

To produce the backgrounds the generator PythiaB has been used. PythiaB is a Pythia version optimized for heavy quarks production, in particular for B-physics studies. PythiaB takes into account all the possible processes that produce single heavy quark or pair of heavy quarks. The hard production processes are three: *gluon-fusion*, *quark-fusion* and *flavor excitation*. The first two correspond to the production of a quark pair by gluon fusion or by the annihilation of light quarks via the two parton subprocesses, $gg \to c\bar{c}$, and $q\bar{q} \to c\bar{c}$. The flavor excitation consists in the scattering of a c or $\bar{c}$ quark out of the initial state into the final state by a gluon or by a light quark or antiquark via the subprocesses $gc \to gc$, $qc \to qc$ or $\bar{q}c \to \bar{q}c$ and the corresponding three $\bar{c}$ subprocesses. The Feynman diagrams of the three production processes are shown in Fig. 6.3. The same processes are also considered for the b-quark production.

The total heavy quark production cross sections are $\simeq 10$ mb for the c-quark and $\simeq 500$ μb for the b-quark, with very large uncertainties. In order to attach a systematic error to the evaluation of the production cross sections provided by the PythiaB generator their values have been compared using the analytical calculation provided by the FONNL program. FONLL[43, 44] is a program which calculates heavy quark transverse momentum

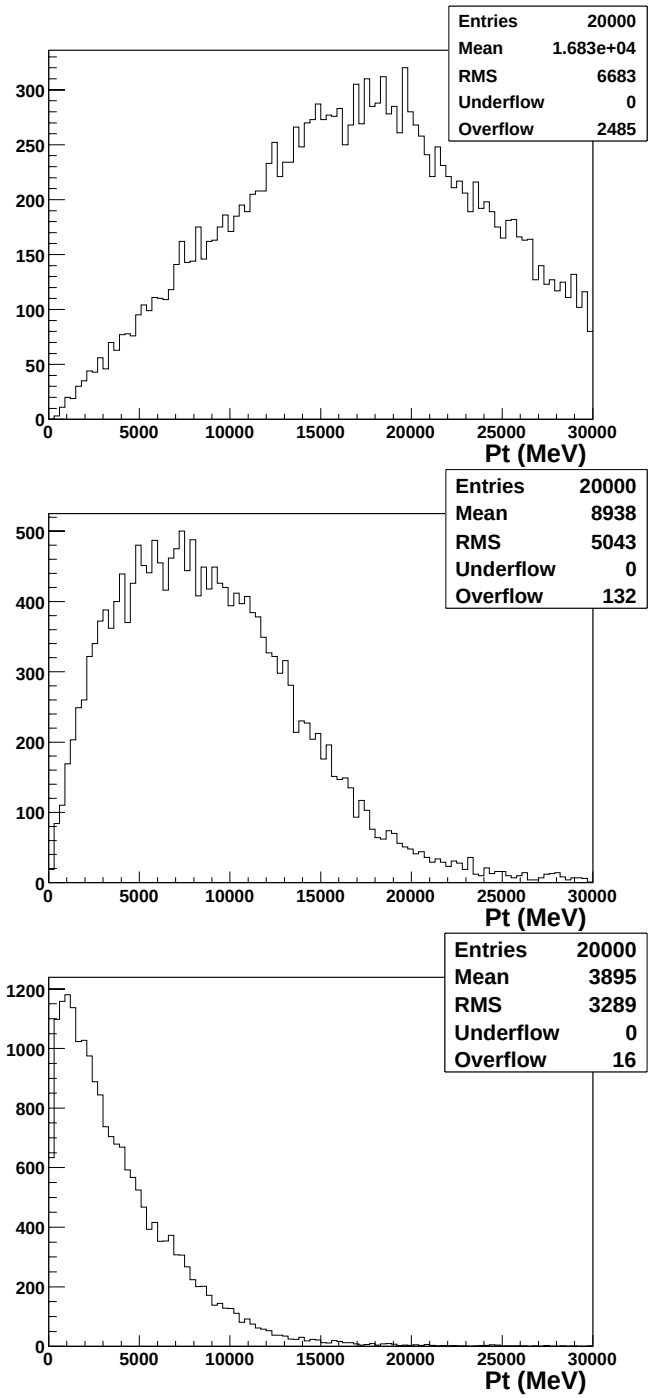

Figure 6.1: Transverse momentum distribution (montecarlo truth) for the three muons produced by the τ assuming a uniform phase space decay. The muons are ordered for decreasing values of p_t.

and rapidity distributions in hadron-hadron and photon-hadron collisions, matching Fixed Order next-to-leading order terms and Next-to-Leading-Log large-p_t resummation. In

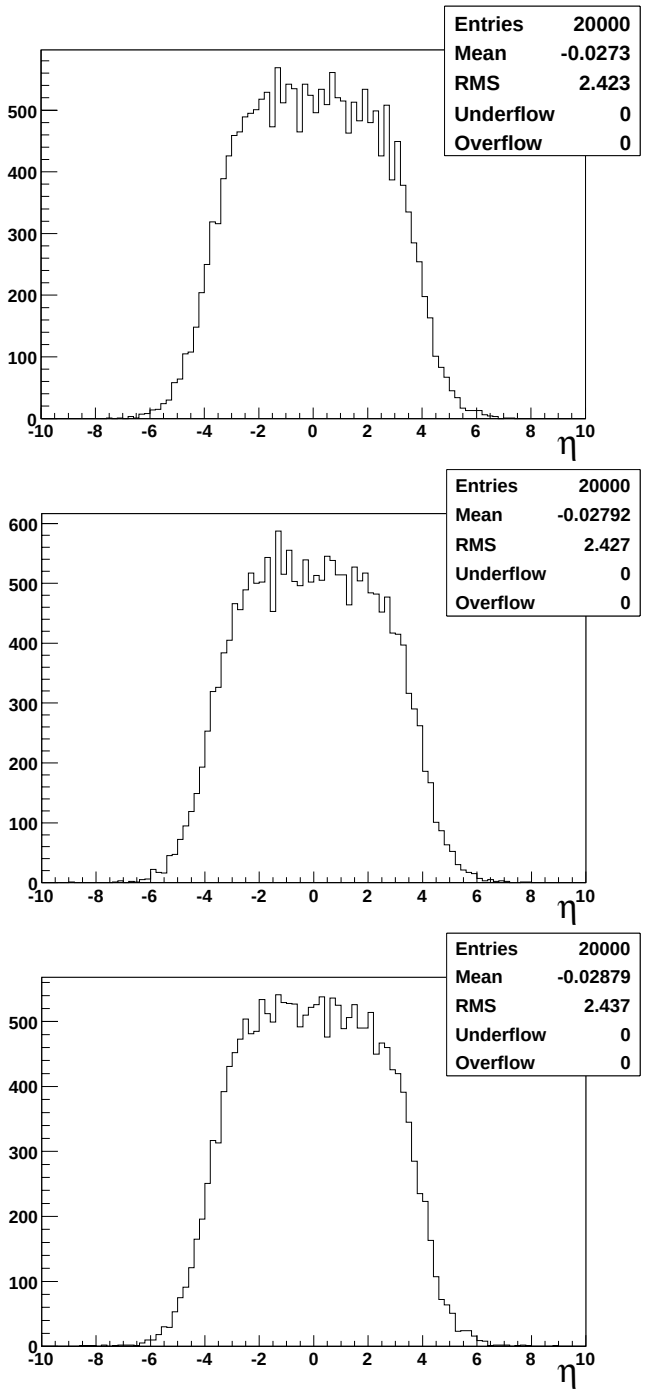

Figure 6.2: Pseudorapidity distribution (montecarlo truth) for the three muons of the signal.

Fig.6.4, the cross section for production of the b quark is shown as a function of the transverse momentum of the B mesons created, from the hadronizzation of the b quark, in the pseudorapidity range $|\eta| < 1.2$. In this plot both the cross section computed by

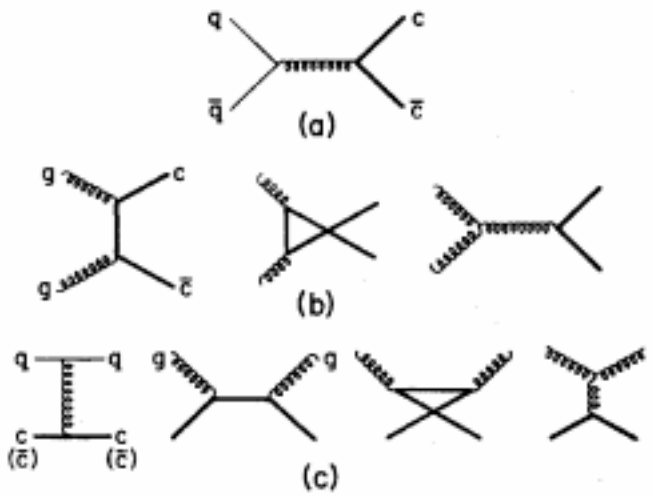

Figure 6.3: Feynman diagrams of the heavy quark production processes: (a) quark-fusion, (b) gluon-fusion and (c) flavor-excitation.

PythiaB and by the FONLL program are shown. The agreement is very good, apart small discrepancy in the low-p_t range $p_t < 5$ GeV.

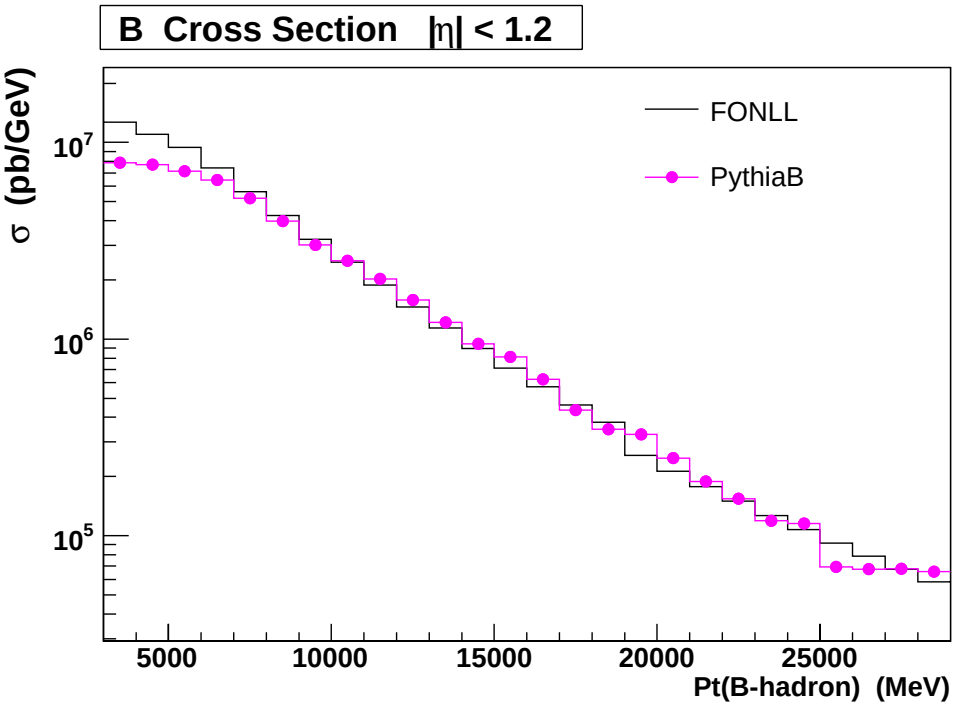

Figure 6.4: Cross section as a function of B hadrons transverse momentum for the PythiaB generator and for the FONLL program.

As shown in Fig.6.5, there are two topologically different way to produce a final state with three muons starting from c or b production. In the first kind of background, a muon is produced from one heavy meson of the event and the other two muons are produced from the other heavy meson, back to back from the first. This kind of events does not represent a real source of background since they are completely removed by requiring the three muons to be in the same hemisphere of the detector. This kind of events counts for a total branching ratio of the order 10^{-3}.

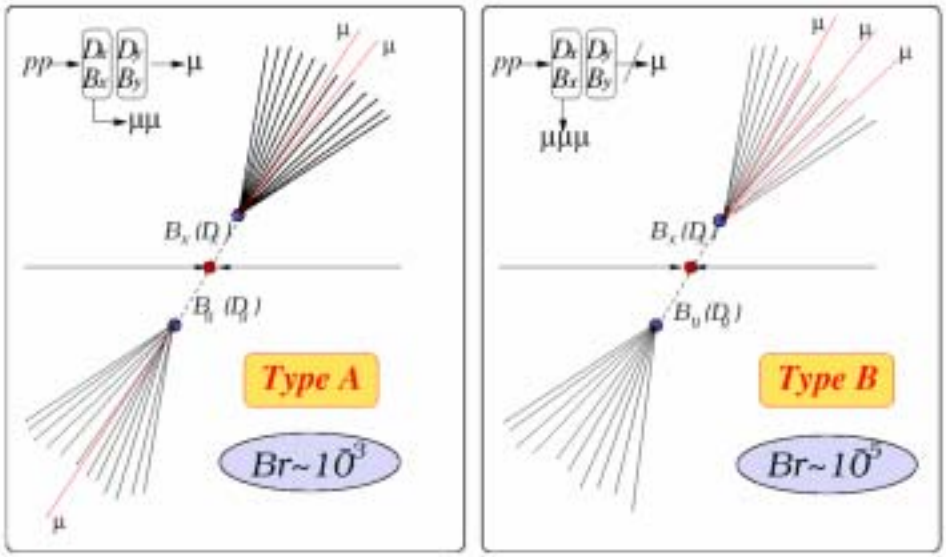

Figure 6.5: Background from heavy meson decay: in the events of type A (left) two muons are produced in a branch of the event while the third is produced in the other branch. In the events of type B (right) the three muons are produced in the same hemisphere.

An important source of background is instead due to processes where the semileptonic decays of D_X and B_X are developed in the same hemisphere of the event. This kind of events counts for a total branching ratio of the order of 10^{-5} as shown in Tab.6.1.

6.2.2 Background production from selected decay chains

The most unbiased way to produce the background, in order to be sure not to exclude any background source, should be to generate a huge number of inclusive c and b-quark events, and to search for events with three muons in the final state. Unfortunately, this work would take such a large CPU time that it is realistically not possible. To study the background rejection we have therefore considered specific decay chains by starting from the heavy quark production processes giving rise to three muon final state in the same hemisphere. As shown in the previous paragraphs, the most probable ones have been selected by looking at the Particle Data Group by searching the decay chains with the largest branching ratios.

The backgrounds considered as the most relevant ones are reported in Tab.6.1 together with their production cross sections as obtained from the PythiaB generator and the branching ratios for the various decay steps.

	$\sigma(mb)$	Decay Chain	BR	Evt	ϵ_{filter}	Filtered Evt
$D_s\phi$	6.1	$D_s \to \phi\mu\nu$	2.4%			
		$(\phi \to \mu\mu)$	(2.86×10^{-4})	450×10^6	1.82×10^{-4}	80000
$D_s\eta$	6.1	$D_s \to \eta\mu\nu$	3.1%			
		$(\eta \to \mu\mu\gamma)$	(3.1×10^{-4})	640×10^6	1.40×10^{-4}	90000
$B_s\phi$	0.78	$B_s \to D_s\mu\nu$	7.9%			
		$(Ds \to K\phi)$	$(< 6.0\times10^{-4})$			
		$(Ds \to \pi\phi)$	(4.4×10^{-2})			
		$(Ds \to \rho\phi)$	(8.2×10^{-2})			
		$(\phi \to \mu\mu)$	(2.86×10^{-4})	24×10^6	8.2×10^{-5}	2000
$B_s\eta$	0.78	$B_s \to D_s\mu\nu$	7.9%			
		$(Ds \to K\eta)$	$(< \times10^{-4})$			
		$(Ds \to \pi\eta)$	(2.1×10^{-2})			
		$(Ds \to \rho\eta)$	(13.1×10^{-2})			
		$(\eta \to \mu\mu\gamma)$	(3.1×10^{-4})	30×10^6	3.4×10^{-5}	1000

Table 6.1: Main background processes. The cross section production, the branching ratio for the various chain steps, the number of events produced in 10 fb^{-1}, the filter efficiency and the number of expected events in 10 fb^{-1} after the filter are reported.

The number of expected background events in the first year of data taking at LHC (10 fb^{-1}) is very large. As an example, the decay chain $pp \to D_sX \to \phi\mu\nu X$ with $\phi \to \mu\mu$ will produce:

$$N_{exp} = \sigma(pp \to c(\bar{c})) \times A \times BR(D_s \to \phi\mu\nu) \times BR(\phi \to \mu\mu) \times L \simeq 450 \times 10^6 \qquad (6.2)$$

events. In the eq. 6.2 A $= N(c(\bar{c}) \to D_s)/N(c(\bar{c}) \to all)$ represents the probability to create a D_s meson from the hadronizzation of the c-quark as estimated by the Pythia generator.

Due to the large number of background events to be produced, an event filter has been applied at the generation level, retaining only the events that satisfy minimu requirements regarding detector acceptance and trigger. In particular, since the Atlas Muon Spectrometer covers a pseudorapidity range of $|\eta| < 2.5$, we are not interested in events with muons generated outside of this range. The LVL1 trigger will select events with two muons by requiring a trigger threshold of 6 GeV in p_t. For this reason, given the fast turn on of the trigger efficiency curves the events have been generated asking for two muons with $p_t > 5$ GeV. The momentum threshold applied has been chosen below the nominal one to take into account momentum resolution effects. Indeed the resolution in the measurement of the muon transverse momentum is about 4-5 % for muon with $p_t \simeq 6$ GeV.

Moreover, muons with a p_t smaller than 3 GeV have a small probability to escape from the calorimeters and reach the Muon Spectrometer. Thus the presence of a third muon with $p_t > 3$ GeV is required. Summarizing, the background events have been filtered by asking two muons with $p_t > 5$ GeV and a third one with $p_t > 3$ GeV. These three muons must have a pseudorapidity in the range $|\eta| < 2.5$. Only background events that satisfy these conditions have been passed to the fast and full simulation programs of the Atlas detector. The efficiencies of the filter applied on the background events are reported in Tab.6.1, they take into account both the p_t and η cuts on the three final state muons and the ratio A.

The distribution of the transverse momenta of the three muons, ordered for decreasing p_t values, for the first background ($D_s\phi$) are reported in Fig.6.6[1]. A number of events

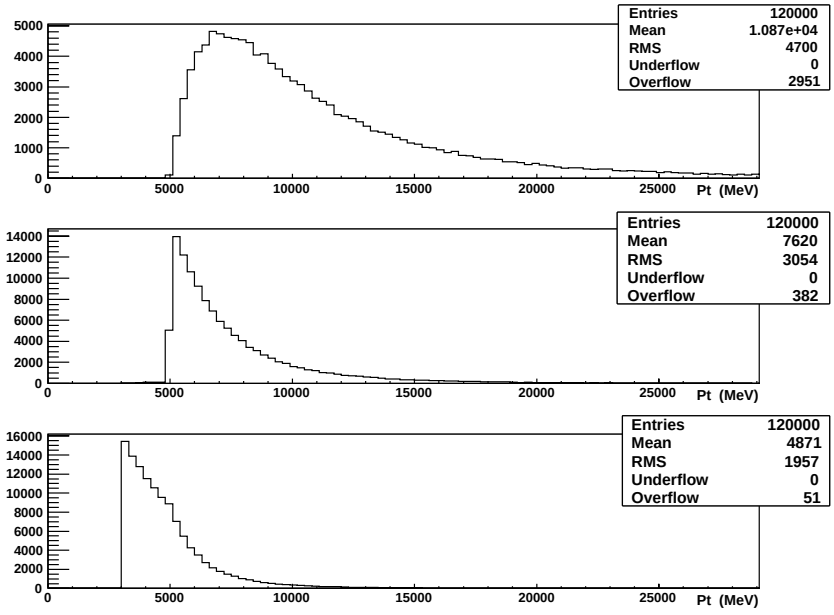

Figure 6.6: P_t distributions for the three muons of the $D_s\phi$ background. The muons are selected with $p_t > 5$ or $p_t > 3$ GeV at the generation level.

corresponding to an integrated luminosity of 20 fb^{-1} has been generated for the backgrounds $D_s\phi$ and $D_s\eta$. Because of the smaller event number expected in 10 fb^{-1} for the backgrounds $B_s\phi$ and $B_s\eta$, it has been possible to achieve a very high statistics, corresponding to 50 fb^{-1} and 100 fb^{-1} respectively. The four background processes have been simulated with the fast simulation program of Atlas together with the signal events. Due to the large time that the full simulation requires only the first background ($D_s\phi$) has been fully simulated together with the signal.

[1]In this chapter, the background from the decay chain $D_s \to \phi\mu\nu(\phi \to \mu\mu)$ will be taken as representative for the distributions of all the background processes of Tab. 6.1 unless some variable shows a more specific or different behavior.

6.3 Fast Simulation with ATLFAST

In order to have a first estimate of the signal and backgrounds rates in the Atlas detector, the generated events have been passed through the fast simulation program of Atlas, ATLFAST [45]. This package attempts to reproduce as well as possible the expected Atlas detector properties in terms of mass and momentum resolution. Not all the detector effects are parametrized in this simulation and only the basic information of the detector geometry are used by the package. Examples of the basic geometric information are: the η coverage for internal trackers and for the calorimetry, the size of the barrel/endcap transition region for the electromagnetic calorimeter, and the granularity of the calorimeters.

Concerning the muons, Atlfast applies a smearing to each true muon momentum according to a resolution which depends on the muon p_t, η and ϕ. Three smearing options can be used depending on which subdetectors are assumed to be used for the muon measurement: muon system stand-alone, inner detector stand-alone and combined. The combined resolution has been used in this analysis.

The Atlfast program does not introduce any inefficiency effects either the one related to the reconstruction programs or to the trigger.

6.3.1 Analysis Chain of ATLFAST simulated events

The events simulated with the Atlfast program have been submitted to a series of selection cuts in order to reject the background while maintaining the highest possible signal detection efficiency.

At the beginning of the analysis the invariant mass spectrum of the three muons for the signal is shown in Fig.6.13. Fitting this distribution with a gaussian function leads to the following values:

$$< M_{3\mu} >= 1777.38 \pm 0.16 \;\; MeV \tag{6.3}$$

$$\sigma(M_{3\mu}) = 16.14 \pm 1.2 \;\; MeV. \tag{6.4}$$

The analysis selection criteria are the following:

- **Preselection**
  A preselection on the reconstructed p_t and η of the three muons is required in order to take into account the fact that the Atlfast program does not include any detector inefficiency. Similarly to what done in the filter at generated levels we impose cuts on the muon pseudorapidity. Only muons produced in $|\eta| < 2.5$, i.e. in the acceptance of the Muon Spectrometer, and with a minimum p_t of 3 GeV are kept. The momentum cut allows to eliminate the events in which the muons have a low probability to pass the calorimeter layers and reach the Spectrometer. The threshold of 3 GeV represents the average energy loss for a muon traversing the calorimeters at normal incidence (i.e. in the Barrel). In the endcaps the calorimeter

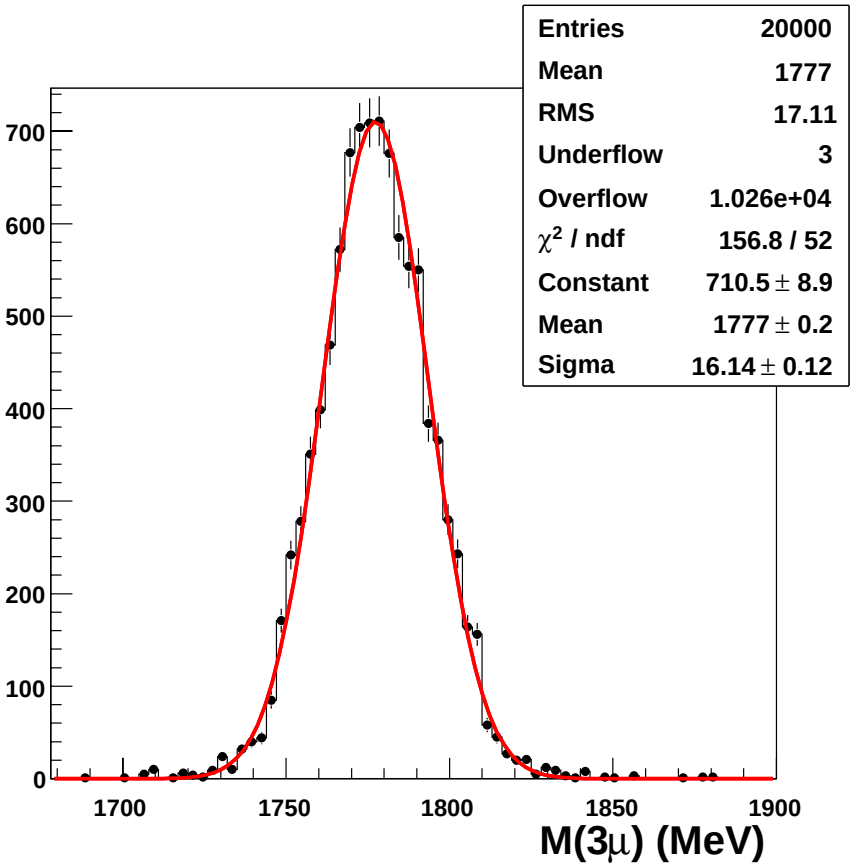

Figure 6.7: Invariant mass of the three muons from $W \rightarrow \tau\nu$, $\tau \rightarrow 3\mu$ decay as simulated by Atlfast.

geometry differs and the energy absorption sets a limit on p rather than p_t:$p_t > E_{loss} \times \sin\theta$, where E_{loss} is about 4 GeV and $\sin\theta$ can be as small as 0.17, thus bringing the calorimeter threshold down to 1 GeV at high η.

We remind that the signal events have been generated without any filter at the generation level, while the background events have been filtered as shown in section 6.2.2. For this reason the preselection affects the reconstructed backgrounds only in a minimum way.

- **Trigger cut**
  In the LVL1 muon trigger of Atlas a low-p_t Di-muon trigger, selecting two muons with $p_t > 6$ GeV, and a high-p_t muon trigger, selecting one muon with $p_t > 20$ GeV, are foreseen. The low-p_t muon LVL1 trigger efficiency is shown in Fig. 6.8 for the barrel (left) and for the endcaps (right). In order to take into account the LVL1 muon trigger efficiency, the curves of Fig. 6.8 have been parametrized with an analytical function and used to apply with the hit-or-miss method the LVL1 trigger efficiency.

For what concerns the high level trigger (HLT), that is composed by the LVL2 trigger and the Event Filter, specific considerations have to be taken into account for the $\tau \rightarrow 3\mu$ signal. Indeed the HLT trigger rate must be limited to 100-200 Hz of which not more than 10-20 Hz will be dedicated to Di-muon triggers. In order to fulfill this constraint, the generic $c\bar{c}$ and $b\bar{b}$ events will be prescaled while specific algorithms are developed to keep the most interesting events (J/Ψ,Υ). The prescale factor is too large for the rare search we are studying. For this reason, we are developing a specific HLT algorithm where more requirements are applied to the events in order to retain the signal while rejecting most of the generic $c\bar{c}$ and $b\bar{b}$. At the moment we are proposing to add to the requirement of two muons with p_t > 6 GeV, a cut on the missing transverse energy (MET). After correcting it for the muon candidates (see section 6.5.2) we will accept only events with MET greater than 20 GeV. In this case the signal efficiency is more than 60% while less than $\simeq$ 10% of the $c\bar{c}$ and $b\bar{b}$ background are maintained.

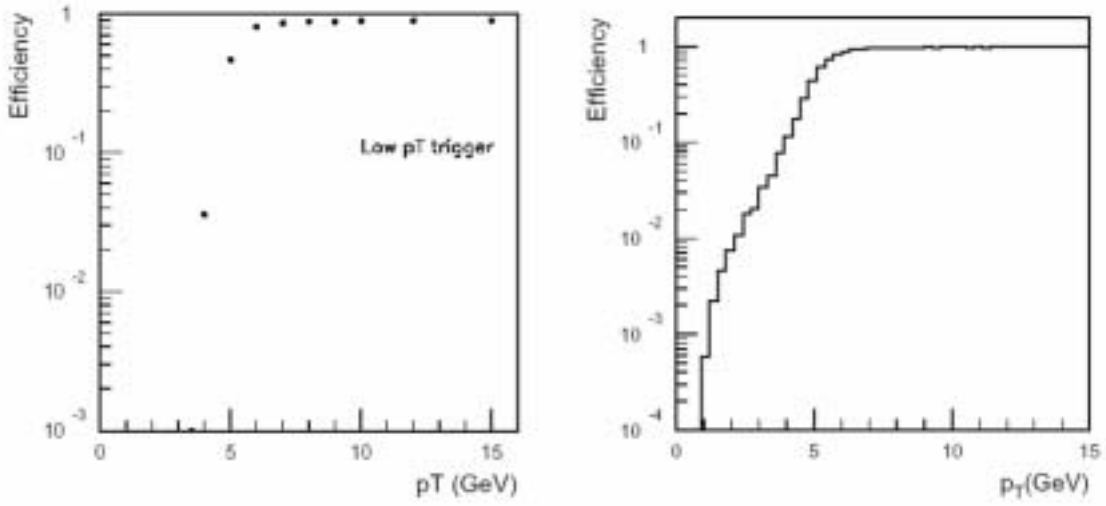

Figure 6.8: Trigger efficiency for the low-p_t trigger threshold for the barrel (left) and for the endcaps (right). The trigger efficiency for low-p_t (< 6 GeV) muons in the barrel is lower than in the endcap since in the barrel the central calorimeter acts as a barrier to muons with $p_t < 3$ GeV while in the endcaps the threshold is $\simeq 1$ GeV.

- **Isolation**
  Atlfast divides the muons in two categories, isolated and non isolated. The isolation criteria [45] are based on the η and ϕ distance, $\Delta R = \sqrt{\Delta\eta^2 + \Delta\phi^2}$, between the calorimeter cluster associated to the muon and all other calorimeter clusters and the maximum transverse energy deposition, ${E_T}^{iso}$, in the calorimeter cells surrounding the muon direction in a cone. A muon is considered to be isolated if it satisfies the following conditions:

– $\Delta R > 0.4$ from all calorimetric clusters;

– $E_T^{iso} < 10$ GeV in a cone $\Delta R < 0.2$ around the muon.

The requirement to have at least three isolated muons in the final state is very severe for the backgrounds, where the three muons are produced from D, B or light mesons decays. In Fig. 6.9 the number of isolated and non isolated muons for the signal (left) and for the $D_s\phi$ background (right) are shown. For the signal, more than 95% of the events that have passed the trigger cut have three or four isolated muons. A cut on the events asking the presence of three or four isolated muons is applied. For background the fraction of events with three or four isolated muons in the final state is $\simeq 20\%$.

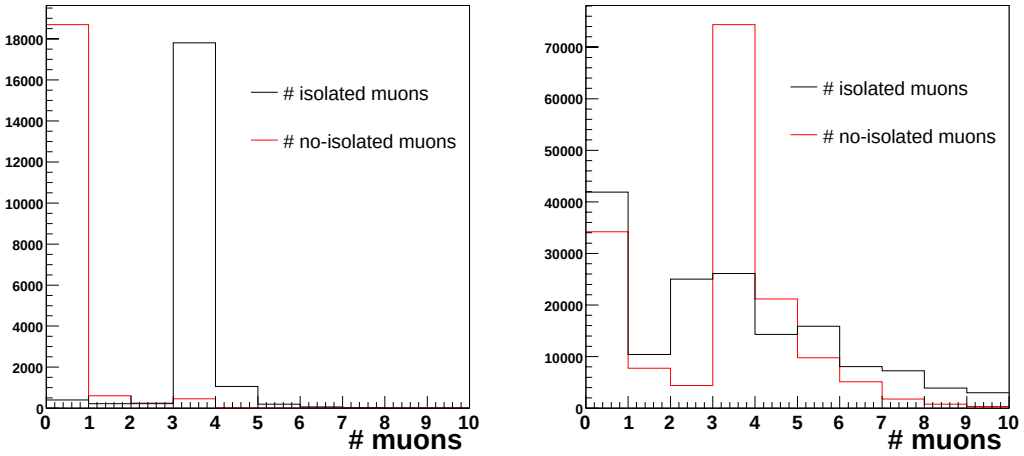

Figure 6.9: Number of isolated and non-isolated muons per event for the signal (left) and for the composition of the four backgrounds (right).

- **Missing Energy**
  The three muons of the signal will be produced together with a high energy neutrino from the decay $W \rightarrow \tau\nu$. This translates in a transverse missing energy, E_T^{miss}, distribution which shows the usual Jacobian peack at 40 GeV. The distribution of the missing transverse energy for the background events is instead peaking at very low values. In Fig. 6.10 the E_T^{miss} distribution for the events that passes the trigger cut is shown for the signal (left) and for the background $D_s\phi$ (right). A cut on the missing transverse energy at 20 GeV is required to gain in the S/B ratio which in the real data will reconfirm the selection applied at HLT.

- $\Delta\mathbf{R}_{ij}$
  The three isolated muons produced from the τ decay are almost collinear, as expected for the decay of a light object boosted in energy of $\simeq 40$ GeV. Looking at the

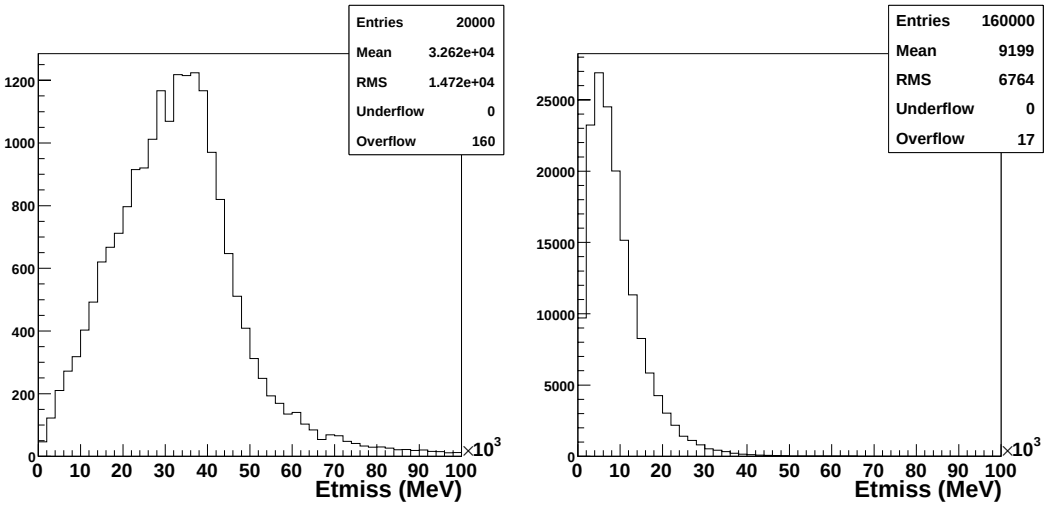

Figure 6.10: Missing transverse energy distribution for the signal (left) and for the background (right).

simulation, the three muons from the $\tau \rightarrow 3\mu$ decay are indeed practically contained in a cone of ΔR < 0.2. The $D_s\phi$ and $D_s\eta$ backgrounds are not too much rejected by this cut since also for these processes the produced muons are contained in a narrow cone. The cut $\Delta R_{ij} < 0.2$ is instead effective on the rejection of the $B_s\phi$ and $B_s\eta$ channels due to the larger mass of the decaying particle. In Fig. 6.11 the ΔR_{ij} variable is shown for signal (left) and for the $B_s\phi$ background (right).

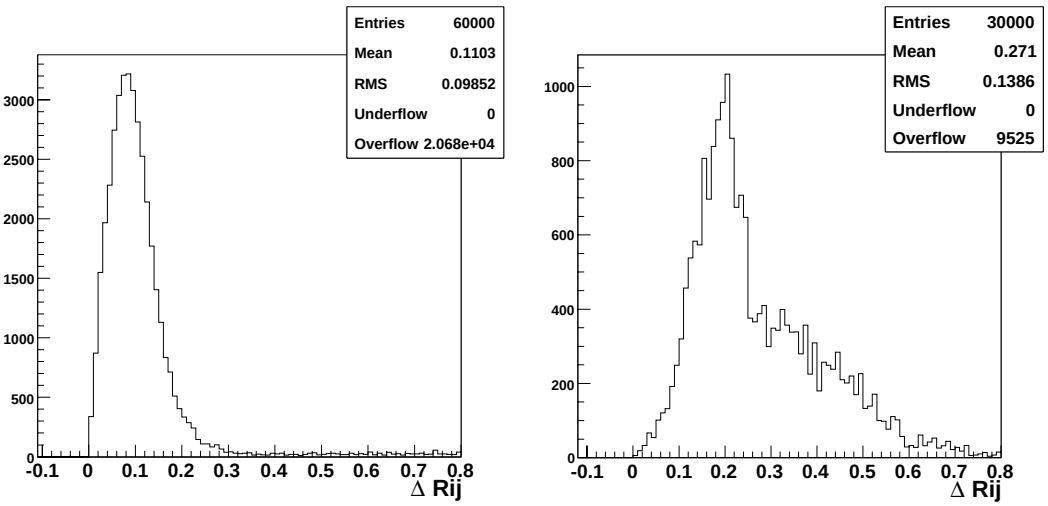

Figure 6.11: Distance in η and ϕ directions between the produced muons for the signal (left) and for the B_s background (right).

- **ϕ-veto**

  To reject the background where two muons are produced from the decay of a ϕ meson, the variable $M_{closest}$, i.e. the invariant mass of the muon pair closest to the ϕ mass and with null total charge is used. The distribution of the $M_{closest}$ variable is shown in Fig. 6.12 for the signal (left) and for the background $D_s\phi$ (right). From the plots it is clear that the signal has a flat di-muon invariant mass distribution, while for the background a narrow peak centered at the ϕ resonance mass value is visible. Fitting the $M_{closest}$ distribution for the background with a gaussian function the following values are found:

$$< M_{closest} >= 1019.76 \pm 0.07 MeV \tag{6.5}$$

$$\sigma(M_{closest}) = 9.81 \pm 0.06 MeV. \tag{6.6}$$

  Only the events with $M_{closest}$ outside a window of $3\times\sigma(M_{closest})$ with respect to its mean value are retained for further analysis.

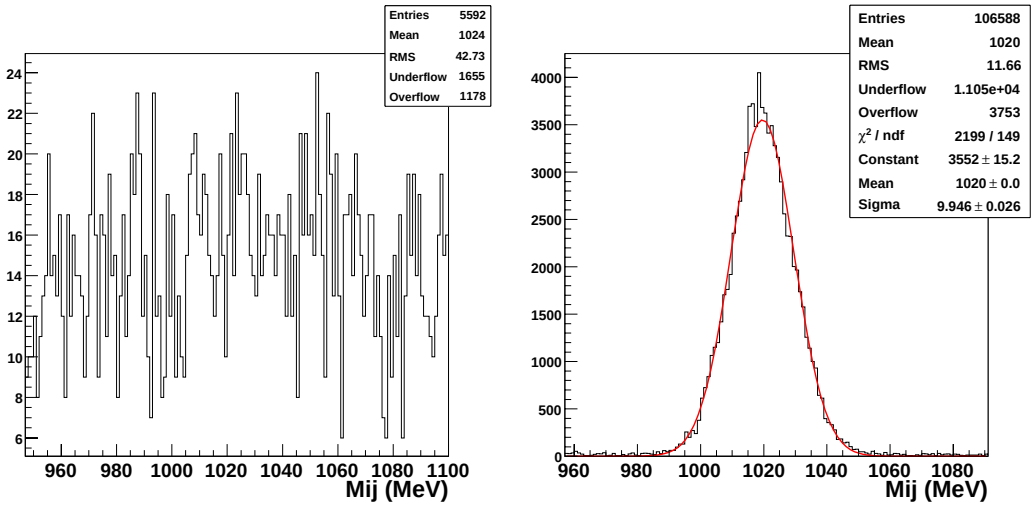

Figure 6.12: Invariant mass distribution of the muon pair with invariant mass closest to the ϕ mass for the signal (left) and for the background $D_s\phi$ (right).

  This cut is not so efficient for the background with the production of a η meson. In this case two of the three final state muons are produced from the η decay, $\eta \to \mu\mu\gamma$, together with a low energy photon and is not possible to apply a stringent constraint on the η resonance mass. We are still investigating the search of the photon to see if we can improve on this rejecetion.

- **3μ total sign**
  Only the events having the sum of the charges for the three isolated muons consistent with ± 1 (i.e. the ones compatible with a decay of a charged lepton) are kept.

- **τ window cut**
  At the end of the analysis chain only the events with an invariant mass of the three selected muons close to the τ mass are counted. The invariant mass spectrum of the three muons, $M_{3\mu}$, for the signal is shown in Fig.6.13. A fit to this distribution with a gaussian function leads to the following values:

$$< M_{3\mu} >= 1777.38 \pm 0.16 MeV \tag{6.7}$$

$$\sigma(M_{3\mu}) = 16.14 \pm 1.2 MeV. \tag{6.8}$$

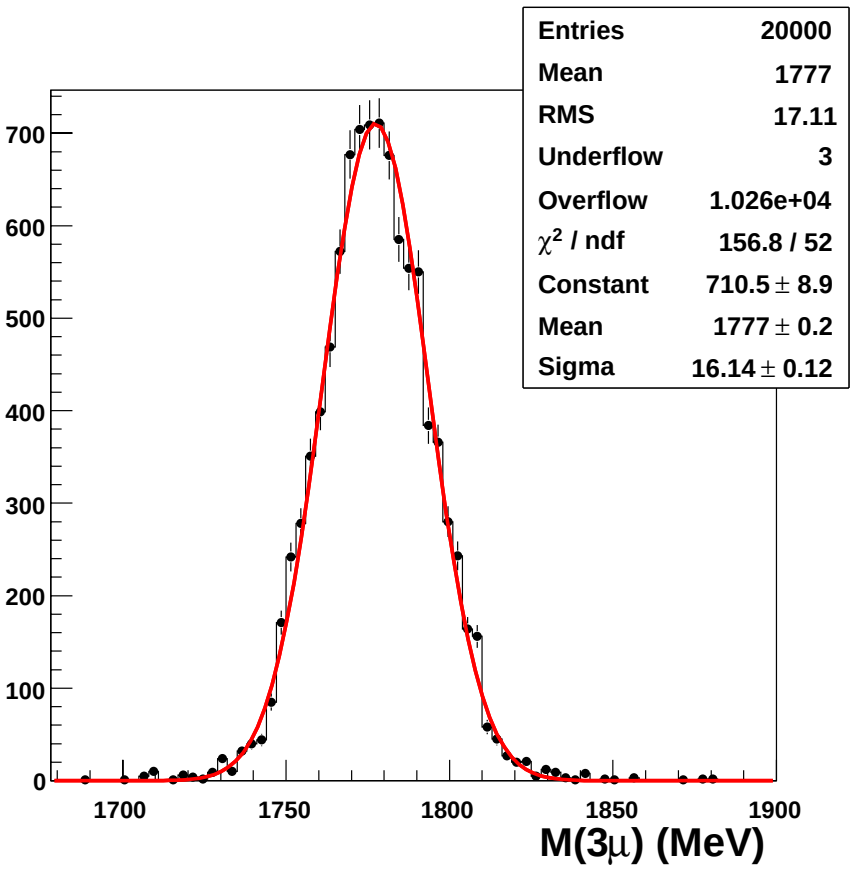

Figure 6.13: Invariant mass of the three muons from $W \rightarrow \tau\nu$, $\tau \rightarrow 3\mu$ decay as simulated by Atlfast.

We retain events with $M_{3\mu}$ in the τ mass window : $M_\tau \pm 3{\times}\sigma(M_\tau)$.

The number of events that survive the selection cuts are reported in Tab.6.2 for the signal and the four backgrounds. As it can be observed apart from the preselection, the most relevant rejection is provided by the isolation and missing energy cuts. Of great importance are also the ΔR and ϕ cuts.

The global signal detection efficiency obtained is $18.78 \pm 0.39\%$. Assuming a branching ratio of 2×10^{-7} for the signal, 7 signal events are expected in 10 fb^{-1}. Concerning the backgrounds, 1 event for the $D_s\phi$ channel and 1 event for the $B_s\eta$ channel survive the selection. Since a number of background events larger than the one expected in 10 fb^{-1} has been generated, these countings correspond to 0.5 event for the $D_s\phi$ background and 0.1 events for the $B_s\eta$ background.

	Signal	$D_s\phi$ (20 fb^{-1})	$D_s\eta$ (20 fb^{-1})	$B_s\phi$ (50 fb^{-1})	$B_s\eta$ (100 fb^{-1})
Generated	20000	160000	180000	10000	10000
Preselection	6410	159083	169314	9947	7126
Trigger	5888	123134	131656	7721	5598
Isolation	5192	23921	12263	1353	464
Missing Energy	4555	894	718	73	28
ΔR	4378	767	674	12	12
ϕ-veto	3787	45	646	0	11
Sign(3μ)	3787	38	639	0	11
τ-window	3756 (7.1)	1 (0.5)	0	0	1 (0.1)

Table 6.2: Number of events at the various analysis steps for the signal and the four backgrounds.

In Fig.6.14 the invariant mass of the system of the three muons is plotted for the signal and for the four backgrounds at the various steps of the analysis chain. The first plot refers to the events that survive the trigger cut, the second to the events that survive the requirement of three isolated muons in the final state, the third is after the cut $E_t^{miss} >$ 20 GeV cut and the last is after the ϕ-veto cut. The distributions are all normalized to an integrated luminosity of 10 fb^{-1}.

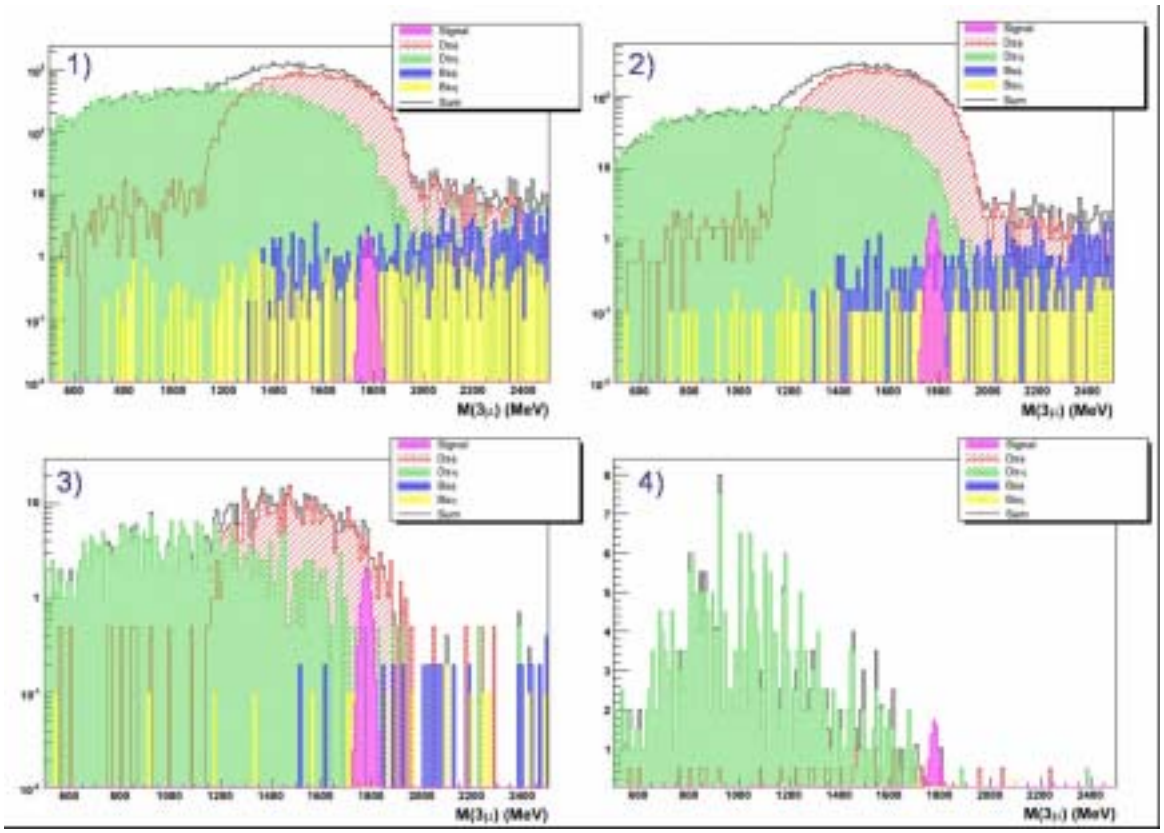

Figure 6.14: Three muon invariant mass for the signal and the four background processes at four steps of the analysis chain: 1) after trigger, 2) after isolation, 3) after the missing energy cut and 4) after the ϕ-veto.

6.3.2 Signal Modeling

The signal events have been generated with the PYTHIA generator using a phase space decay model.

To control the effect of a given dynamics on the p_t and η spectra on the final state muons event-weights related to a specific physical model has been included in the analysis. As reported in sect. 1.4.1, a large number of theories foreseen decays that violate the flavor number and thus also the production of three charged muon leptons by a τ lepton. In this section we refer only to the minimal supersymmetric extension of the standard model (MSSM). In this model the existence of a lagrangian term where the Higgs field can couple with two leptons of different flavor ($\tau \rightarrow H\mu$) gives rise to a non-zero Branching Ratio for the $\tau \rightarrow 3\mu$ decay. As illustrated in section 1.4.1, the MSSM foreseen branching ratios for the process under investigation of the order of 10^{-7}-10^{-8}, depending on the values of the model parameters. The parameterization of the BR($\tau \rightarrow 3\mu$) is reported in eq. 1.7. It depends on the values of $tan\beta$, on the mass of the Higgs boson and on two dimensionless function of the MSSM parameters, Δ_R and Δ_L.

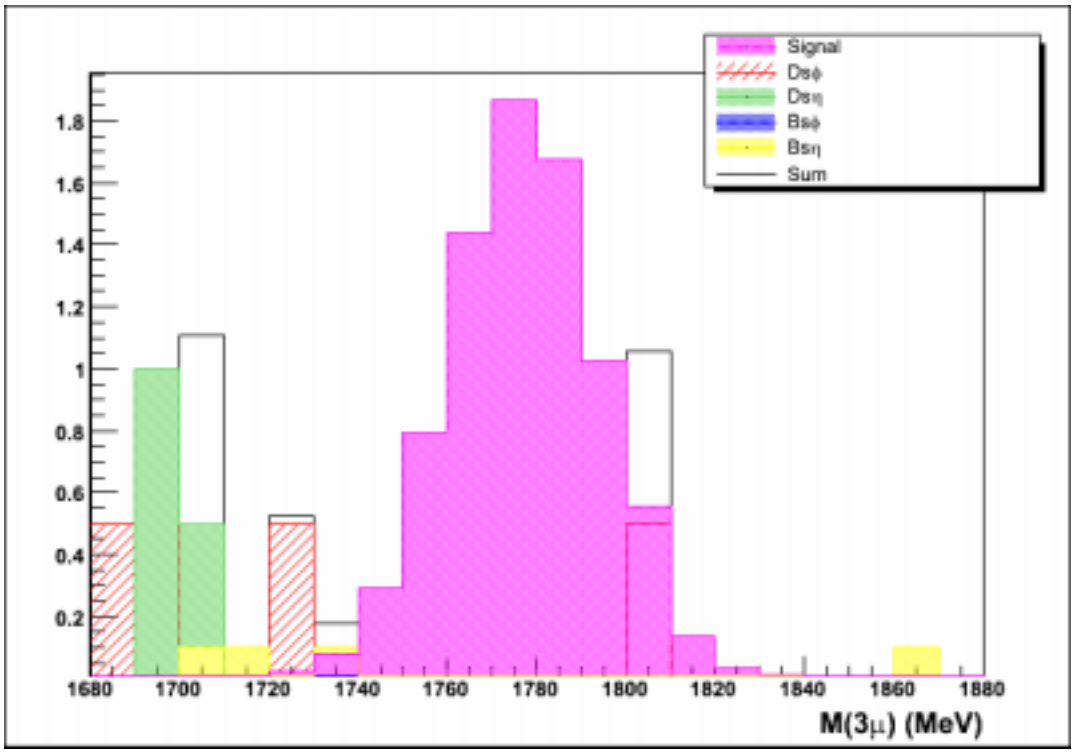

Figure 6.15: Three muon invariant mass for the signal and the background at the end of the selection.

To estimate the effect of modeling the decay mode, a simple code has been developed. We start from the energy values of two random final state muons, E_1, E_2, and perform a Lorentz boost to the τ center of mass system. The quantity $d\Gamma/dE_1^{CM}dE_2^{CM}$ is evaluated for each event using a parameterization of $\Gamma(E_1, E_2)$ obtained in the contest of the MSSM model. The relevant MSSM parameters has been fixed at the following values:

- $m_{A_0} = m_{H_0} = m_{h_0} = 100$ GeV;
- $tan\beta = 1.55$ ($\beta \simeq 50$);
- $\Delta_R = \Delta_L = 0.006$;

In Fig.6.16 the Dalitz plot for a three body decay is shown. The kinematic variables selected are the energy of the first and of the second muon, E_1, E_2. The case of a uniform phase space decay is shown in Fig. 6.16 (left), while that for a decay matrix with the matrix element of the MSSM model is shown in Fig. 6.16 (right). As expected, in the first plot the data density in the Dalitz plot is uniformly distributed within the kinematic limits. In the second plot instead, a much greater density is observed in the central region, or in other words in the region where two of the three decay products have the same energy. This is due to the presence of an intermediate heavy particle, the Higgs

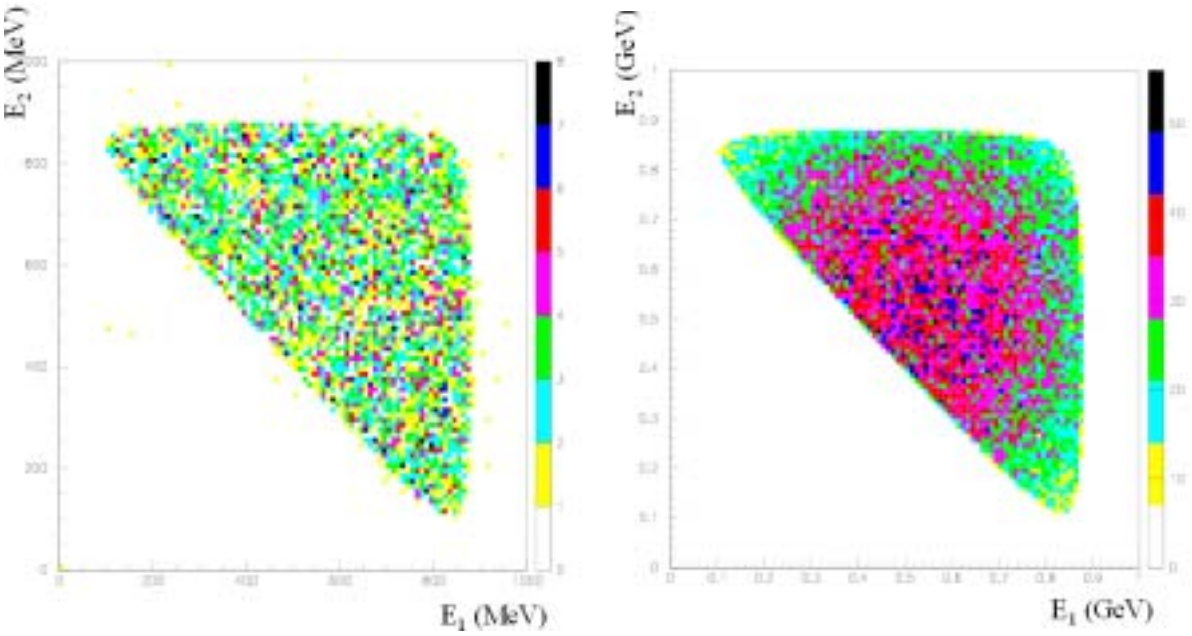

Figure 6.16: Dalitz plot for the three body decay $\tau \rightarrow 3\mu$ in the case of a phase space three body decay (left) and in the case of modelling with a MSSM matrix element (right).

boson, in the decay which changes the dynamic of the $\tau \rightarrow 3\mu$ decay. This could change in principle the global detection efficiency of the signal, i.e. the number of events surviving the selection cuts and their distribution.

In order to test this, each event generated with the uniform phase space has been weighted with the factor $d\Gamma/dE_1^{CM}dE_2^{CM}$, normalized to the mean Γ of the decay. Fig. 6.17 shows the distribution of the three muon invariant mass in the case of a uniform phase space three body decay and in the case of re-weighting the events with a model dependent factor. The plot shows that no appreciable effects exist, the global efficiency changes from 18.78% to 18.97%.

6.4 Upper Limit with the Atlfast simulation

After having estimated the number of expected background and the signal efficiency with the fast simulation, it is then possible to compute the upper limit on the signal branching ratio. The upper limit on the branching ratio is expressed by the following formula:

$$BR_{UL} = \frac{N_{UL}}{L \times \sigma(W) \times BR(W \rightarrow \tau\nu) \times \epsilon}, \tag{6.9}$$

where ϵ is the signal detection efficiency and N_{UL} is the upper limit on the number of

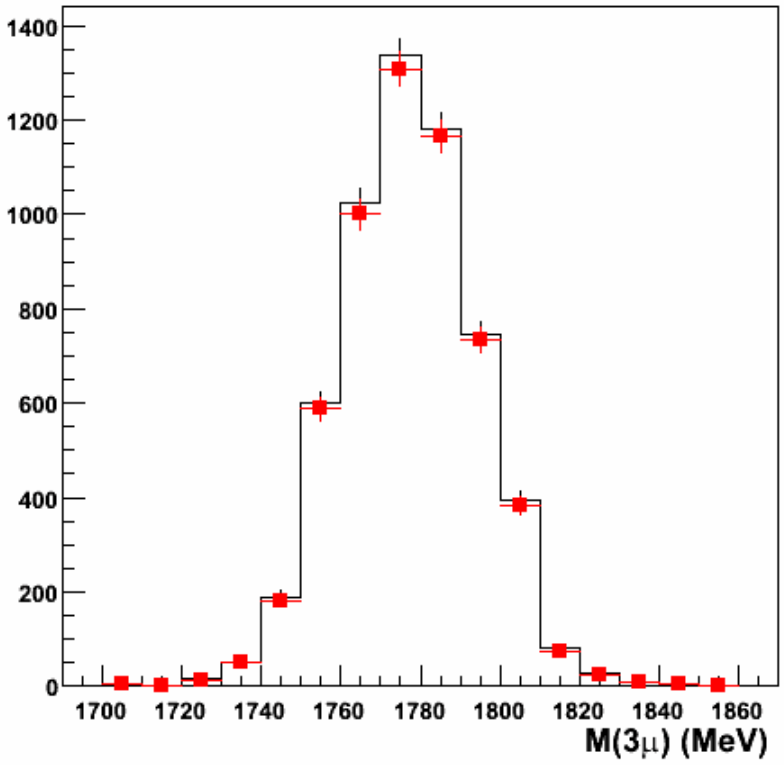

Figure 6.17: Three muon invariant mass distribution. Histogram is for the phase-space $\tau \rightarrow 3\mu$ decay, red points are for the decay weighted with a MSSM matrix element.

signal events when a certain number of background events and observed events, N_{bkg} and N_{obs}, are expected. In 10 fb^{-1} of integrated luminosity we estimate 0.6 background events. The upper limit is computed with the hypothesis to have N_{obs} = 0,1,2,3..., weighting it with a poissonian probability. The mean upper limit to the branching ratio is given by:

$$< BR_{UL} >= \sum_i BR_{ULi} P(N_{bkg}|i), \tag{6.10}$$

where i = N_{obs} = 0,1,2,3.... Using the Feldman and Cousins prescription[17], one N_{UL} is set corresponding to a given N_{obs}. The upper limit on the $\tau \rightarrow 3\mu$ branching ratio is then:

$$BR(\tau \rightarrow 3\mu)_{UL} = 7.8 \times 10^{-8} \quad at \quad 90\% \quad C.L. \tag{6.11}$$

and

$$BR(\tau \rightarrow 3\mu)_{UL} = 9.6 \times 10^{-8} \quad at \quad 95\% \quad C.L. \tag{6.12}$$

As reported in Par. 1.4.2, the upper limit on the $\tau \rightarrow 3\mu$ branching ratio has been set by the B-factories to the value 2×10^{-7} at 90% C.L.. This number has to be compared with

the result of eq. 6.8. The analysis done with the fast simulation indicates that, the Atlas detector can improve the present upper limit by a factor of 2, already using the first 10 fb^{-1} of integrated luminosity.

6.5 Full Simulation

In order to estimate the Atlas detector performances for the search of the $\tau \rightarrow 3\mu$ signal in a more realistic and complete way respect to the fast simulation, part of the generated events have been passed through Atlas the full simulation program. This allows to take into account detector effects, such as resolutions and geometrical acceptance as well as reconstruction efficiency. The complete simulation chain consists of:

- Detector simulation: it is the process whereby generated events are passed through GEANT4 Simulation of the Atlas detector to produce GEANT4 Hits, i.e. a record of where particle has traversed the detector and how much energy has been deposited.
- Response digitization: it is the process whereby the simulated GEANT4 Hits are passed through the response of the detector to produce Digits, such as charge, times and voltages, as produced in the Raw Data from the real detector. The digitization of GEANT4 hits in Atlas is performed subdetector-by-subdetector.
- Event reconstruction: it is the process whereby the raw data Digits are reconstructed into tracks and energy deposits as Event Summary Data (ESD), Analysis Object Data (AOD) or Combined NTtuples (CBNT).

Due to the complexity to follow the entire chain from the generated events to the reconstructed ones, not all the four background processes have been fully simulated. The result of the fast simulation is that the most dangerous background is the one from the decay of a D_s meson with the production of a ϕ resonance (the one representing the major source of background at the end of the selection chain). A statistic corresponding to 10 fb^{-1} has been fully simulated for this process. The other backgrounds will be fully simulated only when the performances of the reconstruction programs of the Atlas detector will be completely understood.

6.5.1 Muon Reconstruction algorithms

For the scope of this analysis we are particularly interested in the reconstruction of muons. When a charged particle moves through the Atlas detector it leaves a set of hits both in the Inner Detector and in the Muon Spectrometer. A hit provides information about the track parameters at the measured location. There are several sources of hits: tracks from the interactions in LHC, coming from different bunch crossing, as well as cosmic particles, electronic noise and radioactivity. The pattern recognition task is to properly associate hits to particle trajectories in order to find the full set of track parameters by searching for the best fit of a physically valid track. A muon is reconstructed separately in the inner tracker and in the muon system, information from the two sub-detectors are then combined in order to obtain the track parameters. Different reconstruction softwares are available within the Athena framework in order to individuate a muon and measure its momentum and direction. Here a list of the reconstruction programs that have been looked at for this work:

- **IPatRec**[46]
  It is a Foltran program used for reconstructing track in the Inner Detector. The general procedure is to form track-candidates using space-point combinatorial subject to criteria on maximum curvature and vertex region projectivity. Candidates undergo a track-fit procedure to give track parameters with covariance at the point of closest approach to the beam-line (perigee parameters). The track follower algorithm propagates these parameters to form an intersect with error ellipse at each silicon detector layer in turn. Accepted tracks are required to have at least 6 silicon clusters and a χ^2-fit probability greater than 0.001.

- **MuonBoy/STACO**
  Muonboy is a muon spectrometer "standalone" track reconstruction code. Muonboy includes segment pattern recognition at the MDT/CSC and trigger chamber level, global spectrometer track tracing through the B field, track fitting to extract the momentum, and back propagation to the interaction point. The sequence of reconstruction in Muonboy starts by identifying regions of activity. These regions are indicated by the trigger chambers (RPCs in the barrel and TGCs in the endcap). The hits in these active regions are combined into local segments via a pattern recognition algorithm. This algorithm employs some constraints to enhance speed and accuracy. For example segments are required to point roughly to the Interaction Point. The position and direction of segments provide a first rough estimate of momentum. Individual segments are then connected to segments in other stations via 3-dimensional continuous tracking in magnetic field. Several combination sequences are performed on multiple segments where the fits provide refined momentum estimates and track quality factors. If segments match, a candidate track is found. A candidate is confirmed if it can be backtracked to the interaction point.

  STACO (STAtistical COmbination) is a code which attempts to statistically merges the two independent measurements derived from the inner detector track (IPatRec) with the spectrometer track (MuonBoy) at the interaction point. The merging is done by combining the covariance matrices of the two tracks to obtain the benefit of two independent measurements.

- **MOORE/MuID**[47, 48]
  Muon Object Oriented REconstruction. It is a package for the reconstruction of the muon tracks in the Atlas Muon Spectrometer, developed in C++ in the Athena framework. The program starts from a search of the regions of activity within the detector and subsequently performs the pattern recognition and track fitting. The final reconstructed objects are tracks whose parameters are expressed at the first measured point inside the Muon Spectrometer. A very good reconstruction efficiency is expected for tracks with $p_t > 10$ GeV (about 95%) in the pseudorapidity range covered by the Muon Spectrometer.

  The package MuID (MUon IDentification) associates tracks found in the Muon Spectrometer with the corresponding Inner Detector tracks as well as with calorimeter

information by extrapolation of the MOORE track parameters to the vertex. The multiple scattering in the calorimeters is parametrized with a set of scattering planes: the energy loss is evaluated either from the calorimeters measurements or from a parameterization as a function of the muon momentum and pseudorapidity. The final objects are identified muons whose track parameters are given at the point of closest approach to the beam intersection. Unlike STACO which statistically merges the two independently found tracks, this code performs a global refit of all hits associated with these tracks.

- **MuIDLowPt**[49]
  A dedicated algorithm allows for the identification of low-p_t muons that lose a significant part of their energy in the calorimeters and thus do not have a corresponding track in the muon spectrometer. The inner detector tracks are extrapolated into the muon system and associated with segments or a series of hits in the spectrometer. All the muon spectrometer technologies are used, MDT and CSC chambers but also RPC and TGC chambers. Propagation through the solenoidal field is performed to obtain ϕ at the spectrometer entrance. A parameterization of the toroidal magnetic field effects is used to extrapolate η to the middle muon spectrometer station.

A large fraction of signal events have at least one muon with transverse momentum ranging from 3 to 6 GeV. Indeed, as shown in section 6.1, in the fast simulation, it was observed that in the $\tau \rightarrow 3\mu$ process about 55% of the events that pass the trigger cut have a third muon with 3 GeV $< p_t <$ 6 GeV. In this range of transverse momenta is often possible a muon can passing through the calorimeters will have not enough energy to pass through the three spectrometer stations. In particular, muons with p_t between 3 and 4 GeV will not have a corresponding track in the spectrometer, but they can anyway pass the calorimeters and reach the first spectrometer station. This muons are not reconstructed by the MOORE/MUID and MuonBoy/STACO algorithms but are instead individuated by the MuIDLowPt package.

Muons reconstructed by MuIDLowPt are flagged in such a way to keep the information if they were reconstructed as combination of an inner detector track and a muon spectrometer track (*combined muons*) or they are individuated as an inner detector track with an associated segment in the muon system (*low-p_t muons*). About 47% of the muons reconstructed from the $\tau \rightarrow 3\mu$ generated events and contained in the MuIDLowPt collection are identified as low-p_t muons.

In Fig.6.18 the reconstruction efficiency of the MuIDLowPt package is shown as a function of p_t and η of the muons. In Fig.6.19 the fraction of fake muons as a function of the muon transverse momentum and pseudorapidity is reported. From the plots a very high efficiency in the reconstruction of muons is observed also for very low values of the transverse momentum. The fraction of fake muons is negligible for truth muons with p_t $>$ 4 GeV (lower than 0.1%).

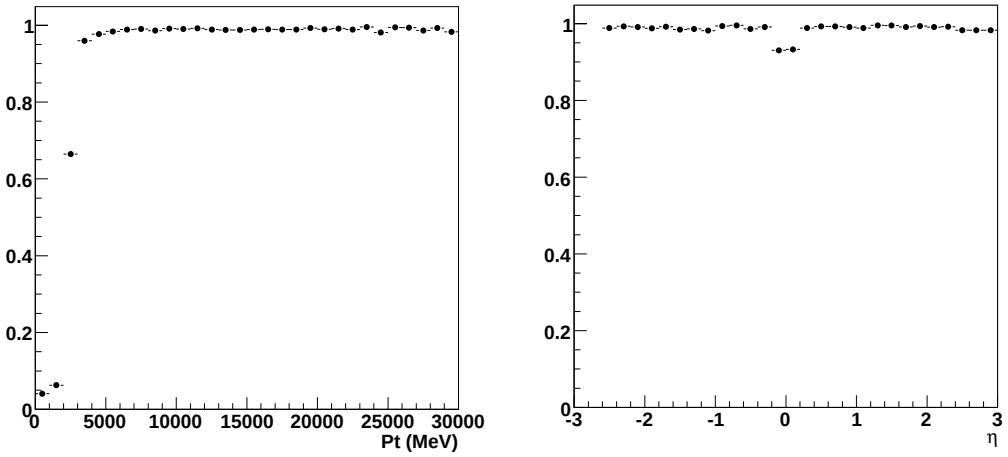

Figure 6.18: Reconstruction efficiency of the MuIDLowPt package on the signal events as a function of the muon p_t (left) and η (right). The efficiency as a function of η is plotted for muons with $p_t > 3$ GeV.

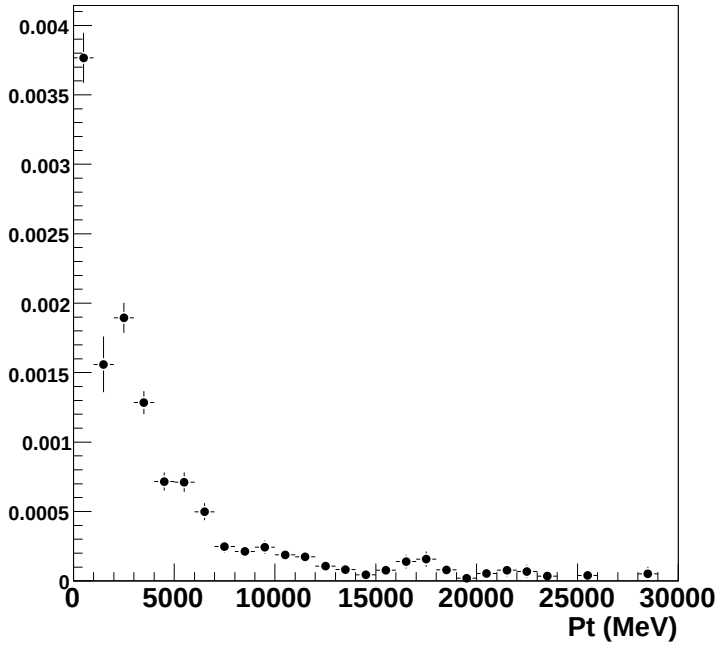

Figure 6.19: Fraction of fake muons reconstructed by the MuIDLowPt package as a function of the muon p_t.

6.5.2 Analysis of fully simulated events

In this section, we repeat on fully simulated events the analysis scheme tested with the fast simulation to study eventual reconstruction problems or differences in the counting due to the reconstruction efficiency of the different algorithms. As explained in the previous section in order to improve the efficiency at low p_t, we consider as muons the ones reconstructed by the MuIDLowPt which is based on track reconstructed in the ID in association with a series of hits or segment in the Muon Spectrometer.

Preselection

Also for this sample we apply on the reconstructed events a minimum cutoff to p_t and η, $p_t > 3$ GeV and $|\eta| < 2.5$, since it has been already applied in the background generation knowing that, in this case, the track efficiency will not be 100 % as assumed in the fast simulation. In particular, there will be a drop on counting in the momentum region between 3 and 5 GeV. As shown in Tab.6.2, the effect of preselection in this sample is much more hard on background that on the signal since the p_t spectrum is much softer.

Another important difference with respect to the fast simulation is the presence of fake tracks. Indeed the distribution of the number of muon candidates, for signal and background after the preselection, is shown in Fig.6.20. There is a reasonable contribution

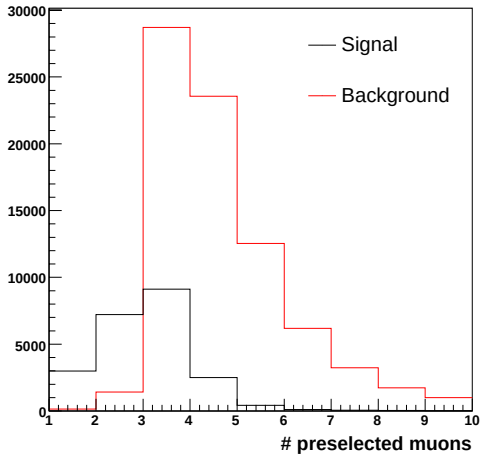

Figure 6.20: Number of muons per event after the preselection on p_t and η for the signal and the background.

of cases with more than three preselected muons. We restrict the analysis to the events with 3 or 4 preselected muons. By looking at the MonteCarlo truth, we found out that the best method to reduce the counting of fake tracks, in the signal sample, is to select the 3 tracks having the invariant mass closest to the τ mass.

Trigger

Similarly to what done in the fast simulation, the LVL1 trigger efficiency has been inserted manually. The muon LVL1 trigger efficiency curves, shown in Fig.6.8 for the barrel and for the endcaps, are fitted with an analytical function of the muon transverse momentum. The function obtained from the fit are used to weighed the events with the hit-or-miss method.

Isolation

The high background rejection power of requiring three isolated muons has been highlighted in the fast simulation analysis where the isolation criteria were based on the distance between the tracks and calorimeter clusters. In the full simulation, criteria based on the muon isolation with respect to other tracks is used.

For each muon, a loop on the tracks candidate of the inner detector is performed by searching for tracks close to the muon candidate. Other muon candidates are excluded from this counting. In Fig. 6.21 (left) the number of tracks with $p_t > 1$ GeV contained in a

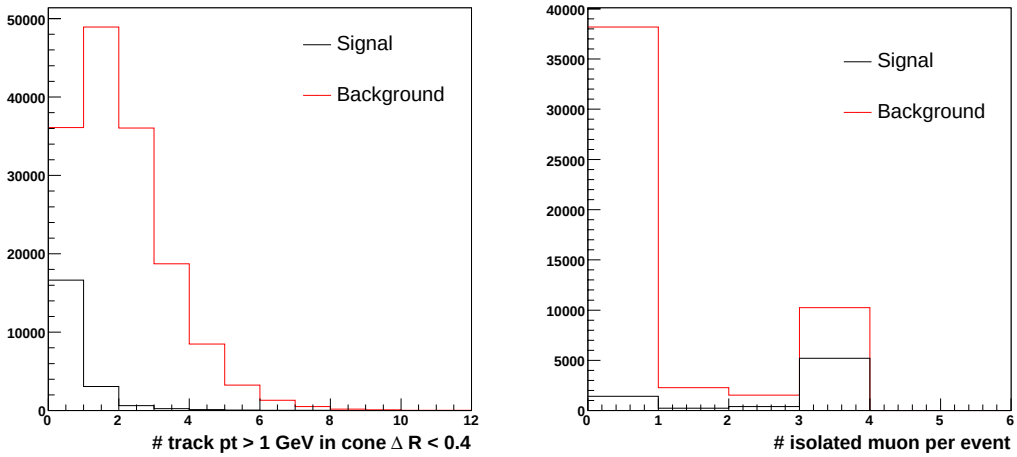

Figure 6.21: Left: number of tracks with $p_t > 1$ GeV contained in a cone of $\Delta R < 0.4$ around the muon direction. Right: number of isolated muons per event.

cone of $\Delta R < 0.4$ around each muon is shown for the signal and for the background. In the background, the muons are less isolated due to the tracks coming from the accompaning particles generated by the parton-shower of the c or b quark. A considerable amount of them have p_t of at least 1 GeV. We define an isolated muon the ones without any other tracks with $p_t > 1$ GeV in the surrounding cone. In Fig. 6.21 (right) the number of isolated muons per event, for the signal and for the background, is shown. From the plots it is evident that the requirement to have three isolated muon in the final state is very effective on the background rejection.

The efficiency of the isolation cut is 18% for the background and 73% for the signal.

Missing Energy

The signal events are characterized by a large amount of transverse missing energy due to the presence of a neutrino from the $W \rightarrow \tau\nu$ decay. The fast simulation study has shown that a cut on the missing transverse energy is very powerful in rejecting the backgrounds, thus it is important to make this variable working on the fully simulated events.

The total missing transverse energy is computed as the sum of three contributions:

$$E_T^{miss} = E_{T(Calo)}^{miss} + E_{T(Cryo)}^{miss} + E_{T(muon)}^{miss}, \tag{6.13}$$

where E_T is $\sqrt{(P_X^{miss})^2 + (P_Y^{miss})^2}$ and each single component is the sum of the energy on all calorimeter cells, treated as momentum sum, by weighting each cell for its angular position as follow: $P_x^{miss} = -\sum_i E^i sin(\theta_i)cos(\phi_i)$, $P_y^{miss} = -\sum_i E^i sin(\theta_i)sin(\phi_i)$. The different terms in eq. 6.13, are the contribution due to the calorimeter cells, the correction term to take into account the energy loss in the cryostat and the correction for the muon loss. This last term depends on the fact that the muon energy deposition in the calorimeters is not linear with muon momentum but is limited to the energy loss due to the minimum ionization. This loss is distributed following a landau curve with a peak which is set to 3 GeV ($P_{\mu loss}$) in the barrel at 90°. This loss is proportional to the calorimeter thickness and therefore scales down as $1/sin(\theta)$.

The standard muon correction is calculated starting from the muons reconstructed with MuID, i.e. the ones reconstructed both in the inner tracker and in the muon spectrometer. As shown in section 1.5.1, there is a large amount of events, $\simeq 50\%$, in which a muon does not have a corresponding track in the Muon Spectrometer. For this reason, the missing transverse energy computed by the full reconstruction program is underestimated. To correct this technical problem, we have subtracted the contribution $E_{T(Muon)}^{miss}$ as computed by the standard reconstruction and add a new term that takes into account also the low-p_t muons individuated by MuIDLowPt. For each muon in the event the quantity:

$$E_T^{correction} = \sqrt{(P_x^{miss})^2 + (P_y^{miss})^2} \tag{6.14}$$

where

$$P_{x(y)}^{miss} = P_{x(y)}^{full} - P_{x(y)}^{muon} + P_{x(y)}^{correction} \tag{6.15}$$

is computed. Here the correction of the missing energy components are given by:

$$P_{x(y)}^{correction} = \sum_i (|P| - |P_{\mu loss}(\theta)|)sin(\theta)cos(\phi). \tag{6.16}$$

In Fig.6.22 the E_T^{miss} distribution is shown for the signal and for the background before (left) and after (right) the correction. After correction, the distribution for the signal is again peaked at 40 GeV while the distribution for the background is peaked at very low transverse missing energy values. A cut is applied asking $E_T^{miss} > 20$ GeV, as in the fast simulation analysis. About 92% of the signal events survive the cut against 6% of background events.

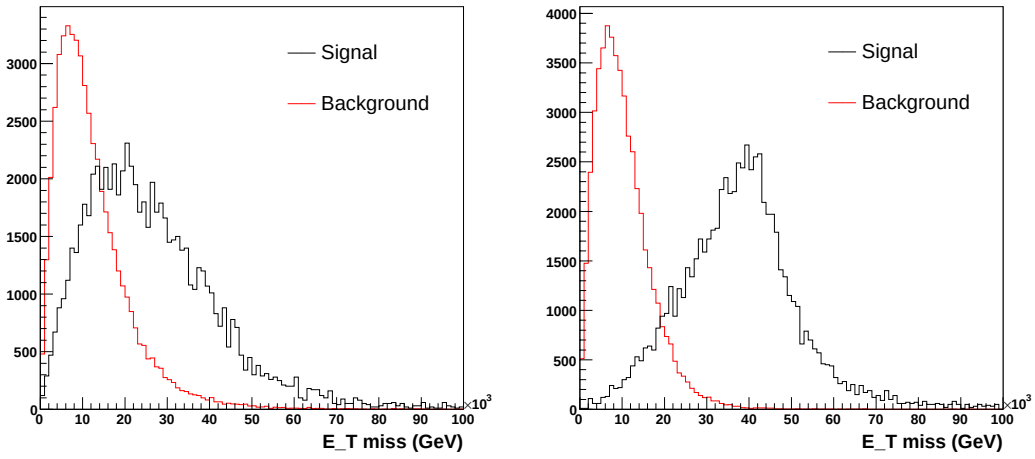

Figure 6.22: Left: missing transverse energy distribution for the signal (black) and the background (red) as is computed in the full simulation. Right: same distributions including the contribution from low-p_t muons.

ϕ-veto

The only background reconstructed with the full simulation is the decay chain $D_sX \to \phi\mu\nu X$ with $\phi \to \mu\mu$ since, as it is emerged from the fast simulation, this process gives the greatest contribution to the signal backgrounds at the end of the selection. Also in this case, we apply a veto on these events by reconstructing the ϕ mass with the quantity $M_{closest}$. This is done by searching the muon pair with a total charge null sign and with the closest invariant mass to the ϕ mass. The distribution of $M_{closest}$ is shown in Fig.6.23. From the plot is evident that the distribution is larger than the one obtained from the fast simulation, Fig.6.12. Fitting it with a gaussian function leads to the following values:

$$< M_{closest} >= (1021.92 \pm 0.24) \;\; MeV \tag{6.17}$$

$$\sigma(M_{closest}) = (17.17 \pm 0.22) \;\; MeV. \tag{6.18}$$

These values have to be compared with the ones found with the fast simulation program: $<M_{closest}>$ = (1019.76 $\pm$ 0.07) MeV and $\sigma(M_{closest})$ = (9.81 $\pm$ 0.06) MeV; a worsening of almost a factor 2 in the mass resolution is observed. This effect is not uniform on all the detector acceptance but is more pronounced at large pseudorapidity values. In Fig.6.24 the width of the distribution $M_{closest}$ is shown after having divided the η range of the muon pair in five intervals.

In the plot the η dependence of the mass resolution is shown both for the events having two combined muons and for events having muons from low-p_t algorithm. No differences are visible in the mass resolution between the invariant masses of two combined muons and the ones of two low-p_t muons. Indeed, as expected, given the low momentum of the tracks in this sample ($p_t < 30$ GeV), the dominant contribution to the resolution is given

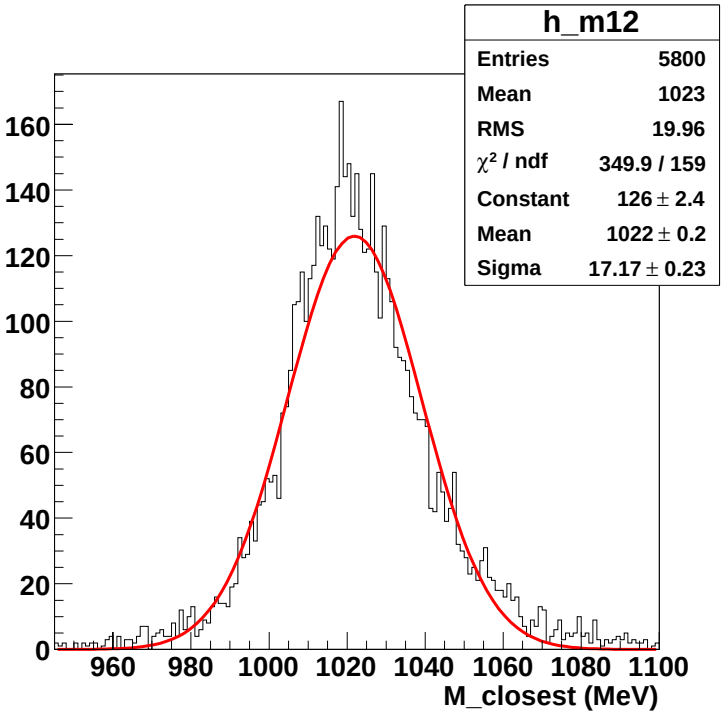

Figure 6.23: Distribution of the invariant mass of the couple of muons with invariant mass closest to the ϕ mass.

by the inner detector. We also show in red the same resolution as estimated by the fast simulation. In this case the η dependence is almost negligible.

In order to reject the background events while not reducing too much the signal efficiency, a cut on $M_{closest}$ which takes into account the variation of $\sigma(M_{closest})$ as a function of the muon η, has been applied.

We reject the events having $M_{closest}$ in within this range:

$$|M_{ij} - < M_{closest} > | < 3 \times \sigma(M_{closest}), \tag{6.19}$$

with $< M_{closest} >$ and $\sigma(M_{closest})$ depending on the muon pseudorapidity. This translates in a deterioration of the signal efficiency with respect to the what obtained with the fast simulation. Indeed 70% of the signal events passes the ϕ-veto cut against the 86% found in the fast simulation.

τ-window

After the cut on the $M_{closest}$ variable, we have only to count how many events have three muons with invariant mass, $M_{3\mu}$, close to the τ mass.

In Fig.6.25, the $M_{3\mu}$ distribution for the signal is shown for events surviving the trigger requirement. While for the fast simulation a width of 16.14 MeV was found, in the case

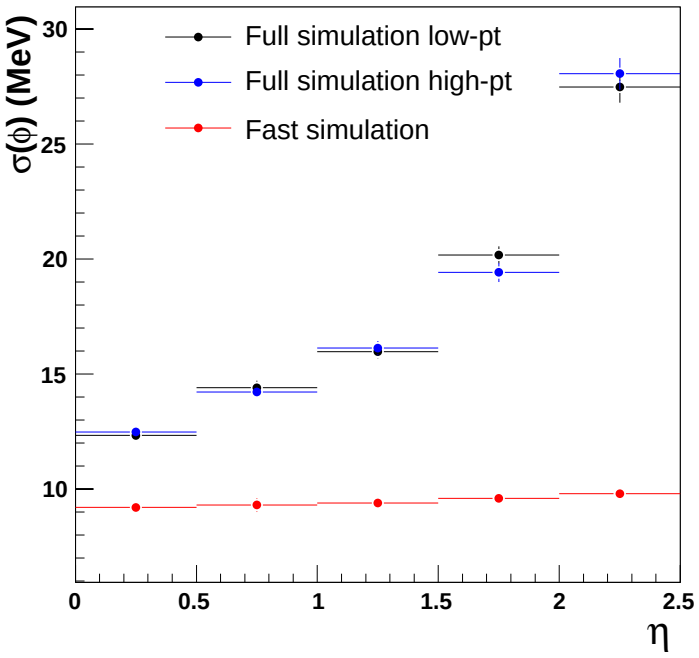

Figure 6.24: Width of the $M_{closest}$ distribution as a function of the muon pseudorapidity. The black and blue points refer to the mass computed with combined and low-pt muons respectively. The red point are the ones obtained with the fast simulation.

of the full simulation the width becomes 29.3 MeV. As for the $M_{closest}$ distribution, a deterioration of the mass resolution at large values of the muon pseudorapidity is observed and the mass-window used to count events has therefore to take into account this η dependence.

In Fig.6.26 the width of the $M_{3\mu}$ distribution is shown as a function of the pseudorapidity of the muons for the fast (red points) and for the full (black points) simulation programs. We accept events only if $M_{3\mu}$ is within $3\times\sigma(M_{3\mu})$ from M_{τ}.

6.5.3 Final events counting and comparison with fast simulation

In Tab. 6.3 the number of events for the signal and for the $D_s\phi$ background are reported at the various steps of the analysis chain. At the end of the selection no background events are counted, while the signal efficiency is lower than the one found with the fast simulation. The global signal efficiency in the full simulation is (13.7 $\pm$ 0.3)% versus (18.78 $\pm$ 0.39)% obtained with the fast simulation.

In Tab. 6.4 the numbers of signal events at the various steps are reported for the analysis performed with the fast and with the full simulation. In the same table, the efficiency of each single cuts applied are also shown in order to compare, step by step, the

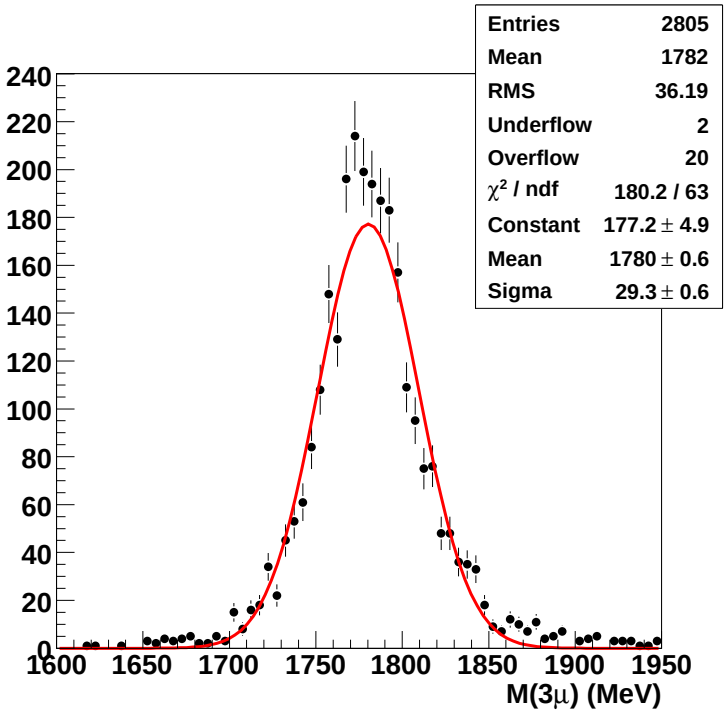

Figure 6.25: Three muon invariant mass distribution for events that survive the trigger requirement.

	Signal	$D_s\phi$ (10fb^{-1})
Generated	20000	80000
Reconstructed	7263	52262
Trigger	6217	31673
Isolation	4559	5748
Missing Energy	4122	344
ΔR	4005	289
ϕ-veto	2805	5
τ-window	2736	0

Table 6.3: Analysis chain with the fully simulated events.

two analysis.

Both for the signal and for the background there is a difference with respect to the fast simulation for the preselection cut. This is due in part to the reconstruction inefficiency that is not taken into account in the fast simulation and in part to the presence of the fake tracks in the full simulation. Indeed preselection for the full simulation asks for three or four muons with $p_t > 3$ GeV and $|\eta| < 2.5$. For the events with four preselected muons

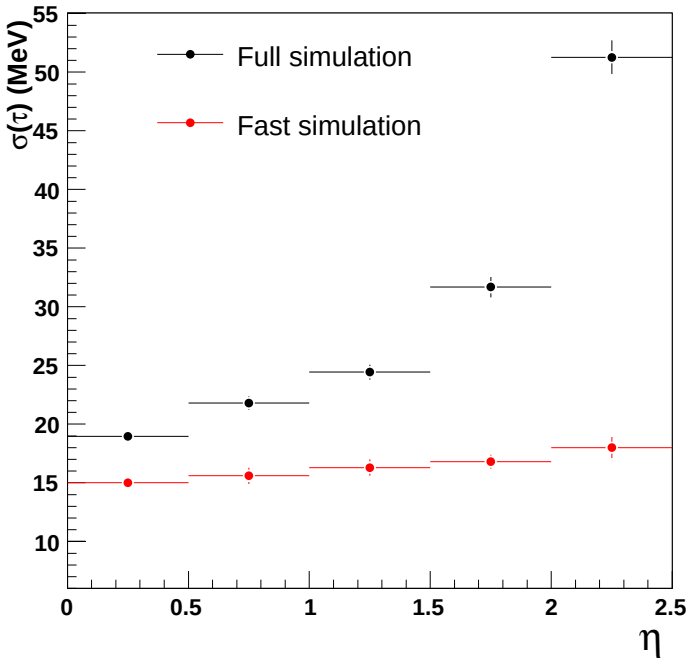

Figure 6.26: Width of the $M_{3\mu}$ distribution as a function of the muon pseudorapidity for the fast (red) and for the full (black) simulation.

we select the three candidate muons from τ by searching the three muon combination with invariant mass closest to the τ mass (see section 6.5.2). Moreover the background shows a bigger loss than the signal in the preselection due to its real softer p_t spectrum.

The isolation shows also some differences and it is much harder in full than in fast simulation but the recipe is slightly different and this is acceptable. Work is in progress to compute the also the calorimetric isolation of muons.

The requirement to have a missing transverse energy greater than 20 GeV in the event and the requirement to have three almost collinear muons, show a very good agreement between the fast and the full simulation.

The largest difference observed however comes from the $|\eta|$ dependence of the mass resolution which almost completely accounts for the efficiency loss. In the following paragraph, the studies done up to now to investigate this $|\eta|$ dependence are summarized. We will then conclude with the determination of the U.L. on the signal branching ratio with the full simulation.

	Fast Sim.	Full Sim.
Starting Events	20000	20000
Reconstructed	6410 (32%)	7263 (36%)
Trigger	5888 (29%)	6217 (31%)
Isolation	5192 (88%)	4559 (73%)
Missing Energy	4655 (90%)	4122 (92%)
ΔR	4378 (94%)	4005 (95%)
ϕ-veto	3787 (86%)	2805 (70%)
τ-window	3756 (99%)	2736 (97%)
Total Efficiency	18.8%	13.7%

Table 6.4: Comparison of the number of events that passes the selection chain for the fast and the full simulation.

6.5.4 Study of the resolution

In order to study the mass resolution we have taken into consideration two different points both for fully simulated and fast simulated events.

- Dependence on τ vertex position;
- Comparison of single track resolutions as a function of the muon η.

First of all the τ vertex position with respect to the interaction point has been controlled. In Fig. 6.27 (left) the distribution of R_{vtx} for the τ from the MonteCarlo truth is shown in black; the red histogram is the one obtained plotting for each single muon candidate the impact parameter, obtained as $R_0 = \sqrt{D_0^2 + Z_0^2}$. The inclusive distributions look reasonable although these two variables are not nicely correlated. Indeed, we still need to analyze the reconstruction of the secondary vertexes which surely have a much better resolution than the single track impact parameters. The distribution of $c\tau$ after correcting R_{vtx} for the $\beta\gamma$ of the τ has been checked. The distribution of $c\tau$, shown in Fig. 6.27 (right), has been fitted with an exponential giving a number of lifetime very close to the one of the PDG for the τ, $c\tau(\tau) = 87\mu m$. As it can be observed, depending on its $\beta\gamma$ the τ can decay also 2-3 cm far away from the interaction point. We have calculated the mass resolution in five different bins of R_{vtx}. Distribution of the three muon invariant mass are shown in Fig.6.28 for the five bins of increasing distance of the vertex from the interaction point. The resulting behavior of the mass resolution with respect to the τ vertex position is shown in Fig.6.28.

Similar exercise has been done for the main background looking at the vertex-dependence of M_ϕ, Fig.6.29, where in this case the decay vertex is the one of the D_s.

Looking at the behavior of the mass resolution as a function of the vertex position, it can be concluded that all events with a vertex closer than 1 mm to the interaction point have mass resolution in agreement with the one obtained with the fast simulation within

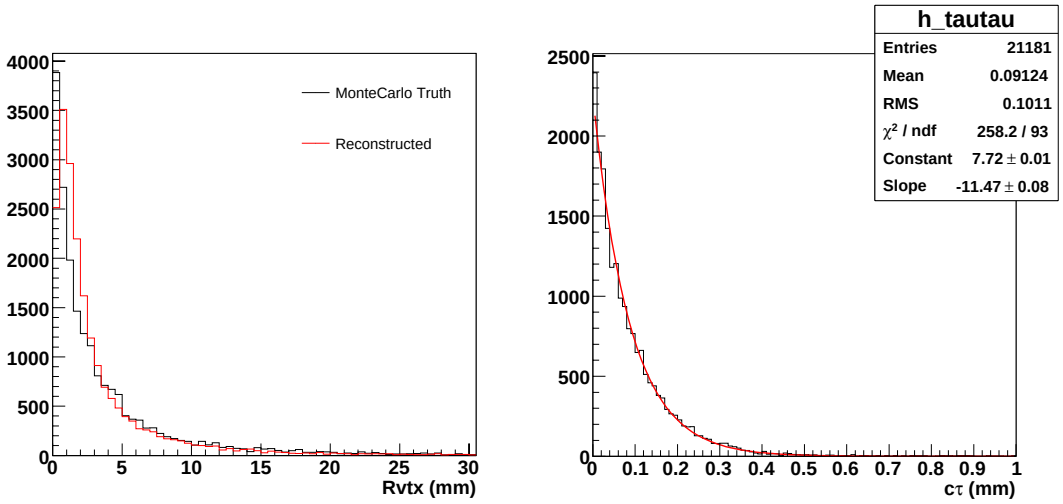

Figure 6.27: Left: The black histogram is the $\tau \to 3\mu$ vertex position from the MonteCarlo truth. The red histogram is the distribution of $R_0 = \sqrt{D_0^2 + Z_0^2}$ for each muon coming from the τ from the reconstructed events. Right: τ lifetime.

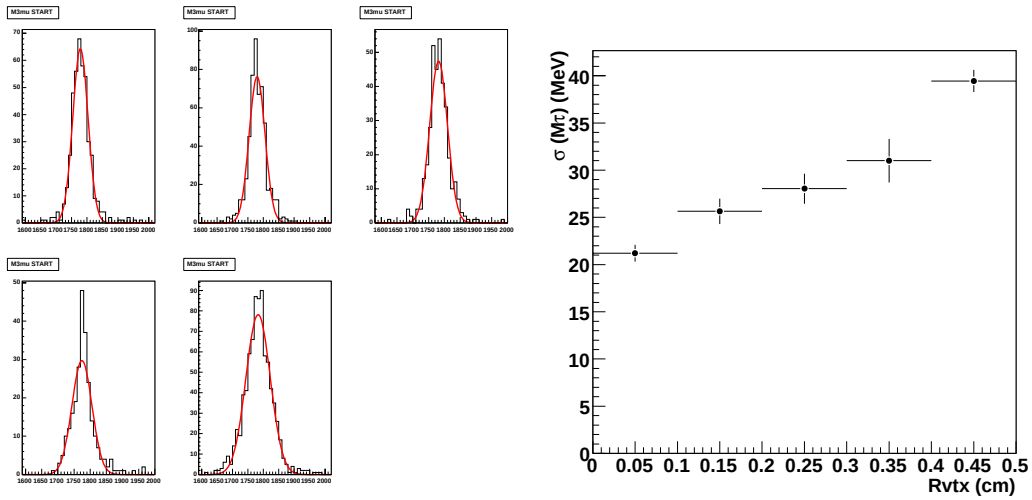

Figure 6.28: Left: three muon invariant mass for five bins of the vertex position of the tracks used to compute it. Right: Width of the three muon invariant mass distribution as a function of the τ vertex position.

10-20%. On the other hand, for events with vertex far from the interaction point the mass resolution of the full simulation can be greater than the one from the fast simulation by a factor 2.

In order to understand the observed dependence on η of the mass resolution, the single track momentum, $\sigma(1/p_t)$, and angular, $\sigma(cot\theta)$ and $\sigma(\phi)$, resolutions have also been studied. In Fig.6.30 the three resolutions are shown as a function of the pseudorapidity

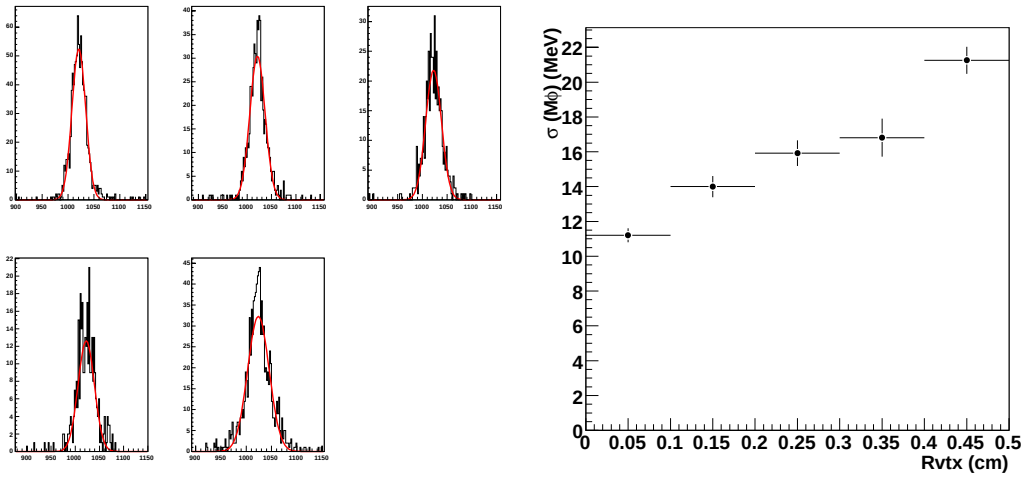

Figure 6.29: Width of the $M_{closest}$ distribution for the background as a function of the D_s vertex position.

for all the tracks with a p_t below 6 GeV. In Fig.6.31 the same resolutions for muons with $p_t > 6$ GeV are shown.

The resolution found, and their dependence on the muon pseudorapidity, are in good agreement with the ones reported in the Technical Design Report of the Inner Detector in the case of no vertex constraint applied [50]. Indeed the parameterizations of the various resolutions as a function of p_t and θ are given by the following formulas:

$$\frac{\sigma(p_t)}{p_t^2} = 0.36 \oplus \frac{13}{p_t\sqrt{sin\theta}} \quad (TeV^{-1}); \tag{6.20}$$

$$\sigma(cot(\theta)) = 0.70 \oplus \frac{2.0 \times 10^{-3}}{p_t\sqrt{sin^3\theta}}; \tag{6.21}$$

$$\sigma(\phi) = 0.075 \oplus \frac{1.8}{p_t\sqrt{sin\theta}} \quad (mrad); \tag{6.22}$$

The single track momentum and angular resolutions have been computed also for the events reconstructed with the fast simulation. They are shown in Fig.6.32 and 6.33 in the case of muons with p_t below or above 6 GeV respectively.

The resolutions found with the fast simulation are not in agreement with the ones obtained with the full simulation apart from the one on $\sigma(cot\theta)$ which is similar both in the fast and in the full simulation showing also the right η dependence. The resolutions on $\sigma(p_t)/p_t^2$ and $\sigma(\phi)$ show negligible η dependence in contrast with full simulation and TDR.

Concluding, although not everything is clear we have done some relevant observations on the mass and momentum resolution. In the full simulation a strong dependence of the mass resolution on muon pseudorapidity is observed in contrast with the fast resolution. In particular the full simulation have single track resolutions much more in agreement

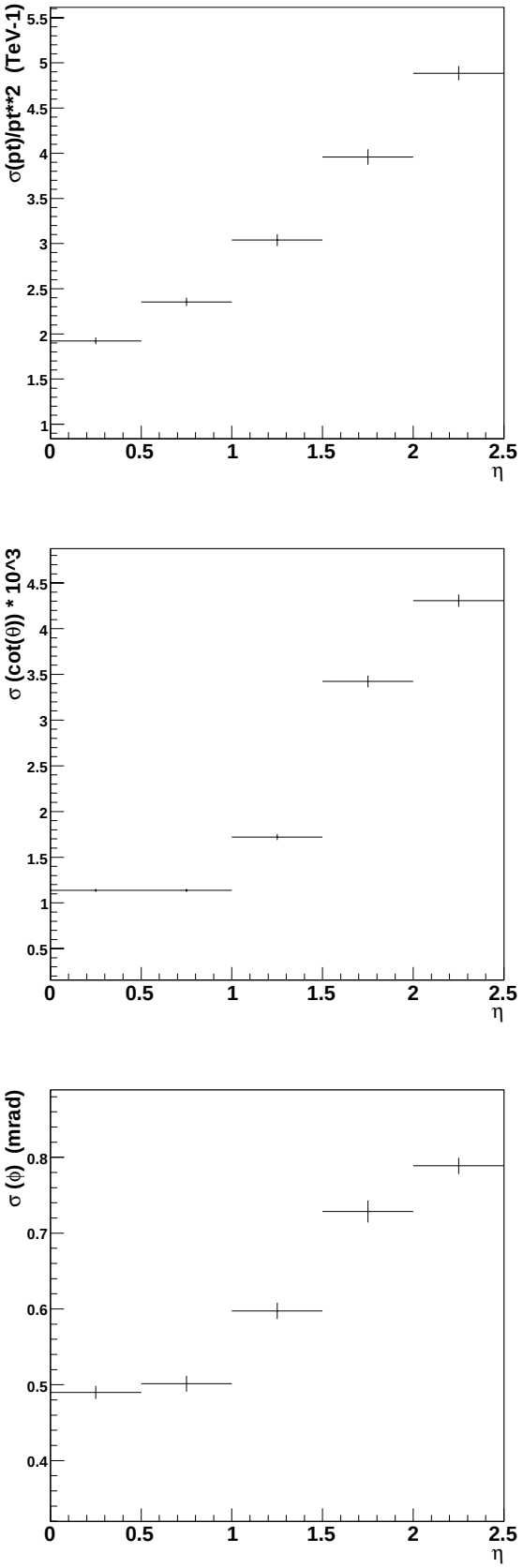

Figure 6.30: Single track resolutions ($\sigma(p_t)/p_t^2$, $\sigma(cot\theta)$ and $\sigma(\phi)$) as a function on the track pseudorapidity for muons with $p_t < 6$ GeV of the full simulation.

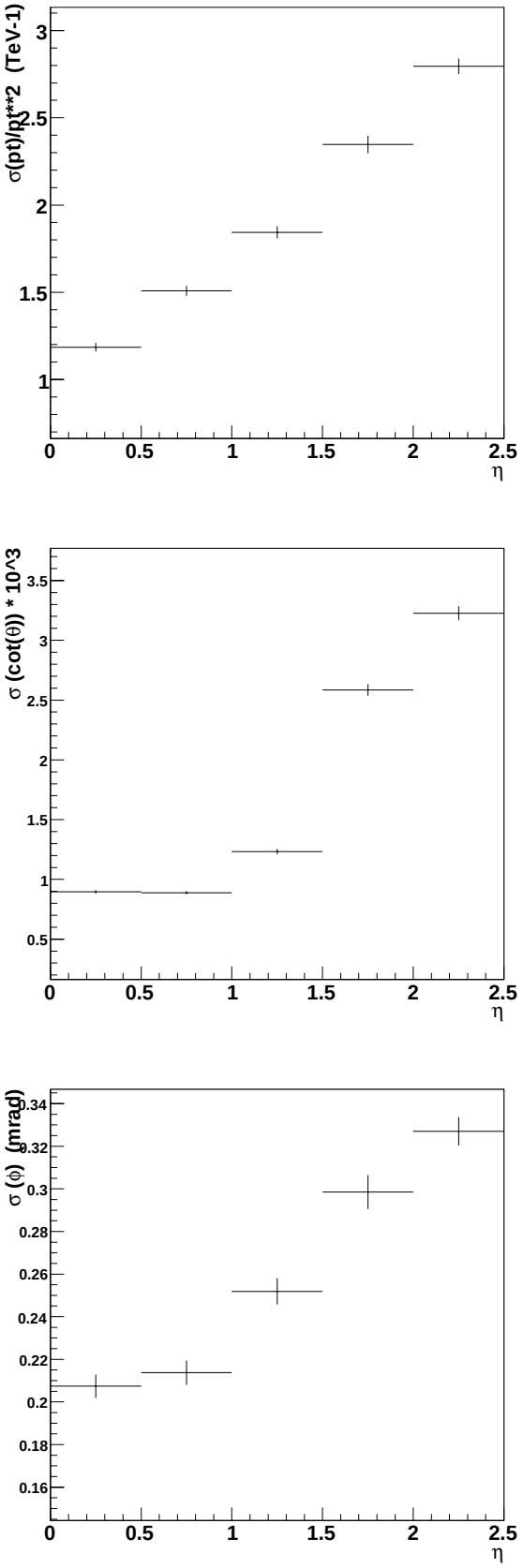

Figure 6.31: Single track resolutions ($\sigma(p_t)/p_t^2$, $\sigma(cot\theta)$ and $\sigma(\phi)$) as a function on the track pseudorapidity for muons with $p_t > 6$ GeV of the full simulation.

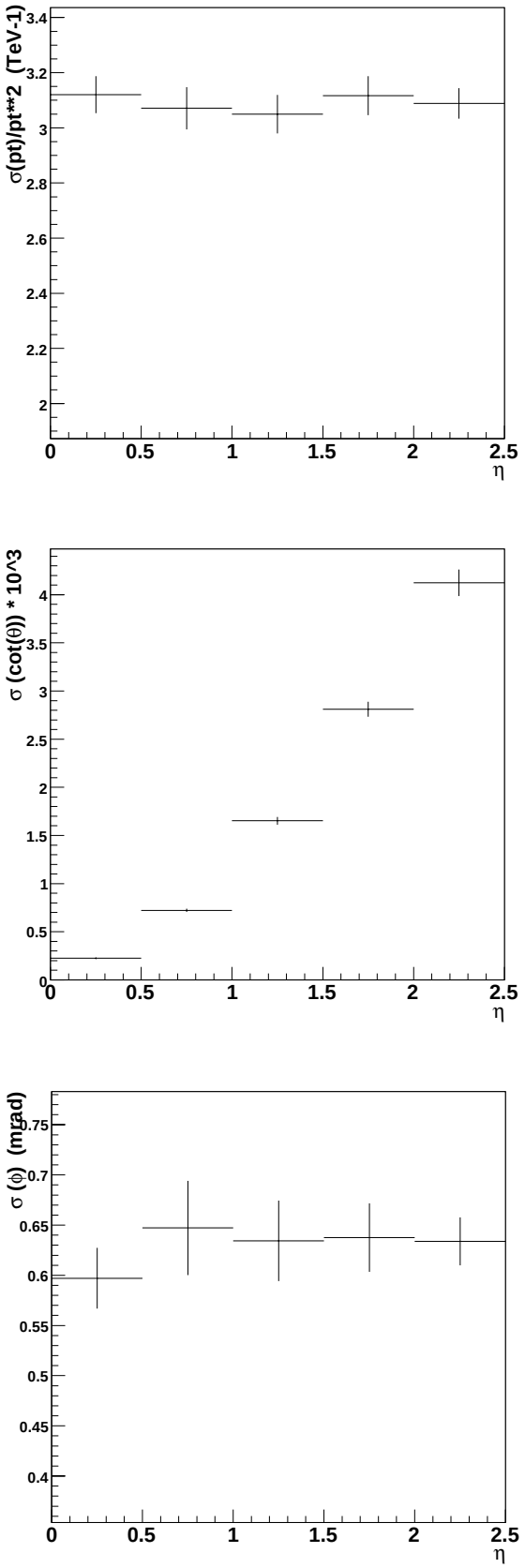

Figure 6.32: Single track resolutions ($\sigma(p_t)/p_t^2$, $\sigma(cot\theta)$ and $\sigma(\phi)$) as a function on the track pseudorapidity for muons with $p_t < 6$ GeV of the fast simulation.

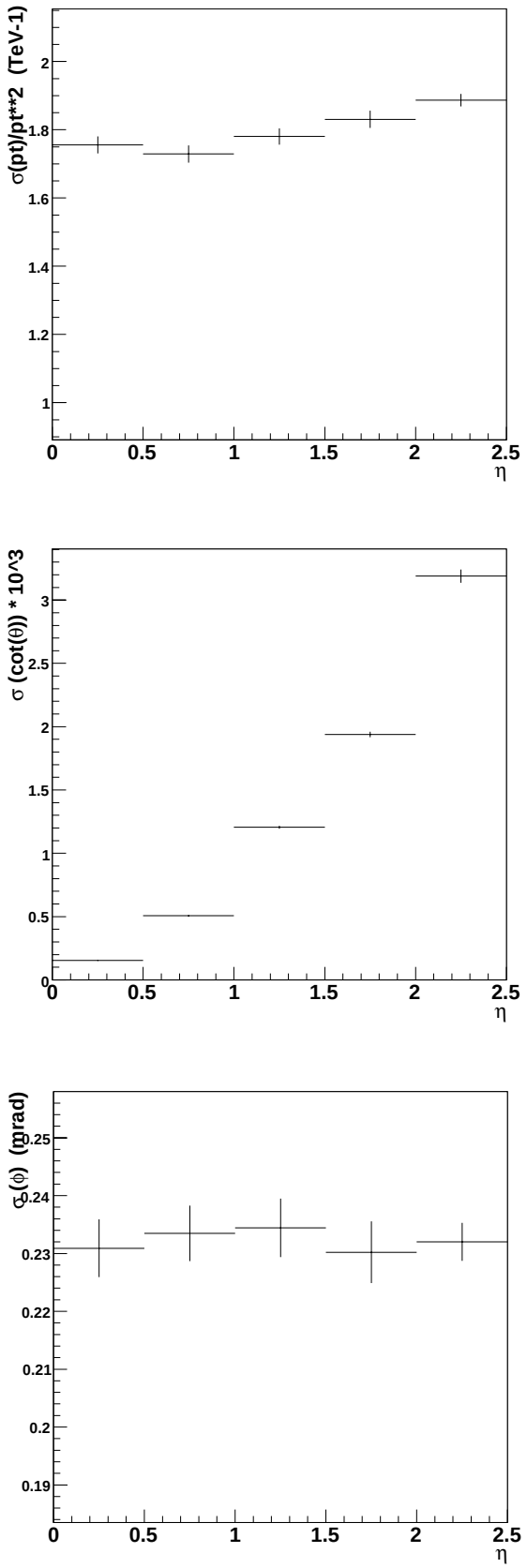

Figure 6.33: Single track resolutions ($\sigma(p_t)/p_t^2$, $\sigma(cot\theta)$ and $\sigma(\phi)$) as a function on the track pseudorapidity for muons with $p_t > 6$ GeV of the fast simulation.

with the TDR with respect to what found in the fast simulation. In particular, in the fast simulation there is not any η dependence of the resolution which is instead expected for a solenoidal tracker.

However, the fact that there is an improvement on mass resolution when cutting on the vertex, still leaves open the possibility to improve the resolution by constraining the tracks at the decay vertex. Following TDR the only variable which can still improve with vertex constraining is on ϕ. Work is in progress to use secondary vertex reconstruction and vertex-constrained tracks.

6.5.5 Determination of the UL for the full simulation

Although there are still open questions on the mass resolution, the study with the full simulation is stable enough to allow the estimation of U.L. on the $\tau \rightarrow 3\mu$ decay branching ratio using the values of number of background events found and signal detection efficiency.

We recall again the formula for the U.L.:

$$BR_{UL} = \frac{N_{UL}}{L \times \sigma(W) \times BR(W \rightarrow \tau\nu) \times \epsilon} \tag{6.23}$$

where N_{UL} is the upper limit on the number of signal events when a certain number of background events, N_{bgd}, are observed. In 10 fb^{-1} of integrated luminosity no background events are expected. With this number, using the Feldman and Cousins prescription[17], N_{UL} is 2.44 at 90% confidence level (C.L.) and 3.09 at 95% C.L.. The upper limit on the $\tau \rightarrow 3\mu$ branching ratio is thus:

$$BR(\tau \rightarrow 3\mu)_{UL} = 8.7 \times 10^{-8} \quad at \quad 90\% \quad C.L. \tag{6.24}$$

and

$$BR(\tau \rightarrow 3\mu)_{UL} = 1.1 \times 10^{-7} \quad at \quad 95\% \quad C.L. \tag{6.25}$$

We still see a factor 2 of improvement on the upper limit with respect to the result of the B-Factories already in 10 fb^{-1} of integrated luminosity.

Conclusions

The Monitored Drift Tube chambers will be used as precision tracking detectors in the Muon Spectrometer of the Atlas experiment. Extensive tests on these detectors have been performed in the last few years, to study all the different aspects of the chamber performances such as spatial resolution, tube efficiency and electronic noise rate. In this work, many of these studies on the MDT's chambers have been described.

In particular, a very important step in the understanding of the MDT properties has been done at the test beam carried out at the H8 beam line of the SPS in the summer 2004. The H8 setup was composed by a complete slice of the Atlas detector, including inner detector, calorimeters and muon system. Beams of different particles at different energies were available. Moreover, it was possible to measure the beam momentum, since a magnetic field was positioned in the muon system. In this thesis, the analysis performed on the data collected at H8 with the MDT chambers of the barrel has been presented. The resolution in the measurement of the muon sagitta has been measured by analyzing data collected with beams of muons with nominal momentum ranging from 100 GeV to 250 GeV. The obtained results show that the muon system is able to measure the muon sagitta with a resolution of 50μm in the high p_t range, where the contribution of the multiple scattering becomes negligible.

Other important tests of the MDT functionality are the one performed at the cosmic ray (CR) facility at BB5 (CERN). The CR stand represents the last step in the certification procedure that each chamber, of the middle and outer stations of the barrel muon spectrometer, has to pass before being installed in the Atlas cavern. At BB5 many aspects of an MDT chamber are controlled. The absolute pressure of the gas mixture and the percentage of the single elements are monitored. Dead or noisy channels are individuated and reported on the MDT database. Existing electronic problems are repaired. The drift properties of the tubes are investigated with the cosmic data by looking at the TDC and ADC spectra of each tube in the chambers.

In October 2005, few chambers were installed in final position in sector 13 of the Muon Spectrometer and then connected to temporary services. Checks of the electronic noise

level in the final environment were carried out. Moreover, more chambers were acquired from the DAQ control room to test the transportation of signals via optical fibers. First cosmic rays have also been acquired in the cavern by using a trigger based on scintillators counters. Results on the analysis of these first cosmic rays runs in the Atlas cavern have been presented.

In the last part of this thesis, the study of the Atlas sensitivity for the Lepton Flavor Violating decay of the τ lepton in three muons has been shown. The strategy to select this signal with the Atlas detector has been studied to obtain the highest possible detection efficiency while keeping under control the background. The cleanest signal production chain is the one with a W boson decay $W \rightarrow \tau\nu$. The largest source of background is instead constituted by the production of heavy mesons, D and B, with subsequent production of light mesons as ϕ and η. The most dangerous background sources have been studied, showing that a good rejection power is achievable. The key-points for the improvement of the signal to background ratio have been identified in the missing E_t, isolation of muons, distance between tracks and momentum resolution.

With the fast simulation program of Atlas, it has been shown that the upper limit on the signal branching ratio can be decreased by a factor 4 with respect to the present limit set by the B-factories, already using 10 fb^{-1} of integrated luminosity. Summarizing, our study indicated that with 10 fb^{-1} we can set an upper limit in the BR($\tau \rightarrow 3\mu$) of 6×10^{-8} at 90% C.L.

The study with the full simulation indicates that we are able to repeat the analysis steps as in the fast simulation with the exception of the momentum resolution. We have investigated this point and find out that the full simulation gives track resolutions in agreement with the ones expected for the inner tracker without constraining the track to the secondary vertex. Instead the fast simulation assumes a vertex constraining of tracks. Work is in progress to apply also the fit constraint procedure to events of the full simulation. However the U.L. on the signal branching ratio found with the full simulation has been computed and set to 8.7×10^{-8} at 90% C.L..

Bibliography

[1] "The Large Hadron Collider Conceptual Design", LHC CERN-AC-95-05;

[2] "Search for the Standard Model Higgs boson at Lep", CERN-EP/2001-055;

[3] Y. Fukuda et al., Super-Kamiokande collaboration, Phys. Lett. B433 (1998) 9; Phys. Lett. B436 (1998) 33; Phys. Rev. Lett. 81 (1998) 1562;

[4] J. R. Ellis, M. E. Gomez, G. K. Leontaris, S. Lola, D. V. Nanopoulos, Eur. Phys. J. C 14, 319 (2000);

[5] J. R. Ellis, J. Hisano, M. Raidal, Y. Shimizu, Phys. Rev. D 66, 115013 (2002);

[6] G. Cvetic, C. Dib, C. S. Kim, J. D. Kim, Phys. Rev. D 66, 034008 (2002);

[7] A. Masiero, S. K. Vempati, O. Vives, Nucl. Phys. B 649, 189 (2003);

[8] C. x. Yue, Y. m. Zhang, L. j. Liu, Phys. Lett. B 547, 252 (2002);

[9] "Higgs-Mediated $\tau \to \mu$ and $\tau \to e$ transitions in II Higgs doublet Model and Supersymmetry", P Paradisi.

[10] K. S. Babu and C. Kolda, Phys. Rev. Lett. 89, 241802 (2002)

[11] A. Dedes, J. R. Ellis and M. Raidal, Phys. Lett. B 549, 159 (2002)

[12] A. Brignole and A. Rossi, Phys. Lett. B 566, 217 (2003)

[13] Particle Data Group, 2005;

[14] D. Bliss *et al.* (CLEO Collaboration), Phys. Rev. D 57 (1998) 5903;

[15] B. Aubert *et al.* (Babar Collaboration), Phys. Rev. Lett 92 (2004) 121801;

[16] K. Abe *et al.* (Belle Collaboration), Phys. Rev. Lett. 92 (2004) 171802;

[17] G.J. Feldman and R.D. Cousins, Phys. Rev. D 57 (1998) 3873;

[18] "First study of the CMS sensitivity to the neutrinosless decay $\tau \to \mu\mu\mu$", CMS NOTE 2002/037;

[19] Atlas Collaboration, "Atlas Magnet System Technical Design Report", CERN-LHCC-97-18, ATLAS TDR 6 (1997);

[20] ATLAS Collaboration, "Atlas Inner Detector Technical Design Report", Vol. 1, CERN-LHC-97-16, ATLAS TDR 4 (1997);

[21] ATLAS Collaboration, "Atlas Inner Detector Technical Design Report", Vol. 2, CERN-LHC-97-17, ATLAS TDR 5 (1997);

[22] "Reconstruction of the Extended Gauge Structure from Z' Observables at Future Colliders", by F. del Aguila, M. Cvetic, and P. Langacker, Phys. Rev. D52, 37 (1995);

[23] ATLAS Collaboration, "Atlas Liquid Argon Calorimeter Technical Design Report", CERN-LHC-97-41, ATLAS TDR 2 (1998);

[24] ATLAS Collaboration, "Atlas Tile Calorimeter Technical Design Report", CERN-LHCC-97-42, ATLAS TDR 3 (1996);

[25] ATLAS Collaboration, "Atlas Muon Spectrometer Technical Design Report", CERN-LHCC-97-22, ATLAS TDR 10 (1997);

[26] "The alignment system of the ATLAS muon spectrometer", Amelung, C; Phys. J. C 33 (2004);

[27] ATLAS Collaboration, "Atlas First Level Trigger Technical Design Report", CERN-LHCC-98-14, (1998);

[28] ATLAS Collaboration, "Atlas High-level Triggers, DAQ and DCS Technical Proposal", CERN-LHCC-2000-17 (2000);

[29] "The Monitored Drift Tube (MDT) chambers for the muon precision tracking in the ATLAS spectrometer", By ATLAS Collaboration 1999. Published in Nucl.Phys.Proc.Suppl.78:422-425,1999;

[30] "Drift properties of Monitored Drift Tubes chambers of the ATLAS Muon Spectrometer", Cirilli, M; Nucl. Instrum. Methods Phys. Res., A 518 (2004) 62-64;

[31] "Performance studies of the monitored drift-tube chambers of the ATLAS muon spectrometer", Cerutti, F; Nucl. Instrum. Methods Phys. Res., A 535 (2004)

[32] "Calib: a package for MDT calibration studies - User Manual", Bagnaia, P; Baroncelli, A; Iodice, M; Orestano, D; Pontecorvo, L; ATL-MUON-2005-013; ATL-COM-MUON-2002-004; Geneva, CERN, 2002;

[33] "The 2004 ATLAS Combined Test Beam", ATL-ENEWS-2004-021;

[34] "System Test of the ATLAS Muon Spectrometer in the H8 Beam at the CERN SPS", ATL-MUON-2004-026; ATL-COM-MUON-2004-020; CERN-ATL-COM-MUON-2004-020, Geneva CERN, 2004.

[35] "The H8 muon community, Proposed measurement program for H8 2004 muon system test", ATL-COM-MUON 2004-006, 4 May 2004.

[36] G.R. Lynch, O.I. Dahl, "Approximations to multiple Coulomb scattering", Nucl. Inst. Meth. B58(1991) 6-10;

[37] "Assembly and Certification of ATLAS Muon Stations for the Middle and Outer Barrel at CERN" Aielli, G; Di Girolamo, A; Fleischmann, P; Iengo, P; Kovar, S; Wotschack, J; Zimmermann, S; ATL-COM-MUON-2006-021;

[38] "The GNAM monitoring system and the OHP histogram presenter for ATLAS" Zema, F. et al.; ATL-DAQ-CONF-2005-029; ATL-COM-DAQ-2005-031; CERN-ATL-COM-DAQ-2005-031;

[39] "The Persint visualization program for the ATLAS experiment" Pomarède, D; Virchaux, M; cs.GR/0305057; Geneva: CERN, 29 May 2003;

[40] "The ROD Crate DAQ of the ATLAS Data Acquisition System", Gameiro, S et al. ATL-DAQ-CONF-2005-020; ATL-COM-DAQ-2005-019: CERN, 2005;

[41] "Uncertainties on W and Z production at the LHC.", ATLAS-COM-PHYS-2005-045, Sep 2005. 13pp. e-Print Archive: hep-ex/0509002;

[42] "PYTHIA 6.2 Physics and Manual", arXiv:hep-ph/0108264, v1 (2001);

[43] M. Cacciari, M. Greco and P. Nason, JHEP **9805** (1998) 007
[arXiv:hep-ph/9803400];

[44] M. Cacciari, S. Frixione and P. Nason, JHEP **0103** (2001) 006
[arXiv:hep-ph/0102134];

[45] "ATLFAST 2.0: a fast simulation package for ATLAS", ATL-PHYS-98-131;

[46] "IPATREC: inner detector pattern-recognition and track-fitting" Clifft, R; Poppleton, A; ATL-SOFT-94-009; ATO-PN-9.- Geneva : CERN, 14 Jun 1994;

[47] "Track reconstruction in the ATLAS Muon Spectrometer with MOORE 007" Adams, D et al. ATL-SOFT-2003-007; Geneva : CERN, 28 May 2003;

[48] "Muon Identification using the MUID package" Fassouliotis, D. et al., ATL-CONF-2003-011;

[49] "Low Pt Muon Identification in the Atlas Detector at the LHC" S.Tarem, N.Panikashvili, ATL-SOFT-2004-003;

[50] ATLAS Collaboration, "Detector and physics performance Technical Design Report", Vol. 1, CERN-LHCC-99-14, ATLAS TDR 14 (1999);